Thermal stability, structure and interface study of x-ray multilayers for EUV and soft x-ray applications

By

NAGESWARARAO POTHANA

PHYS 03201204002

Raja Ramanna Centre for Advanced Technology, Indore

A thesis submitted to the

Board of Studies in Physical Sciences

In partial fulfillment of requirements

for the Degree of

DOCTOR OF PHILOSOPHY

of

HOMI BHABHA NATIONAL INSTITUTE

August, 2018

Homi Bhabha National Institute

Recommendations of the Viva Voce Committee

As members of the Viva Voce Committee, we certify that we have read the dissertation prepared by Nageswararao Pothana entitled " Thermal stability, structure and interface study of x-ray multilayers for EUV and soft x-ray applications" and recommend that it may be accepted as fulfilling the thesis requirement for the award of Degree of Doctor of Philosophy.

Chairman – Prof. Rama Chari	**Date:** 11.9.19.
Guide / Convener – Prof. Tapas Ganguli	**Date:** 11/09/2019
Technical advisor- Dr.S.K.Rai	**Date:** 11/9/2019
Examiner – Prof. Satish Vitta	**Date:** 11/09/2019.
External Member - Prof.D.Bhattacharya	**Date:** 11/09/19
Member - Prof. S.M.Gupta	**Date:** 11-9-19
Member - Prof.T.K.Sahrma	**Date:** 11.9.19
Member - Prof.M.H.Modi	**Date:** 11.9.19
Member- Prof.M.K.Chattopadhyay	**Date:** 11/09/2019

Final approval and acceptance of this thesis is contingent upon the candidate's submission of the final copies of the thesis to HBNI.

I/We hereby certify that I/we have read this thesis prepared under my/our direction and recommend that it may be accepted as fulfilling the thesis requirement.

Date: 11-09-2019

Place: RRCAT, Indore

Dr. Tapas Ganguli
Guide

STATEMENT BY AUTHOR

This dissertation has been submitted in partial fulfillment of requirements for an advanced degree at Homi Bhabha National Institute (HBNI) and is deposited in the Library to be made available to borrowers under rules of the HBNI.

Brief quotations from this dissertation are allowable without special permission, provided that accurate acknowledgement of source is made. Requests for permission for extended quotation from or reproduction of this manuscript in whole or in part may be granted by the Competent Authority of HBNI when in his or her judgment the proposed use of the material is in the interests of scholarship. In all other instances, however, permission must be obtained from the author.

Nageswararao Pothana

DECLARATION

I, hereby declare that the investigation presented in the thesis has been carried out by me. The work is original and has not been submitted earlier as a whole or in part for a degree / diploma at this or any other Institution / University.

Nageswararao Pothana

List of publications arising from the thesis

Journal:

1. Fabrication and evaluation of large area Mo/Si soft x-ray multilayer mirrors at Indus synchrotron facilities.

   P.N.Rao, M.Nayak, G.S.Lodha, S.K.Rai, A.K.Srivatava, M.H.Modi, A.Sagdeo, Advances in Optical Technologies (**2012)**, **2012**, 1-8.

2. Thermal stability of ion beam sputter deposited C/B_4C X-ray multilayer mirror. **P.N.Rao**, M.H.Modi, S.K.Rai, V.G.Sathe, S.K.Deb, G.S.Lodha,

   Thin solid films **(2013)**, **527**, 244-249.

3. Stability and Normal Incidence Reflectivity of W/B_4C Multilayer near the boron K-edge.

   P.N.Rao, S.K.Rai, M.Nayak, G.S.Lodha

   Appl. Opt. **(2013)**, **52**, 6126-6130.

4. Thermally induced interface changes in W/B_4C multilayers

   P. N. Rao, S. K.Rai, A. K.Sinha, M. N.Singh, G. S. Lodha

   Thin Solid Films **(2015)**, **589**, 268-271.

5. Microstructure and composition analysis of low-Z/low-Z multilayers by combining hard and resonant soft x-ray reflectivity

   P. N. Rao, S.K.Rai, A. Srivastava, T.Ganguli, R.Dhawan, P. A.Naik

   J. Appl. Phys. **(2016)**, **119**, 245301-6.

6. Investigation of thickness dependent composition of boron carbide thin films by resonant reflectivity

   P. N. Rao, R.K. Gupta, K. Saravana, A.Bose , S.C.Joshi S.K.Rai, T.Ganguli, Surface and Coatings Technology **(2018)**, **334**, 536-542.

Conferences:

1. Magnetron sputtering system for fabrication of x-ray multilayer optics

   M.Nayak, **P.N.Rao**, G.S.Lodha

   AIP. confer. proc. **(2012)**, **1451**, 154-156

2. Fabrication and evaluation of large area soft x-ray multilayer mirrors

   P.N.Rao, M.Nayak, G.S.Lodha, S.K.Rai, A.K.Srivatava, M.H.Modi, A.Sagdeo

   AIP. confer. proc. **(2012)**, **1451**, 151-153.

3. Growth of multilayer optics for synchrotron radiation source

   P.N.Rao, M.Nayak, M.H.Modi, S.K.Rai, G.S.Lodha

   Journal of Physics: Conference Series **(2013)**, **425**, 052023 (1-4).

DEDICATIONS

To My Parents

ACKNOWLEDGEMENTS

I would like to thank my Ph.D guide Dr. Tapas Ganguli for his constant encouragement and support throughout this work. He has faith in me which helps to explore scientific problems.

I am thankful to my earlier guide Dr. G. S. Lodha for assigning the work on x-ray multilayer optics. He is the person who started x-ray MLs activity at RRCAT and has great vision for the need of such kind of optics for synchrotron radiation applications.

I am extremely thankful to my technical advisor Dr. Sanjya kumar Rai for useful discussion and suggestions. Many of things are clear to me after discussing with him. I am rigid to try new things, but he always pushes me to think in different directions and make me put more efforts to complete the task. Without him it could be possible for me to give shape like this for my thesis.

I am extremely thankful to Dr. S. K. Deb for useful discussion. He is a great mentor and humble person. I learned a lot from him while analyzing the Raman spectroscopy data. He always motivated subordinates with his words.

I am grateful to Dr. S.K. Gupta, BARC, Dr. Dibyendu Bhattacharyya, BARC, Dr. L.M. Kukreja and all the members of Doctoral Committee for their constructive criticism, motivation and guidance. I am especially grateful to Dr. S.B. Roy for erudite guidance and motivational words.

I would like to thank Dr. Vasant G Sathe, UGC-DAE CSR Indore for help in performing the Raman Spectroscopy and analyzing the data.

I would like to thank Dr. Anil Sinha for help in performing the synchrotron based grazing incidence x-ray diffraction measurements. I am also thankful to him in analysis and presenting the diffraction data. I would like to thank Dr. Arvind Kumar Srivastava for help in performing the transmission electron microscopy. I would like to thank Dr. Mohammed Hussein Modi for help in publishing my first scientific article in a journal.

I would like to thank Dr. Sendhil Raja S. and Dr. Dileep Kumar Gupta, IUC-DAE CSR Indore for help in carrying out the stress measurements on ML samples. I am really thankful to them for their selfless effort. I would like to thank Dr. Sundaravel and Dr. K. Saravanan, IGCAR for performing RBS experiments and useful discussion. I would also like to thank Shri.Aniruddha Bose and Shri. S.C.Joshi for performing TOF-SIMS measurements.

I would like to thank Dr. Maheshwar Nayak for my association with him during initial days of my carrier. I am also thankful to him for providing the magnetron sputtering system for sample preparation. I would like to thank Dr. Pooja Gupta for useful discussion. I am also thankful to her for preparing the reply to many of my manuscripts and make my view clear to third person.

I would like to thank Dr. Archna Sagdeo for useful discussion on x-ray diffraction. I would like to thank Dr. Vishal Prabhakar Dhamgaye for providing the white synchrotron radiation beam at Lithography beamline (BL-07) at Indus-2.I would like to thank Mr. Raj Kumar Gupta for his help in soft x-ray reflectivity measurements. I am also thankful to each and every staff associated with reflectivity beamline at Indus-1.

I would like to thank Mr. Rajnish Dhawan for his help in preparing samples using ion beam sputtering. I would like to thank Mr. Mahendra Babu for his help in preparing samples for transmission electron microscopy.

In the end I would like to thank all of my family members. My Ph.D would have not been possible without them. I always remember sacrifices made my parents. I especially thank to my wife Bhavani for her patience, our kids Manashvi and Purvi whose smile and innocence give me strength to face any kind of situation in life.

Contents

Summary

The main interest of this thesis is to investigate suitability of B_4C based MLs in SXR-EUV wavelength regime. We studied the reflective of W/B_4C MLs near the B K-edge. We observed a maximum peak reflectance of 8.3% at wavelength of 68 Å. The reflectivity drops to 7.3% after 800 °C annealing. W/B_4C MLs undergone period thickness changes on annealing. The period variation is less when B_4C layer thickness is more than 2 nm and MLs with B_4C layer thicknesses are less than 2 nm undergone more period thickness and drop in reflectivity. One of the drawbacks of W/B_4C MLs is absorption is high in W which limits the maximum number of layer pairs contributing to the reflectivity and hence energy resolution. To improve the energy resolution we replace W with C. The electron density difference (~6%) is small between C and B_4C as a result there is an uncertainty in estimating the structural information using GIXR. Combination of GIXR and TEM techniques gives improved structural information. Resonant reflectivity measurements performed in the vicinity of the B K-edge suggested that presence of excess C into the boron carbide layer. C/B_4C ML structure is stable up to 700 °C. We investigated the compositional changes in boron carbide thin films using RSXR. We observed the boron deficient growth/carbon rich growth with decrease in film thickness. Such compositional changes might be responsible for observed period thickness in W/B_4C MLs as a function of B_4C layer thickness. Additionally, we have established that RSXR is a useful tool in estimating the composition of films in a non-destructive way.

List of Figures:

List of Tables:

Chapter 1.

Introduction

This chapter gives brief introduction to extreme ultraviolet and soft x-ray region. The theory of refractive index and multilayer optics are discussed. The various aspects related to multilayer optics are discussed.

1.1. Introduction:

The spectral region, extending from wavelength λ= 5 Å to 400 Å is generally categorized as soft x-ray (SXR) 5 Å < λ < 50 Å, and extreme ultraviolet (EUV) radiation 50 Å< λ < 400 Å. The boundary between these two regions is not stringent. EUV-SXR is an important region in electromagnetic spectrum. There are a large number of atomic resonances fall in this region which provide mechanism for both elemental and chemical identifications.[1] This provides opportunities for researchers in both science and technology. The progress in this region is delayed due to the large absorption typically in nanometer or micrometer range. The wavelengths are relatively shorter which open up possibilities to study the nanometer scale structures in microscopy[2], and to write smaller patterns in lithography.[3,4] Diffraction limited focal spot can be achieved in this region which allowed to perform spatially resolved spectroscopes, to spatial resolutions measured in tens of nanometers.[5,6] The region covering the oxygen absorption edge λ=23 Å to carbon absorption edge λ=44 Å is known as water window region, which falls in SXR region. SXR radiation is absorbed by carbon and transparent to oxygen and this natural contrast is indeed very attractive for imaging the biological samples in its natural aqueous environment.[7-9] These interesting properties attract many researchers in the field of imaging, spectroscopy and nanofabrication.

Conventional optical elements like lens and thin film coated mirrors are not applicable in this region. This is due to small refractive index in this spectral region for all materials compared to vacuum. As a result all materials give a negligible reflection or refraction in this region. Electromagnetic radiation undergoes reflection and refraction at a boundary between two media if there is a change in refractive index. The knowledge of refractive index is essential to predict the response of a medium to incident radiation. The complex refractive index in X-ray region can be written as[10],

$$n = 1 - \delta + i\beta, \qquad \mathbf{1.1}$$

$$\delta = \frac{n_a r_e \lambda^2}{2\pi} \left[f_{NR}^{o} + f'(\lambda)\right] \qquad \mathbf{1.2}$$

$$\beta = \frac{n_a r_e \lambda^2}{2\pi} f''(\lambda) \qquad \mathbf{1.3}$$

where δ (dispersion coefficient) and β (absorption coefficient) are the optical constants, n_a is the atomic density, r_e is the classical electron radius, f_{NR}^{o} is the non-resonant atomic scattering factor (ASF), $f'(\lambda)$and $f''(\lambda)$ are the dispersion and absorption corrections to the ASF that arise from the fact that electron are bound in an atom. The real part of ASF tells effective number of electrons that can be contributed to scattering and imaginary part tells the absorption in a medium. The optical constants decrease quadratically with decreasing wavelengths. In EUV-SXR region both the values of δ and β are comparable and are in the range of 10^{-2} to 10^{-3}. The real part of refractive index,1-δ is close to one in this region, therefore weak refraction occurs at boundary between two media. The absorption is high in this region. The weak refraction and high absorption make it impossible to use lenses in this region. To avoid absorption one can use a thin film coated mirrors at low grazing angles. These thin film coated mirrors works on the principle of total external reflection. These mirrors reflect almost all the incidence radiation below the critical angle. The drawbacks of this kind of optics are large size is required and also there is weak reflection at angle larger than critical angle. In case of natural crystals reflection from each atomic plane is added up in phase and gives intensity maximum at Bragg's condition. But the spacing between planes in natural crystal is of the order of sub nm. So one cannot use crystals as an optical element in this region where wavelengths are of the order of nm. If such structure made artificially with layer thicknesses of the order of nm, they would be used as artificial Bragg reflectors. Such artificial Bragg reflectors can overcome the limitation imposed by grazing incidence optics which works at low incidence angles and non-availability of atomic spacing of natural crystals in this region.[11]

1.2. Theory of x-ray multilayers (MLs):

The theoretical reflectivity, R for a radiation incident normally on smooth interface between two media having difference in refractive index is given by

$$R = \left|\frac{n_1 - n_2}{n_1 + n_2}\right|^2 \approx \frac{\Delta\delta^2 + \Delta\beta^2}{4} \qquad \mathbf{1.4}$$

This shows that the reflectivity depends on the difference in refractive index. As discussed earlier both the optical constants δ and β are small in EUV and SXR region. This indicates that the normal incidence reflectivity from a single surface is very small in this region, typically not more than 1%.

The goal of ML fabrication is to enhance the low reflectivity available from a single boundary by adding up reflectivity from many boundaries. ML mirror consists of alternating layers A and B of thickness d_A and d_B respectively as shown in Figure 1.1. The structure is periodic in a direction perpendicular to the surface with period thickness, $d=d_A+d_B$. A radiation of wavelength λ incident at a grazing angle θ, on such a structure will be reflected from each interface. At Bragg's angle, θ_m given by the relation[1]

$$2dsin\theta_m\sqrt{1-\frac{2\overline{\delta}}{sin^2\theta_m}} = m\lambda \qquad \mathbf{1.5}$$

Reflected wave from each interface will be added in phase and gives a maximum in reflectivity pattern. The square root term in the above equation appears due to refractive correction. Where m is the order of Bragg reflection and $\overline{\delta}$ is the bilayer weighted real part of the refractive index. In case of bi-layer it is given by the relation

$$\overline{\delta} = \frac{d_A \delta_A + d_B \delta_B}{d_A + d_B} \qquad \mathbf{1.6}$$

Where δ_A and δ_B are the dispersion coefficients of layers A and B respectively.

Figure 1.1: Schematic diagram showing a ML structure consist of N layer pairs and period thickness of d.

The parameters that can be used to distinguish different ML structures are period thickness, d, number of layer pairs, N and layers thickness ratio, Γ which is defined as the ratio between the thicknesses of high electron density layer to ML period. Depending up on operating wavelength and incidence angle, the parameters that can be varied in ML structures are layers thickness ratio, number of bilayers, period thickness and material pairs.ML period thickness is chosen according to Bragg's condition. Material combination is selected in such a way that the maximum reflection occurs at an interface between them. It means that the refractive index difference should be high to yield maximum reflectivity. Absorption limits the penetration depth and hence the maximum number of layer pairs that can contribute to the reflectivity. So absorption should be less in the selected combination. A large difference in electron density of a high and low atomic number, Z between the layer materials provides refractive index contrast and less absorption in low Z elements can be useful as a guide for material selection. Some of the low Z elements whose absorption edges fall in EUV-SXR region are: Ti (L edge 31.4 Å), V (L edge 24.3 Å), Sc (L edge 31.9 Å), C (K edge 43.7 Å), B (K edge 6.6 Å), B_4C (K edge 65.6 Å), Be (K edge 111 Å), Si (L edge 123 Å), Mg (L edge 251 Å) and Al (L edge 171 Å). Most commonly used high atomic number elements in this region are Cr, Ni, Mo, Ru, Rh, Pd, La and W.[12-18]

The main advantages of ML structures stem from the tunability of period thickness, lateral and in-depth gradient of periodicity; these can be tailored according to the desired incidence geometry and wavelength regime. Furthermore, ML structures have the advantage of being used for focusing and imaging applications by depositing structures on figured surface. EUV-SXR radiation has many applications in the field of imaging, spectroscopy and nanofabrication which makes the development of coatings for EUV-SXR region is an active and intensive research field. The ML optics is used as a normal incidence reflector to perform microscopy in water window region. Also multilayer mirrors find application in many fields of science and technology, e.g., in lithography, synchrotron beamlines, telescopes, spectroscopy, plasma diagnostics, and soft x-ray laser research.[19-23]

1.3. Roughness of ML optics:

Designing of ML structures for different wavelengths are done based on material optical properties. The properties of ML structures (like Bragg peak width, peak and integrated reflectivity) are strongly influenced by the physical and chemical nature of interface, the composition of the individual layers. In reality interface between two materials is not sharp but has finite width caused by roughness, or intermixing of materials near the boundary. Rough boundary causes wide angle scattering which results into a drop in specular reflectivity. Intermixing or compound formation due to chemical reaction between materials at an interface reduces optical contrast which results in a drop in reflectivity. The finite interface width was taken into account according to Nevot-Croce model[24] and reduction in reflected intensity is given by

$$\mathrm{R(q)=R_o e^{(-q_1 q_2 \sigma^2)}} \qquad \mathbf{1.7}$$

where R_o is the reflected intensity from the ideal interface, σ is the interface width, q_1 and q_2 are momentum transfer vector values in the two media forming the interface. Depending up on application wavelength this interface width limits the maximum achievable reflectivity from a particular combination. As an example Figure 1.2, show the reflectivity, R(σ) values at different, σ values divided by reflectivity, R_0 of ideal ML structures as a function of σ. From the Figure1.2, it is clear that the ML structures with smaller, d have steeper fall in reflectivity ratios as compared ML structures with higher, d values. The reflectivity of ML consists of d= 22 Å and σ= 3 Å falls to more than 50% of R_0. Interface width either due to roughness or due to compound formation represents the most serve limitation for the performance of MLs for small period thickness.

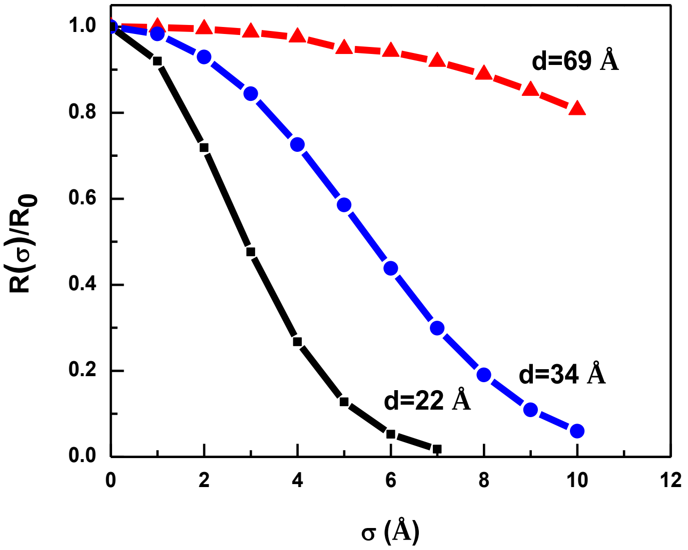

Figure 1.2: The calculated reflectivity ratio of ML structures as a function of interface width.

To achieve maximum reflectivity from a ML structure, σ shall be lea than 0.1d. For example to use MLs as normal incidence reflector at 66 Å (B K-edge), d≅33Å and hence total interface widths should be less than 3 Å. ML structures should have atomically smooth interfaces to use as a high reflecting mirror at shorter wavelengths. We have to select a material combination that can form smooth interfaces for application at shorter wavelengths.

1.4. Thermal load on ML optics:

ML mirrors when exposed to high intense synchrotron radiation absorb a part of the radiation. As a result, at high incident intensity the mirror heats up and shows quick raise in temperature.[25] Thermal load on optics causes changes in the multilayer's internal structure due to void elimination, changes in stress, crystallization, interdiffusion of atoms at the interfaces and compound interlayer growth.[26-29] Any changes in internal structure of MLs due to thermal loading causes change in ML period thickness and cause drop in maximum achievable reflectivity at application wavelength. The change in ML period thickness causes change in optimally reflected wavelength (or incidence angle). Recent study on Mo/Si MLs exposed to an intense pulsed EUV source showed that the silicide formation causes irreversible structural changes.[30]The observed damage mechanism is similar to degradation observed during annealing treatments. So study of structural changes up on thermal annealing and its detrimental effect on the reflectance at an application wavelength of an optical element is important, as it is exposed to high power synchrotron radiations.

MLs with reflectivity close to the theoretically achievable values were developed for wavelength regime greater than Si L-edge (124 Å).The measured reflectivity for shorter wavelength regime is much less than the theoretically achievable values. This is due to the fact that the effect of interface imperfections like roughness or interdiffusion is stronger at shorter wavelength. MLs near the B K-edge (65.6 Å) are of interest for x-ray analysis of boron content in doped semiconductors, plasma diagnostics and lithography. Few ML combinations like Ru/B_4C[15], La/B_4C[17], Mo/B_4C[31] and Pd/B_4C[16] were studied for application near the B K-edge. Ru/B_4C combination is stable only up to 250°C. Annealing studies carried out on Mo/B_4C ML suggest that significant drop in reflectivity at temperature > 600°C. In Chapter 4, we investigated the structural changes with thermal annealing and its detrimental effect on the reflectance of W/B_4C ML structure near the B K-edge. We have chosen W/B_4C ML combination because B_4C can form smooth interfaces with W and tendency of interface reaction is less in W/B_4C as compared to Ru/B_4C and Mo/B_4C.[32] Jankowski et al.[33] observed an expansion in W/B_4C multilayer sample with period thickness of 40 Å after annealing and the observed changes were attempted to be explained by auger electron spectroscopy and transmission electron microscopy but no clear understanding was evolved. A more detailed analysis is required to understand the period thickness changes in W/B_4C ML structures upon thermal annealing. W/B_4C MLs were thermally stable up to the temperature of 700 °C and a little drop in peak reflectance (~1%) was observed after 800 °C annealing near the B K-edge. We observed both period expansion and compression in W/B_4C ML structures on annealing. The period thicknesses of ML structures were accurately measured using hard x-ray reflectivity (XRR). To understand the period thickness changes due to interlayer compound formation a synchrotron based grazing incidence x-ray diffraction measurements were performed.

1.5. Composition of ML optics:

Two factors: Structure parameters (like thickness, interface roughness/width) and composition of layers influence the properties (like Bragg peak width, peak and integrated reflectivity) of ML structures.[11,34] It is important to derive structural and compositional information of these nanometer scale ML structures so that the preparation techniques can be optimized to yield better performance. The finite absorption in the layers of ML structure limits the spectral band pass of width $\Delta E/E \sim 1/N$, where N is the number of layer pairs achieved from it. High resolution ML mirrors are realized either by reducing the thickness of high-Z absorber layer or by using the low-Z/low-Z combination[35]. The calculated reflectivity of Mo/Si which is a high-Z/low-Z combination and Si/B_4C which is a low-Z/low-Z combination is shown in Figure 1.3. The narrow Bragg peak in case of low-Z/low-Z ML is due to less absorption of incident radiation. XRR which works on the principle of electron density difference between layers is routinely used technique to derive structural information of ML structures. For a low-Z/low-Z combination, the electron density contrast (EDC) between layers is low and hence XRR provides the limited structural information. Thus combining the scattering technique like XRR with a microscopic technique like transmission electron microscopy (TEM) provides improved structural information. Further, XRR measurements are also less sensitive to compositional changes in thin film/ML structures consisting of low EDC elements. For example, boron carbide film is composed of B and C atoms and XRR measurements were insensitive to any change in B/C ratios. This is due to fact that electric field of incident radiation interacts with electron density of atoms within the samples and the incident radiation could not distinguish between the atoms having similar electron density. However near the absorption edges optical constants undergo strong variation and significantly modify the reflectivity pattern in this region. Using the soft x-ray reflectivity spectra measured near the absorption edges, we can infer the composition of low EDC structures.

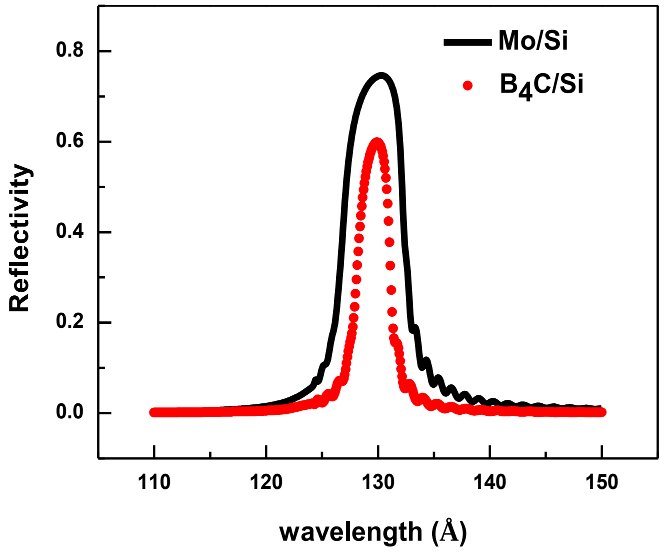

Figure 1.3: The calculated reflectivity of Mo/Si (d=69Å, Γ=0.4, σ=0Å, and N=100) and Si/B_4C (d=69Å, Γ=0.4, σ=0Å, and N=100) ML structures.

So combination of characterization techniques like XRR, TEM and resonant soft x-ray reflectivity can provide complete information about structural and compositional of low EDC structures. In Chapter 5, these aspects are shown with an example of 10-period C/B_4C multilayer which is a low-Z/low-Z combination. In general this method can apply to any low-Z/low-Z combination to derive structural and compositional information.

Boron carbide is an important x-ray optical element in both hard x-ray and EUV-SXR regions.[10,36] It is also a promising material for the next generation lithography application around the wavelength of λ=68 Å.[37,38] It is also found to be one of the suitable candidates for free electron laser applications.[39,41] It is used as capping and barrier layer to protect the ML structure from oxidation and as barrier layer to prevent the interdiffusion.[42] The compositional changes in the boron carbide causes significant changes in its optical constants in the vicinity of B K-edge and limits maximum achievable throughput from boron carbide based MLs. Figure 1.4 showing the calculated SXR profile of ideal W/B_4C ML structure with different B/C ratio. The reflectivity of ML structure decreases with decreasing the B/C ratio.

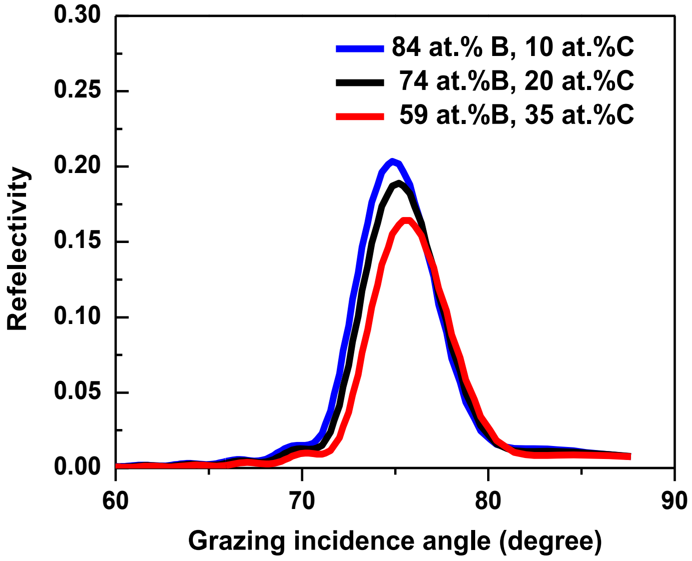

Figure 1.4: The calculated SXR profile of W/B_4C ML structure consisting of d=34Å, Γ=0.29, σ=0 Å, and N=50 with different B/C ratio.

In many applications boron carbide thin films with thickness ranging from a fraction of a nanometer to several nanometers have been used. It is important to study any thickness dependent compositional changes in boron carbide thin films.

In Chapter 6, we investigated thickness dependent compositional changes in boron carbide thin films. XRR were used to derive layer thickness and surface/interface roughness. SXR measurements near the B K-edge were measured to derive optical constants of deposited films. X-ray photo electron spectroscopy technique is used to study surface composition of thin films. Resonant Rutherford backscattering spectrometry and time of flight secondary ion mass spectrometry are used to complement the observation made from SXR.

In chapter 3, we have addressed the development of high reflectivity and large area ML optics in the EUV-SXR regime. Mo/Si ML was designed for normal incidence, a peak reflectivity of ~63% was achieved near the Si L-edge (100 eV). Mo/Si ML structure was deposited over the area of 300x100 mm^2 with period thickness variation less than 1% to use as a reflecting mirror near Si L-edge (124 Å). For the W/B_4C ML designed for normal incidence, a peak reflectivity of ~1.8% was achieved in the water window region.

Chapter 2

Experimental Techniques

In this chapter details of experimental techniques used in the thesis is presented. This includes both deposition and characterization techniques. The geometry of deposition systems are discussed in detail. Theory and experimental setup of characterization techniques are discussed in detail.

2.1. Sample preparation techniques:

Thin film deposition is classified into two categories: physical vapor deposition and chemical vapor deposition.[43-45]The role of deposition technique is to deposit material with desired properties in a reproducible manner and with minimum variation in their composition. In a Chemical vapor deposition the substrate is exposed to volatile precursors and produces a chemical change on a surface and produces a chemically deposited coating on it. Physical vapor deposition is classified into two types: (1) thermal evaporation and (2) sputtering. In this thesis we have used sputtering techniques like ion beam sputtering and magnetron sputtering to deposit thin films and multilayers (MLs). These techniques and geometry of deposition setup are discussed briefly in the following sections.

2.1.1. Sputtering:

In sputtering, the surface is bombarded with high energy ions and surface atoms of the solid are scattered backward due to collisions between the surface atoms and the energetic particles as shown in Figure 2.1. This phenomenon is known as sputtering. A measure of removal rate of surface atoms due to ion bombardment is the sputter yield, defined as the ratio between the number of sputter ejected atoms and the number of incident projectiles.[46] It depends upon the several factors like energy of incident ion, target material, incidence angle of ions and structure of the target surface. The sputtered atoms travel through vacuum and condense on the substrate. Cathode sputtering is used for the deposition of thin films. Sputtering can be realized using the different methods like dc diode, rf diode, magnetron, and ion-beam sputtering.

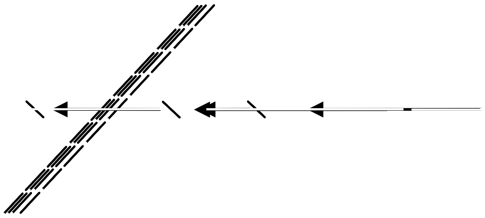

Figure 2.1: Schematic diagram showing the physical sputtering processes.

2.1.2. Magnetron Sputtering (MS):

In the basic sputtering process, a target (or cathode) plate is bombarded by energetic ions generated in glow discharge plasma, situated in front of the target. The bombardment process causes the removal of target atoms and also ejection of secondary electrons from the target surface. These secondary electrons play an important role in maintaining the plasma at lower pressure and enhance the sputtering rate. The basic sputtering process is limited by low deposition rate, low ionization efficiency in the plasma and high substrate heating. These limitations have been overcome by the development of magnetron sputtering.

In magnetron sputtering, a magnetic field parallel to the target surface is applied which can constraint the secondary electrons motion to the vicinity of the target surface. The electrons in the glow discharge show cylindrical motion and the center of the orbit drifts in the direction of **E** × **B** with drift velocity of E/B, where **E** and **B** denote the electric and magnetic fields respectively. Trapping the electrons in this way increases the probability of an ionising electron-atom collision occurring. As a result dense plasma forms near the target surface which will increase the sputtering rate of the target and deposition rate at the substrate. In addition, the magnetron sputtering system can be operated at lower pressure and voltages as compared to sputtering.

2.1.2a. Magnetron sputtering system configuration:

MS system[47] consists of two parts- main processing chamber and load lock chamber. Main chamber is rectangular shape with length ~800 mm,width~325 mm and height ~770 mm. The deposition system has ports to accommodate different magnetron sources, quartz crystal thickness monitors, substrate motions, residual gas analyzer, vacuum gauges, viewing ports etc. The schematic diagram of the deposition system is shown in Figure 2.2.

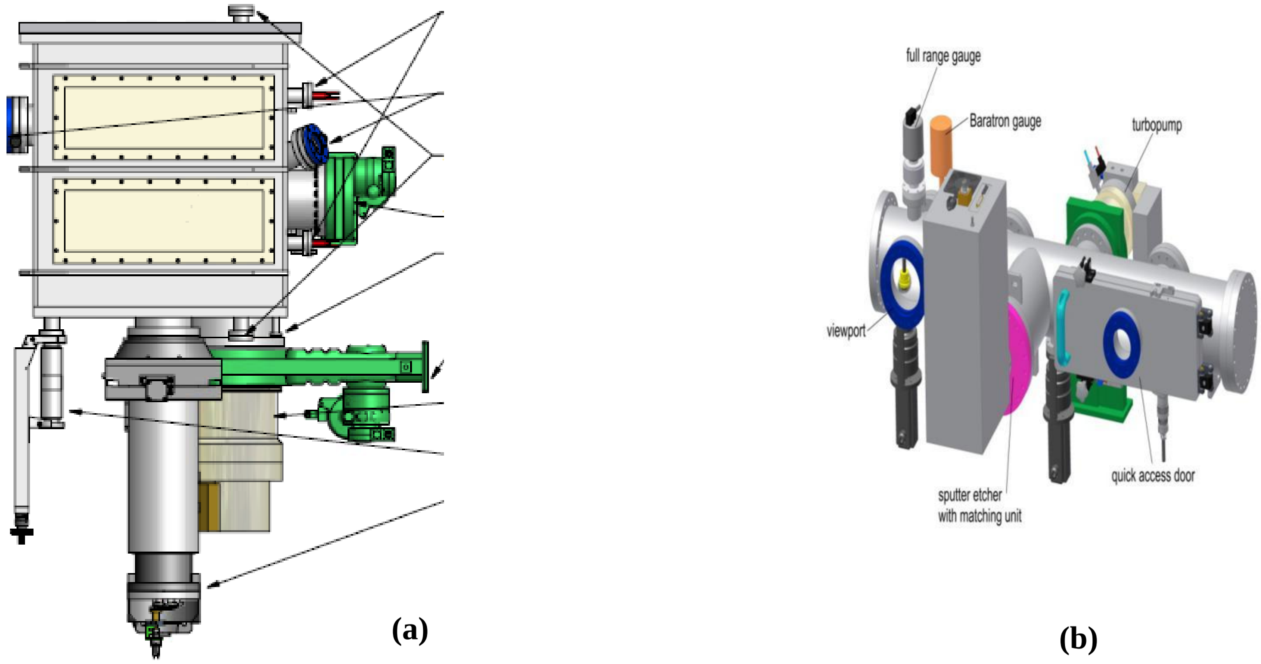

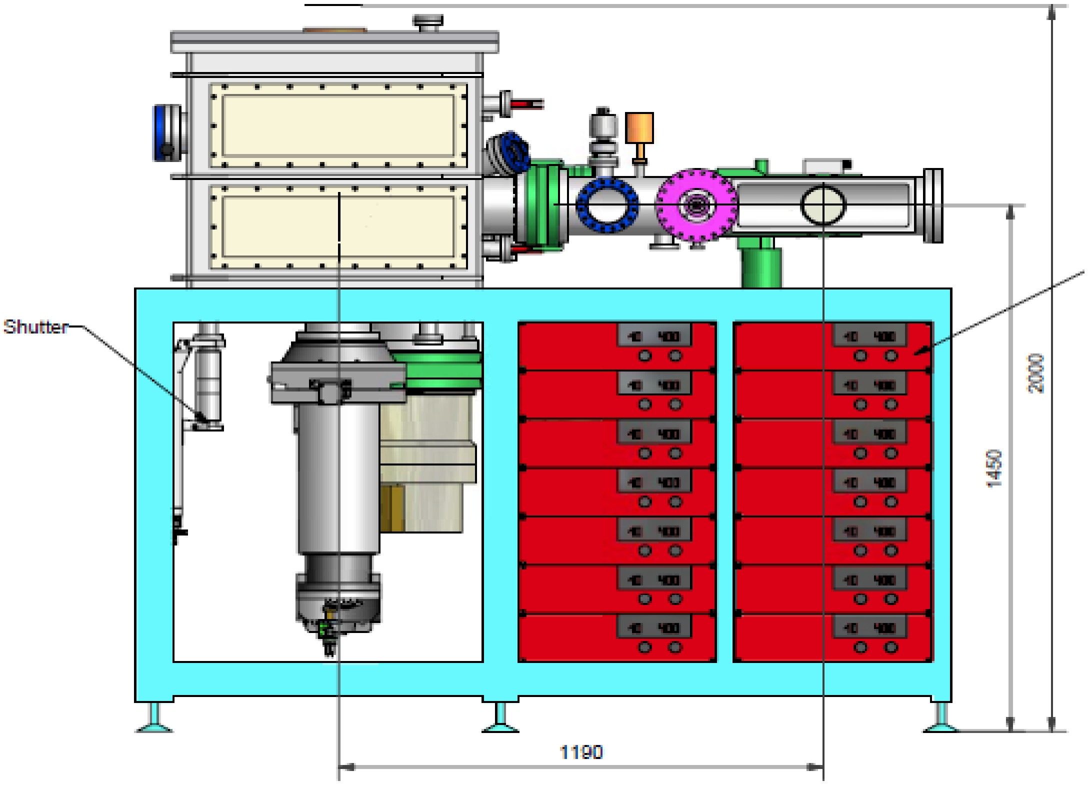

(c)

Figure 2.2: Schematic diagram showing the MS system. (a) Main chamber, (b) load lock chamber and (c) complete system.

A load lock system is attached to the main processing chamber for loading/unloading the substrate without disturbing the vacuum of the main processing chamber. The load lock system is a cylindrical chamber having length ~920 mm and diameter ~130 mm. A pneumatic UHV gate valve is used to isolate of the load lock chamber from the main chamber. The load lock system has port for pumping, pressure measurement and viewing of substrate. The sample is transferred from load lock chamber to the main chamber through a mechanical rail platform. In load lock chamber there is a facility for substrate cleaning using a RF ion etch gun. The RF ion etch gun has the maximum power of 1.6 kW.

The system configuration is such that the sputtering process takes place in horizontal direction. This minimizes the contamination of flaking on the substrate and the cathode. There are two horizontally facing magnetron cathodes, each having the size of 500 mm length and 100 mm width, mounted on one side of the main processing chamber. One cathode is powered by DC power supply with maximum power of 2 kW, the other has both DC and RF source with maximum power of 1 kW and 600 W, respectively. The cathodes are mounted to main chamber through rectangular flanges, and contain all required water, gas and electric high voltage feedthroughs. The sputtering gas pressure is regulated through mass flow controllers. The sputtering gas is ejected to the main chamber through an unbalanced flow rate from two sides of target to ensure uniform gas pressure over the sputter target. For avoiding cross talk between two source materials, there is shutter mounting assembly in front of sputter targets. There is a facility to mount different types of masking arrangements for controlling the spatial variation of deposition rate.

The vacuum system of the main chamber consists of 1800 l/s turbo molecular pump (TMP) backed by a scroll pump. The TMP is connected to the opposite side of the cathode in the main chamber through a pneumatic gate valve with variable port opening option. The ultimate pressure of the system after conditioning is ~ 1×10^{-8} mbar. In load lock chamber, pumping is done by a 250 l/s TMP to achieve a base pressure of 8×10^{-8} mbar. The pressure in the main and load lock chambers are monitored by Pirani and Penning gauge. The deposition system is fully auto controlled, starting from loading to unloading the substrate, with proper interlocking arrangements.

2.1.3. Ion beam sputtering (IBS):

In sputtering ions are used to sputter the target atoms. There are two classes of system used to generate ions: plasmas and ion beams. The only real difference here is that in plasma source, the surface to be bombarded is immersed in the plasma, and in the case of ion beam, the plasma is physically separated from the target, and an ion beam is extracted from the ion source to bombard the surface. This causes IBS operates at lower operating pressures (typically, 10^{-5} to 10^{-4} mbar, compared to 10^{-2} mbar) in the basic sputtering mode. This will reduces the inclusion of gas molecules in the sputtered films. To generate ions, we have used Kaufman-type broad ion source[48]. This type of source typically has a plasma chamber within the ion source with a hot filament cathode. Ions created in the source can be accelerated by means of multi-aperture grids to form a large area and intense beam.

2.1.3a. IBS system configuration:

The schematic diagram of IBS system is shown in Figure 2.3. The deposition consists of a single chamber. The deposition system has ports to accommodate quartz crystal thickness monitors, residual gas analyzer, vacuum gauges, viewing ports etc. We have used a 3 cm diameter Kaufman-type 1.5 kV hot-cathode gridded ion source, at an angle of 45° with respect to the chamber wall. To deposit multi elements, the deposition system is equipped with a multi-target holder in which four targets of different materials on a rotary motion feed-through can be mounted at the same time. A heating stage is attached to substrate holder for carrying a deposition at higher temperatures. The substrate temperature can be increased up to 500 °C. The vacuum system of the main chamber consists of 500 l/s turbo molecular pump (TMP) backed by a scroll pump. The ultimate pressure of the system after conditioning is ~ 1×10^{-7} mbar. The pressure in the system is monitored by Pirani and Penning gauge. The flow of sputtering gas, argon is controlled by mass flow controller. During the deposition the argon gas flow was fixed at 3 standard cubic centimeters (sccm), which results in a vacuum drop to 5×10^{-4} mbar in the chamber. An argon ion-beam of current ~ 25 mA and voltage 1000 V was used to sputter the target material.

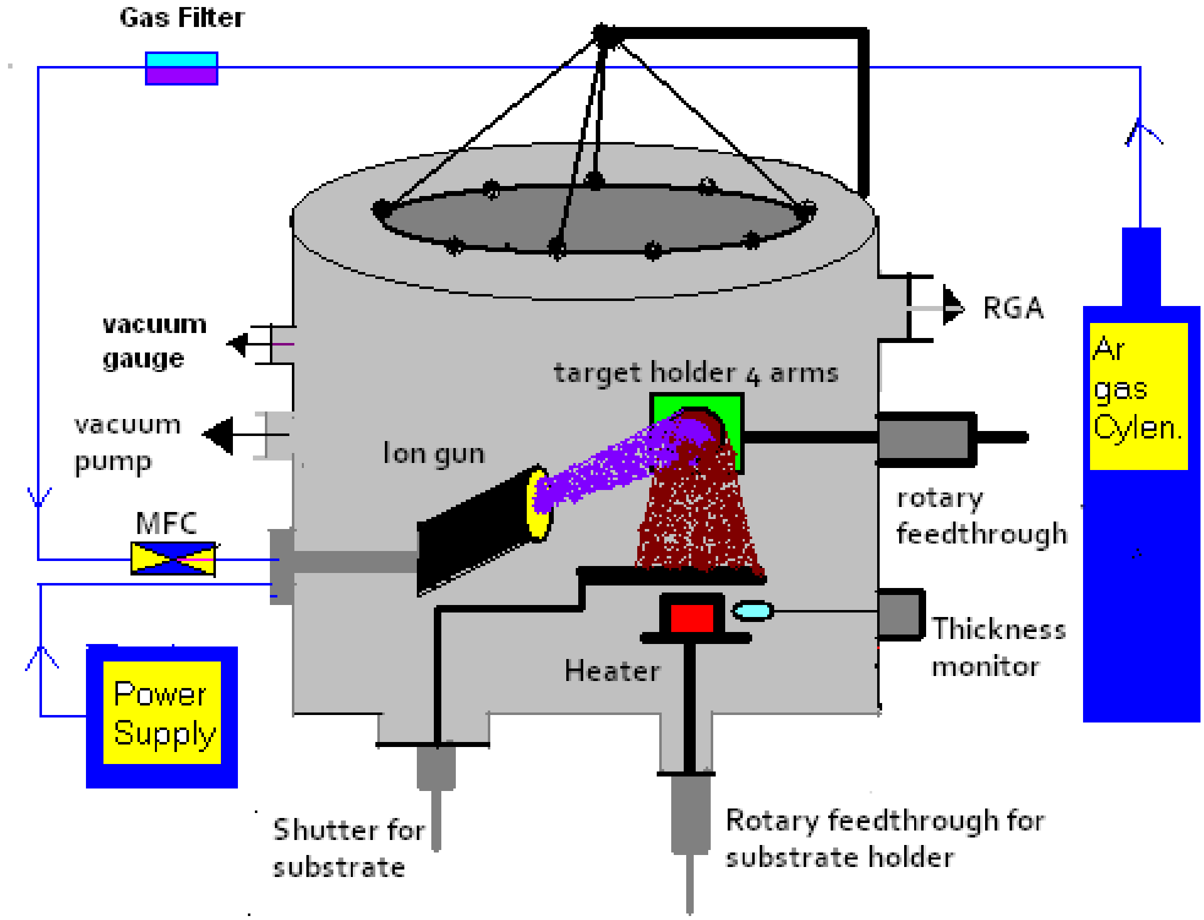

Figure 2.3: Schematic diagram showing the IBS system.

2.2. Characterization techniques:

2.2.1. Hard x-ray reflectivity (XRR):

XRR is a routinely used non-destructive tool to determine the layer thicknesses, period thickness of ML structures, the surface and interface roughness and average electron density of a layered system.[49-53] Electromagnetic radiation incident on an interface will undergo reflection and refraction provided the refractive indices of the media on two sides of interface are different. The refractive index in X-ray region can be written as

$$n = 1 - \delta + i\beta \qquad \mathbf{2.1}$$

Where δ (dispersion coefficient), and β (absorption coefficient) are known as optical constants.

2.2.1a. Single surface:

We have used wave theory to explain the phenomena of reflection and refraction. Figure 2.4. shows the schematic diagram of incident, reflected and refracted waves.

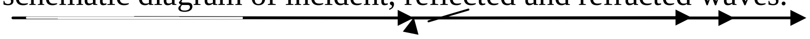

Figure 2.4: Schematic diagram showing incident, reflected, and refracted waves.

Let us consider an electromagnetic plane given by its electric field $\mathbf{E} = \mathbf{E_0}\, e^{-\mathbf{i}(wt - \mathbf{k_i}.\mathbf{r})}$ is incident from vacuum side. $\mathbf{k_i}$ and w are propagation wave vector and frequency of incident wave respectively. A part of the incident wave is reflected and a part of it transmitted into the medium having refractive index n. The reflected and refracted waves can be written as $\mathbf{E}' = \mathbf{E}'_{\mathbf{o}} e^{-\mathbf{i}(wt - \mathbf{k_f} \cdot \mathbf{r})}$ and $\mathbf{E}'' = \mathbf{E}''_{\mathbf{o}} e^{-\mathbf{i}(wt - \mathbf{k_t} \cdot \mathbf{r})}$ **,** respectively. At an interface separating two media, the ratio of refractive indices will determine the angle at which wave refracted, α_t in comparison to grazing incidence angle, α_i. Using Figure 2.4, Snell's law is

$$cos\alpha_i = n \, cos\alpha_t \qquad \textbf{2.2}$$

In general n is a complex number which implies that $cos\alpha_t$ is also complex number for real incidence angle α_i. For absorption free medium (β=0), if n>1, then $\alpha_t > \alpha_i$ and there exists a real angle of refraction for all incidence angles. However if n<1, then $\alpha_t < \alpha_i$ and there is a real angle of refraction for all angle incidence provide α_i is greater than the critical angle α_c. The angle of refraction α_t, is 0 at

$$cos\alpha_c = cos\alpha_i = n \qquad \textbf{2.3}$$

$$\alpha_c = (2\delta)^{1/2} \qquad \textbf{2.4}$$

At values α_i is less than α_c total reflection occurs and only evanescent wave penetrate into the material. At values α_i is greater than α_c the reflection reduces significantly as most of the radiation penetrates into the material. The extent at which radiation reflected at a surface or an interface depends upon the differences in wave vector or momentum transfer vector. In specular reflectivity one can monitor reflectivity as a function of momentum transfer vector perpendicular to the surface, q_z. Hence

$$q_z = |\boldsymbol{k_i} - \boldsymbol{k_f}| = \frac{4\pi sin\alpha_i}{\lambda} \qquad \textbf{2.5}$$

Where **k$_i$** and **k$_f$** are incident and reflected wave vectors respectively, α_i is the grazing incidence angle and λ is the wavelength of probing radiation. The reflection coefficient for a smooth surface or an interface is given by Fresnel formula.[1] The Fresnel's reflection and transmission coefficients for s and p polarization are defined as

$$r_s = \frac{k_{i,z} - k_{t,z}}{k_{i,z} + k_{t,z}} = \frac{sin\alpha_i - n\ sin\alpha_t}{sin\alpha_i + n\ sin\alpha_t} \qquad \textbf{2.6}$$

$$t_s = \frac{2\ k_{i,z}}{k_{i,z} + k_{t,z}} = \frac{2 sin\alpha_i}{sin\alpha_i + n\ sin\alpha_t} \qquad \textbf{2.7}$$

$$r_p = \frac{n^2 k_{i,z} - k_{t,z}}{n^2 k_{i,z} + k_{t,z}} = \frac{n^2\ sin\alpha_i - sin\alpha_t}{n^2\ sin\alpha_i + sin\alpha_t} \qquad \textbf{2.8}$$

$$t_p = \frac{2\ k_{i,z}}{n^2 k_{i,z} + k_{t,z}} = \frac{2 sin\alpha_i}{n^2 sin\alpha_i + sin\alpha_t} \qquad \textbf{2.9}$$

Where $k_{i,z} = k\ sin\alpha_i$ and $k_{t,z} = nk\ sin\alpha_t$ are normal component of incident and transmitted wave vector.

The reflectivity is the modulus square of reflection coefficient and is defined as

$$R_s = |r_s|^2 = \left|\frac{sin\alpha_i - n\ sin\alpha_t}{sin\alpha_i + n\ sin\alpha_t}\right|^2 \qquad \textbf{2.10}$$

$$R_p = \left|r_p\right|^2 = \left|\frac{n^2\ sin\alpha_i - sin\alpha_t}{n^2\ sin\alpha_i + n\ sin\alpha_t}\right|^2 \qquad \textbf{2.11}$$

2.2.1b. Multiple interfaces:

For many practical applications a specimen contains multiple interfaces are of interest than that of single surface. Let us consider a specimen having n layers on a substrate each layer having different thickness as shown in Figure 2.5. There is total n+1 interface, n+1 corresponds to specimen/substrate and 1 corresponds to specimen/vacuum interface. The reflectance is calculated by considering first the reflectance between the substrate and the layer closest to the substrate, i.e., the (n +1)th and nth layer, respectively. This is given by Fresnel's reflection coefficient from a surface. The reflectance between the (n - 1)th and nth layer is then given by

Figure 2.5: Schematic of specimen contains n layers of different thickness on top of substrate.

$$r_{n-1,n} = \frac{r'_{n-1,n} + r'_{n,n+1} exp(2id_n k_n)}{1 + r'_{n-1,n} r'_{n,n+1} exp(2id_n k_n)} \qquad \textbf{2.12}$$

Where the prime denotes the reflectance at the interfaces given by Fresnel's reflection coefficient from a surface while $r_{n-1,n}$ includes internal reflections at the n-1, n and n, n + 1 interfaces of the single layer film. This reflectance, $r_{n-1,n}$ is then used to calculate the reflectance for the next layer by

$$r_{n-2,n-1} = \frac{r'_{n-2,n-1} + r_{n-1,n} exp(2id_{n-1}k_{n-1})}{1 + r'_{n-2,n-1} r_{n-1,n} exp(2id_{n-1}k_{n-1})} \qquad \textbf{2.13}$$

This recursion[52,54] is then continued until the reflectance at the air/specimen interface is obtained which yields the reflectance of the specimen.

So far we have considered smooth surface and interfaces. But in reality these surfaces and interfaces are not smooth. The roughness causes gradual change in refractive index between two media which results in drop in reflectivity. The loss in reflectivity due to roughness is taken into account using Névot-Croce model.[24]They assumed surface heights have a Gaussian distribution and divided rough surface into ensemble of smooth interfaces with root mean square deviation of σ. With these assumptions they got the result that roughness damps the specular reflectivity at an interface j, by a factor $exp(-2k_{z,j}k_{z,j+1}\sigma^2)$. Hence by analysis of reflectivity curves we can get information about layer thicknesses, surface and interface roughness and mean electron density.

In the present work XRR measurements were performed at Cu-kα radiation (E=8.05 keV) on Bruker Discover D8 diffractometer with Ge(220) two bounce monochromator. XRR measurements were performed using 100 μm slits in incident beam and 200 μm slits in reflected beam. A nonlinear least square curve fitting technique based on χ^2 minimization method was applied for the determination of structural parameters from the XRR measurements.

2.2.2. Soft x-ray reflectivity (SXR):

Conventional XRR works on the principle of difference in electron density contrast (EDC). In case of specimen contains low-Z elements difference EDC is less which limits the observable contrast. One cannot get the depth distribution of specimen contains low-Z elements using XRR. In the vicinity of the absorption edge both the optical constants δ and β undergo strong variation. For many light elements absorption edge falls in the EUV-SXR regime. Any small changes in the composition of film gives rise to a significant change in optical index and that can give a clear contrast in a reflectivity profile. Thus analysis of the reflectivity curves measured near the absorption edges gives the concentration profile of all the chemical elements present in the sample. The angular dependence inherent to reflectivity measurements brings furthermore the spatial selectivity. If a sample contains several chemical elements the optical indices can be represented as [55,56]

$$\delta = 2.7007\times10^{-4}\lambda^2\rho\frac{\sum_j X_j\left(f^0_{NR,j} + f'_{R,j}(\lambda)\right)}{\sum_j X_j\mu_j} \qquad \mathbf{2.14}$$

$$\beta = 2.7007\times10^{-4}\lambda^2\rho\frac{\sum_j X_j f''_{R,j}(\lambda)}{\sum_j X_j\mu_j} \qquad \mathbf{2.15}$$

Here λ is the incident wavelength [nm], ρ is the density [g/cc], X_j is the atomic fraction of j atoms, and μ_j is the atomic weight of j atoms [g/mol]. $f^o_{NR}(q)$ is the non-resonant ASF, $f'_R(\lambda)$ and $f''_R(\lambda)$ are the dispersion and absorption corrections to the ASF arising from anomalous dispersion. In the present thesis we reconstruct the composition profile of boron carbide B_4C by performing the SXR measurements in the vicinity of B K-edge using Indus-1 reflectivity beamline[57].

The Indus-1 reflectivity beamline having a toroidal grating monochromator delivers photons in the range of 40-1000 Å with high flux ($\sim10^{11}$ photons/sec) and moderate spectral resolution ($\lambda/\Delta\lambda$: 200-500). Various absorption edge filters are provided in the beamline to suppress the higher order contamination from the monochromator. The reflectometer station installed on the beamline operates in high vacuum environment ($\sim 5 \times 10^{-7}$ mbar). To maintain UHV environment of 1×10^{-9} mbar of the beamline, a differential pumping system has been incorporated between the experimental station and the beamline. The experimental chamber consist two rotary stages driven by stepper motors and a linear translation stage for sample mounting. The two rotary stages were used to accomplish the standard $\theta - 2\theta$ scan for normal reflectivity measurements. The linear stage is employed to bring the sample in and out of the direct beam path, in order to facilitate the direct beam monitoring. An absolute soft x-ray silicon photo diode detector (International Radiation Detector Inc. USA) is used in direct current mode for monitoring reflected and incident beam intensities. The current output of the detector is measured using an electrometer amplifier.

2.2.3. Transmission electron microscopy (TEM):

TEM is a microscopy technique[58-60] which acquires the real space information directly unlike scattering technique (e.g. XRR), where we need modeling to get the real space information. TEM provides the information about layer thicknesses, composition, crystallinity and interfaces, etc. Microscope is an instrument for magnifying things too small to see with the naked eye. TEM were developed because of the limited image resolution in light microscopes. According to Rayleigh criteria, the smallest distance that can be resolved, δ is given approximately by

$$\delta = \frac{0.61\lambda}{n\, sin\beta} \qquad \textbf{2.16}$$

Where λ is the wavelength of incident radiation, n is the refractive index of the viewing medium, and β is the semi angle of collection of the magnifying lens. From the above equation it is clear that resolution in light microscopy is limited by wavelength of radiation. In the case of electrons, their wavelengths are dependent on their energy or their accelerating voltage. If we ignore relativistic correction, the wavelength of electron in terms of energy is written as a

$$\lambda \sim \frac{1.22}{E^{1/2}}\ nm \qquad \textbf{2.17}$$

Where E is the energy of the electron in eV. We can increase the energy of electron by applying higher acceleration voltage. So using the TEM with higher accelerating electrons we can achieve sub nanometer resolution. TEM experimental setup is shown schematically in Figure 2.6.

Figure 2.6: Schematic diagram of TEM consists of different components.

The electron microscope consists of three main parts-(1) a system consisting of a hot cathode emitting electrons and condenser lens to illuminate the sample with electron beam, (2) imaging system comprising of the objective and projector lenses, and (3) photographic film or fluorescent screen to convert the intensity of electron beam into image.

The transmission electron microscope investigations were carried out on a Philips CM 200 TEM, operated at 200 kV accelerating voltage. A cross-sectional sample for TEM was prepared by conventional method of mechanical thinning and ion polishing. Mechanical thinning was performed by dimple grinder up to a thickness of ~ 50 μm. Ion milling of the sample was carried out at very low angle (~3^{o}) and low energy (3 keV) to avoid sample damage. The damage introduced in the sample can be estimated by the thickness of amorphous layer formed at the edge of the sample. The amorphous layer thickness was ~ 10 Å. The final thickness of the electron thin region was ~ 1000 Å.

2.2.4. Grazing incidence X-ray diffraction (GIXRD):

GIXRD measurements were performed on W/B_4C ML structures to study the annealing products. The penetration depth of x-ray is in the range of $10 - 100$ μm. In case of thin film investigations thickness is small causing the most of diffraction signal coming from the substrate in $\theta - 2\theta$ geometry. In GIXRD[61], the incidence angle is small which causes the path traveled by the x-rays to increase within the sample and most of the diffraction signal came from the sample only. The measurement geometry of GIXRD is shown schematically in Figure 2.7. $\mathbf{K_i}$ and $\mathbf{K_f}$ are the incident and diffracted wave vectors respectively. $\mathbf{Q} = \mathbf{K_f} - \mathbf{K_i}$, is a momentum transfer vector and surface normal is along z-axis. Detector moves at angle $2\theta - \alpha$ with respect to the surface, where 2θ is the scattering angle denotes the angle between the outgoing beam and the elongation of the incoming beam. During the measurements incidence angle α is kept fixed around 1°.

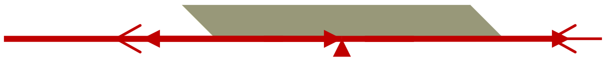

Figure 2.7: Shows the geometry of GIXRD experiment.

In the GIXRD mode, **Q** is neither parallel to surface normal nor does its orientation remain constant. Rather the orientation of **Q** changes in the course of the measurement, during which the scattering vector is tilted from the start position close to surface normal towards an end position ever closer to the incoming beam $\mathbf{K_i}$. As a result in GIXRD, we observe Bragg peaks that are caused by lattice planes neither parallel with the substrate surface nor with each other. In the present work GIXRD measurements were performed using lab source Cu-k_α radiation (E=8.05 keV) on Bruker Discover D8 diffractometer and also using synchrotron radiation. Synchrotron based GIXRD measurements were performed on the angle dispersive x-ray diffraction beamline[62], (BL-12) at Indus-2 synchrotron source. Photon beam energy of 13 keV was used and data is collected on image plate area detector (Mar-345 dtb). The radiation energy and distance between the sample and detector were calibrated using the diffraction pattern of LaB_6 NIST standard

2.2.5. Raman spectroscopy:

Raman spectroscopy provides information about molecular vibrations that can be used for sample identification and quantitation.[63]The sample under study is illuminated with monochromatic light source (i.e. laser) and detecting the scattered light. The scattered light consists of two types: Rayleigh scattering is strong and has the same frequency as the incident beam (V_o), and Raman scattering is very weak (~ 10^{-5} of the incident beam) and has frequencies $V_o \pm V_m$, where V_m is a vibrational frequency of a molecule. The V_o-V_m and V_o+V_m lines are called the Stokes and anti-Stokes lines, respectively. Thus, in Raman spectroscopy, we measure the vibrational frequency (V_m) as a shift from the incident beam frequency (V_o). Raman spectra are plotted with respect to the laser frequency such that the Rayleigh band lies at 0 cm^{-1}. On this scale, the band positions will lie at frequencies that correspond to the energy levels of different functional group vibrations. Raman spectra are more sensitive to the structural change of carbon films which are usually in amorphous states. Using Raman spectroscopy, we can compare the structure of the carbon in multilayers before and after annealing and can relate the structural changes to the period expansion. The Raman scattering measurements were performed using a Jobin Yvon micro-Raman spectrometer (HR800). The schematic diagram Raman spectrometer setup is show in Figure 2.8.

Figure 2.8: Schematic diagram of Raman spectrometer.

Jobin Yvon micro-Raman spectrometer (HR800) consists of following four major components:

(1) Excitation source, which is generally a continuous-wave (CW) laser

(2) Sample illumination and collection system

(3) Wavelength selector

(4) Detection and computer control/processing systems

The sample is illuminated with the Ar laser at 4880 Å. The scattered light is collected with a lens and is sent through interference filter and was analyzed using a spectrometer. In the present study, Raman spectra were recorded over the range of 250-2000 cm^{-1}.

2.2.6. X-ray photo electron spectroscopy (XPS):

XPS is a technique used to study different chemical states, relative composition and for identification of elements present on the surface.[64,65]When a specimen is bombarded with monochromatic X-ray photons, these photons are absorbed by the atoms leading to ionization and emission of electrons. The kinetic energy of emitted electrons is measured using suitable electron analyser and photoelectron spectrum can be recorded. The kinetic energy of emitted electrons can be written as

$$K.E. = hv - E_b \qquad \textbf{2.18}$$

Where hv is the energy of incident photon and E_b is the binding energy of the electron in the atomic orbital from which it has emitted. The basic principle of X-ray photoelectron process is shown schematically in Figure 2.9.

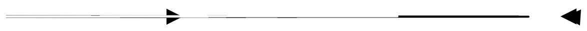

Figure 2.9: Schematic diagram explaining the basic principle of XPS

The binding energies (BE) of energy levels in solids are conventionally measured with respect to the Fermi-level of the solid, rather than the vacuum level. This involves a small correction to the equation 2.18 given above in order to account for the work function (φ) of the solid.

$$\mathrm{K.E.} = h\upsilon - E_b - \varphi \qquad \mathbf{2.19}$$

XPS experimental setup is shown schematically in Figure 2.10. It consists of three main components -1) x-ray source, 2) hemispherical electron energy analyzer and 3) electron detector. x-ray tube is used to generate the x-rays. X-ray of fixed energy impinges on the sample surface and the electron excited by the photoelectric effect are then analysed with respect to their kinetic energy and their momentum in an electron analyzer. XPS measurements were performed in ultra high vacuum environment. Ultra high vacuum environment is maintained to increase the mean free path of photoelectron emitted from the surface and reaching the detector. It will also reduce the contamination on the surface of the sample under study.

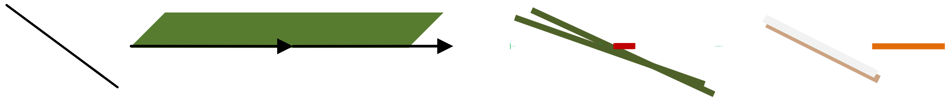

Figure 2.10: Schematic diagram showing XPS experimental setup.

In an atom, electron bound to the nucleus and has characteristic binding energy associated with each atomic orbital. Each atom will give rise to a characteristic set of peaks in the photoelectron spectrum at kinetic energies determined by the photon energy and the respective binding energies. The presence of peaks at particular energies therefore indicates the presence of a specific element in the sample under study and area under the peak is related to the concentration of the element within the sampled region. Thus, the technique provides a quantitative analysis of the surface composition. The most commonly employed X-ray sources are those giving rise to: Mg Kα radiation: hν = 1253.6 eV Al kα radiation: hν = 1486.6 eV. In the present study we have used Al Kα radiation to study the different chemical states of B and C in boron carbide thin films.

2.2.7. Rutherford backscattering spectrometry (RBS):

Rutherford backscattering spectrometry (RBS) is a technique based on the detection of high energy ions scattered by target nuclei. It is the most widely used technique for elemental identification and composition analysis. The advantages of this technique are: quantitative information without any standards, fast and non-destructive in nature. In this technique, a low mass and highly energetic (typically 0.5-4 MeV) ions are directed on a solid sample (losing energy through inelastic collisions with electrons of solid sample), scatters on atomic nuclei (losing energy through kinematics), and travels back (losing energy through inelastic collision with electrons) to be detected and energy analyzed by a surface barrier detector.[66-68] The schematic of RBS setup is shown in Figure 2.11

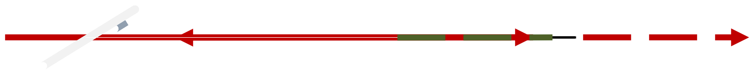

Figure 2.11: Schematic of RBS experimental setup.

2.2.7a. Elemental identification

In RBS, the identification of various target atoms is done based on the analysis of energy of backscattered ions. Let us consider an ion of mass, m_1 having energy E_o is incident on a target atom of mass m_2 initially at rest. The elastic collision between incident ion and target atom can be described by considering conservation of energy and momentum. If θ is the scattering angle as shown in Figure 2.11, the ratio of the projectile energy before (E_o) and after (E_1) the collision is expressed by the kinematic factor K, given by

$$K = \frac{E_o}{E_1} = \left[\frac{\left(m_2^2 - m_1^2 \sin^2\theta\right)^{1/2} + m_1 \cos\theta}{m_2 + m_1}\right]^2 \qquad \textbf{2.20}$$

Since incident ion energy E_o is known and θ is fixed by the geometry of experimental set-up, the scattered ion energy can be converted into target atom mass spectra.

2.2.7b. Depth analysis:

The difference in the energy of backscattered ions from an atom at the sample surface and from an atom of same mass below the sample surface contains the depth information. The backscattered ions from an atom at the sample surface will appear in the energy spectrum at a position $E_1 = K \bullet E_0$. Let us assume that backscattering occurs at a depth Δx in the solid as shown in Figure 2.12. The energy of incident ions at this point is

$$E_{in}(\Delta \mathrm{x}) = E_o - \Delta E_{in} = E_o - \left(\frac{dE}{d\mathrm{x}}\right)_{E_0} \Delta \mathrm{x} \qquad \textbf{2.21}$$

Figure 2.12: Schematic diagram showing energy loss of backscattered ions from an atom at surface and similar atom at a depth Δx.

The energy of backscattered ions due to elastic collision between incident ions and target atom at this depth is $K.E_{in}(\Delta \mathrm{x})$. Let ΔE_{out} is the amount of energy lost while traversing back to the detector. The energy of backscattered ions coming from a depth Δx, detected by detector is

$$E_{det} = K.E_{in}(\Delta \mathrm{x}) - E_{out} = K\left(E_o - \left(\frac{dE}{d\mathrm{x}}\right)_{E_0} \Delta \mathrm{x}\right) - \frac{\Delta \mathrm{x}}{\cos\theta}\left(\frac{dE}{d\mathrm{x}}\right)_{E_{in}} \qquad \textbf{2.22}$$

The difference in the energy of ions backscattered from an atom on the surface and backscattered from a similar atom at a depth Δx is

$$\Delta E = K.E_o - E_{det} = \left(K\left(\frac{dE}{dx}\right)_{E_0} + \frac{1}{\cos\theta}\left(\frac{dE}{dx}\right)_{E_{in}}\right) \Delta \mathrm{x} \qquad \textbf{2.23}$$

There is a direct relation between energy loss and depth. Therefore by measuring the energy loss of backscattered ions we can infer depth information.

2.2.7c. compositional information:

The RBS scattering yield (i.e. , number of detected backscattered ions from any element) is

$$Y = Q\Omega\sigma(\theta)Nt \qquad \textbf{2.24}$$

Where Q is the number of incident ions, Ω is the solid angle subtended at detector, σ(θ) is the RBS cross-section, N is the atomic density (g/cc) and t is the thickness of the sample. By known RBS cross-section and measured yield from RBS experiment we can get compositional information from the above equation without any standard sample. The RBS cross-section can be written as

$$\sigma(E,\theta) = \left(\frac{Z_1Z_2e^2}{4E}\right)^2 \frac{4\left[\left(m_2^2-m_1^2\sin^2\theta\right)^{1/2}+m_2\cos\theta\right]^2}{m_2\sin^4\theta\left(m_2^2-m_1^2\sin^2\theta\right)^{1/2}} \qquad \textbf{2.25}$$

When $m_2 >> m_1$ the above equation can be simplified as

$$= \left(\frac{Z_1Z_2e^2}{4E}\right)^2 \frac{1}{\sin^4\theta/2} \qquad \textbf{2.26}$$

The RBS cross-section changes quadratically with the atomic number of target atom. The RBS is generally suitable for detection of heavy elements on lighter substrate. It is not suitable for detection of light elements in heavy substrates due to 1). Scattering yield is low for lighter elements and 2). Overlap of RBS signal with continuous back ground from the substrate. However, in many cases, if the energy of the incident ion is high, and can able to cross the coulomb barrier between incident ion and target nuclei and strong nuclear forces appears which results into a resonant scattering from the low-Z elements with enhanced cross-section. This non-RBS or resonant-RBS technique is used to detect lighter elements on the heavier substrate.

2.2.8. Time of flight secondary ion mass spectrometry (TOF-SIMS):

Secondary ion mass spectrometry is an analytical technique used to obtain compositional and structural information of elements present on the sample surface. The principle behind this technique is to analyze the mass of secondary atomic/molecular ions produced from sample surface due to bombardment of primary ions having keV energy. A collision cascade model is used to explain the observed features in sputtering. [69] The schematic representation of collision cascade is shown in Figure 2.13.

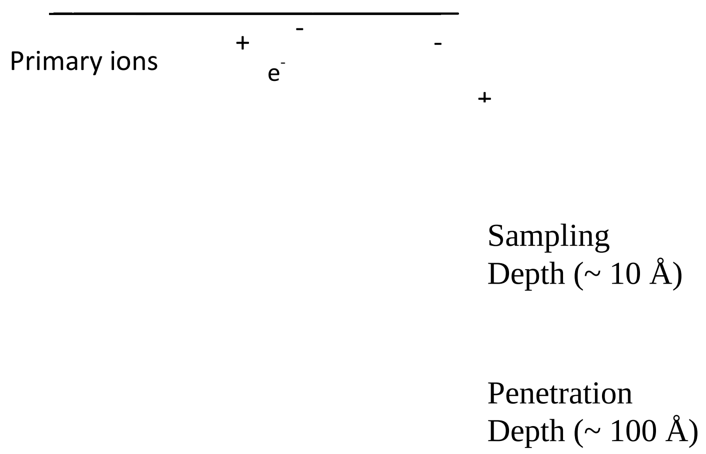

Figure 2.13: Schematic diagram showing a collision cascade.

There are two different variants of this technique 1). Static SIMS and 2). Dynamic SIMS, depending upon the erosion of the surface due to bombardment with primary ions.

1. Static SIMS: This mode of operation is used to get information about composition of the uppermost monolayer without disturbing its structure. To achieve this we need a primary

ion beam with ~0.1-10 keV energies and current density ~0.1-1 nA/cm^2. The lifetime of a monolayer is quite long (minutes/a few hours).

2. Dynamic SIMS: This mode of operation is used to get depth profiling of chemical elements constitute of the sample. To get in-depth information we require primary ions with energies 10-30 keV and current densities up to some A/cm^2. The lifetime of a monolayer is down to 10^{-3} sec under these conditions.[70] In this mode of operation sputtering and analysis were done simultaneously. Due to high sensitivity (down to the ppb range) of dynamic SIMS the presence of very thin interfaces can be studied. A depth profile is constructed using an ion beam to remove sequential layers of material from the surface while acquiring mass spectra at each depth. A typical analysis depth is less than 20 Å and is therefore better suited for the compositional analysis of ultra-thin layers and nanoscale sample features.

2.2.8a. Quantification in SIMS:

The mass-selected ion current in SIMS can be related to atomic concentration through a several parameters[71]

$$I_S^E = I_P C_E S \beta T \qquad \textbf{2.27}$$

Where I_S^E is the secondary ion current of spices E, I_P is the primary ion beam current, C_E is the concentration of species E, S is the sputtered ion yield of E, β is ionization efficiency i.e. probability of the detected species forming positive or negative ions, and T is the transmission of analysis system. The above equation shows that from the measured secondary ion mass current. One can extract the concentration information which implies that quantification can be made easily. However, S and β were found to vary moderately and strongly, respectively with the sample composition (matrix effect). Ionization efficiencies vary over several orders of magnitude for different elements, and likewise vary with the chemistry of the sputtered surface, thus ion signals often vary nonlinearly with concentration**.** This is a major issue to the quantification using SIMS.

In this study, we have used dynamic TOF-SIMS to study the in-depth concentration of different thickness boron carbide thin films. The schematic diagram of SIMS used in this thesis is shown in Figure2.13. TOF-SIMS depth profile analysis of boron carbide thin films was carried out in interlaced mode with pulsed Bi_1+ at 30 keV (~5pA) as the analysis gun and 1keV Cs+ as the sputter gun operating at a constant current of ~75nA. The area of analysis across all measurements was 100µm x 100µm inside the sputter area of 300µm x 300µm. The secondary ions produced are mass analysed using time of flight principle.

2.2.8b. Working of TOF mass spectrometer

Figure 2.14: Schematic showing the principle of Time of Flight mass spectrometer.

Secondary ions produced from the sample due to bombardment of primary ions are accelerated to the same voltage (~2-3 keV) over a very short distance as shown in Figure 2.14. As a result all secondary ions acquire same kinetic energy before they enter a free flight path of length L.

If initial energy (few eV) of secondary ions emitted from sample is neglected, the kinetic energy of these secondary ions can be expressed as

$$E_{K.E} = qV = \frac{1}{2} m_x v_x^2 \qquad \mathbf{2.28}$$

Where q is the charge state of secondary ion, V is the accelerating voltage, m_i and v_i are the mass and velocity of species *x* respectively. Let us assume *t* is the time taken by the species to reach the detector after travelling path length L. It can be written as

$$t = \frac{L}{v_x} = L\left(\frac{m_x}{2qV}\right)^{1/2} \qquad \textbf{2.29}$$

The parameters that are known are L, V and measured time t. The unknown quantities are mass and charge state of ions. These are estimated according to

$$\frac{m_x}{q} = \frac{2Vt^2}{L^2} \qquad \textbf{2.30}$$

From the above equation we can identify the secondary ions having different mass and charge state. This technique relies on the time of flight so it is essential that the ions to be analysed enter the flight path simultaneously or at least within the shortest possible time interval. To achieve this, the area of the surface to be analysed is bombarded with pulses of primary ions whose duration is as short as possible. With a TOF mass analyzer m/Δm, above 10,000 can be achieved.

2.2.8c. Secondary ion Detector:

The detection system is a combination of a channel plate for ion to electron conversion, a scintillator for electron to photon conversion and a photomultiplier, combined with a very fast electronic pulse counting system. The electrons, emitted from the backside of the channelplate, are accelerated onto the scintillator. The scintillator is coated with a conducting Al film, which is penetrated by the keV electrons. The photons emitted out of the backside of the scintillator are detected by the photomultiplier.

Chapter 3.

Fabrication and evaluation of large area Mo/Si multilayers for EUV-SXR application

In this chapter, we present the Fabrication and evaluation of large area Mo/Si multilayers for EUV-SXR application. We discuss optimization of deposition parameters to achieve uniform thickness large area (300 X 100 mm^2*) MLs. We obtained less than 1% variation in the period thickness in the whole area. To understand influence of process parameters on the quality of grown multilayers different characterization techniques were used. Results obtained are discussed in this chapter.*

3.1. Introduction:

X-ray multilayer (ML) mirror is a one dimensional artificial Bragg reflector.[10] It bridges between naturally occurring crystal optics and total reflection optics. The former gives excellent energy resolution however integrated reflectivity is small because of narrow rocking curve. The later gives high reflectivity at extremely small glancing incidence geometry and acts as energy cutoff reflector.[10] X-ray ML mirror provides high integrated reflectivity with moderate spectral bandpass. ML mirror have reasonable high acceptance angle compared to total reflection optics in hard x-ray region, and also gives normal incidence optics in soft x-ray/extreme ultra violet spectral range. The main advantages of ML mirrors stem from the tunability of period thickness, composition, lateral and in-depth gradient of periodicity; these can be tailored according to the desired incidence geometry and wavelength regime. Furthermore, ML mirrors have advantages of being used for focusing and imaging application by depositing structures on figured surface. However, fabrication of these ML mirrors is a challenging task. It requires deposition system capable of fabricating uniform, ultrathin smooth layer (~8 to 50 Å) with thickness control on atomic scale and number of layer pairs ranging from ~ 50 to 500. This task becomes more stringent in case of shorter wavelengths and large area ML for device applications.

Large area MLs have different potential applications such as soft x-ray/extreme ultra violet (EUV) lithography[19,72-74], soft x-ray imaging using Schwarzschild objective[75], double ML monochromator[76-78], super mirror for hard x-ray synchrotron, astrophysics[79], x-ray telescope[80,81], and for generating parallel/focusing x-ray beam using Göbel mirrors.[82,83] For optical system using more than one ML mirror, the layer-to-layer thickness, uniformity and run-to-run reproducibility during fabrication of these ML mirrors should be precisely controlled. To achieve high reflectivity, run-to-run stability and uniformity over large area require: (i) a stable and reproducible fabrication system (ii) precise geometrical configuration of the fabrication system along with proper masking arrangements for improvement in uniformity (iii) optimization of process parameters, such as rate of deposition, kinetic energy of add-atoms etc. to obtain optimum thin film growth condition. Various techniques have been attempted by different groups to produce large area ML mirrors on flat as well as figured substrates.

Using magnetron sputtering, Kortright et al.[75] obtained thickness uniformity better than 99% on 75-mm diameter flat substrate through substrate spinning and masking. Takenaka et al.[72] achieved uniformity of 99.2% on 6-inch diameter flat substrate with 63% reflectivity at 130 Å for Mo/Si MLs fabricated by RF magnetron sputtering through substrate spinning and masking. Mackay et al.[77] and Tsuruta et al.[84] fabricated MLs on flat silicon substrate using magnetron sputtering for monochromator application. The former have obtained uniformity >99% on 75×25-mm^2 area, in W/C ML, using substrate rotation and masking, whereas the later have obtained uniformity 99% on 152×38-mm^2 area in Mo/C ML using substrate rotation. As the dimension of optics increases further, additional constraints are imposed in deposition system to generate stable and uniform distribution of plasma for thickness control. Few reports are available to fabricate MLs with increased dimension. Dietsch et al.[85] fabricated Ni/C MLs on 6-inch diameter substrate (both flat and curved) by pulse laser deposition method. By using substrate motion and masking, they have obtained uniformity 99% with layer to layer thickness error ≤0.1 Å and run-to-run stability <0.5 Å. Gawlitza et al.[83] have fabricated Mo/Si MLs on 200-mm diameter flat substrate using ion beam deposition with ion assist gun. Using mask and substrate rotation they obtained uniformity 99.9% upto radius of 80 –mm, after that uniformity decreases to 99.7%. Recently Morawe et al.[78] fabricated W/B_4C ML on float glass substrate and achieved uniformity ~99.5% over an area of 1200×200 mm^2 using substrate motion and masking arrangements.

In this chapter we report, fabrication and evaluation of high reflectivity Mo/Si MLs on 300×100 mm^2 area substrate with good control over layer-to-layer thickness, lateral thickness homogeneity and run-to-run reproducibility using magnetron sputtering. We have achieved high quality interface structure by optimizing process parameters.

3.2. Experimental:

Mo/Si MLs are fabricated using magnetron sputtering system which has both DC and RF compatibility.[47]There are two rectangular cathodes of size 500 mm × 100 mm each. The sputtering process is in a horizontal configuration. Sample movement is fully software controlled from load lock to main processing chamber. The base pressure in main chamber and load lock system is 1×10^{-8} mbar and 8×10^{-8} mbar, respectively. Load lock chamber contains a RF ion etcher for substrate cleaning. Figure 3.1. Shows the magnetron sputtering used for deposition of various samples. All test samples are fabricated on Si and float glass substrates. Substrate moves linearly over sputter sources with variable speed. The deposited material thickness is determined by the time of substrate exposure to the source, which, in turn depend on the velocity of the substrate. Purity of Mo and Si target is 99.9 and 99.99, respectively. High purity (99.999%) argon is used as sputtering gas. DC power is used for sputtering of Mo and RF power is used for Si. During optimization of the sputtering parameters, sputtering power for Mo and Si is varied from 100 to 200 W and 200 to 400 W, respectively. Ar flow is varied from 4 to 12 sccm, resulting in pressure variation of the process chamber between $1.0\ x10^{-3}$ to $8\ x10^{-3}$ mbar. The target-substrate distance is varied from 50 mm to 150 mm. A reproducibility of target-substrate position of less than 0.5 mm is realized. During fabrication of MLs, ML periodicity (d) is varied from 40 to 100Å, thickness ratio (ratio of Mo thickness to period thickness) Γ is varied from 0.3 to 0.45 and number of layer pairs (N) is varied from 5 to 65.

Figure 3.1: Showing the magnetron sputtering system used for deposition of various samples.

The performance of Mo/Si ML is tested using Indus-1 reflectivity beamline.[57] Hard x-ray reflectivity (XRR) measurement are performed on Bruker discover D8 diffractometer. Transmission electron microscope (TEM) investigations are carried out on a Philips CM 200 TEM, operated at 200 kV accelerating voltage. The microscope is used in imaging, diffraction, and analytical modes.

3.3. Results and Discussion:

3.3.1. Layer Structure and thickness control Mo/Si MLs:

Fabrication of high reflectivity MLs with good energy band pass depends strongly on nature of interface, density contrast and thickness error. While thickness error from layer to layer in the multilayer stacks depends on the stability of the process parameters, the interface characteristics and density contrast depends on kinetic energy (KE) of the add-atoms. KE of condensed particles is optimized by adjusting flux and energies of sputtered atoms through a systematic variation of process parameters during growth of thin films, bilayers and finally MLs. Desired film quality is obtained after several iterations, by optimizing gas flow rate, pressure, power, target- substrate distance and substrate speed. Some of these results are discussed below.

The influence of argon pressure on the quality of Mo single film is shown in Figure 3.2. Measured XRR profile is fitted using Parratt formalism.[54] For fitting, a low density Mo oxide layer of thickness ~ 45 Å is assumed at the top of Mo thin films. The best fit results reveal the rms surface roughness of oxide layer is in the range of 8 Å for samples Mo-1, Mo-2, Mo-3 and Mo-4. The substrate roughness of 4 Å is assumed in fitting of all samples.

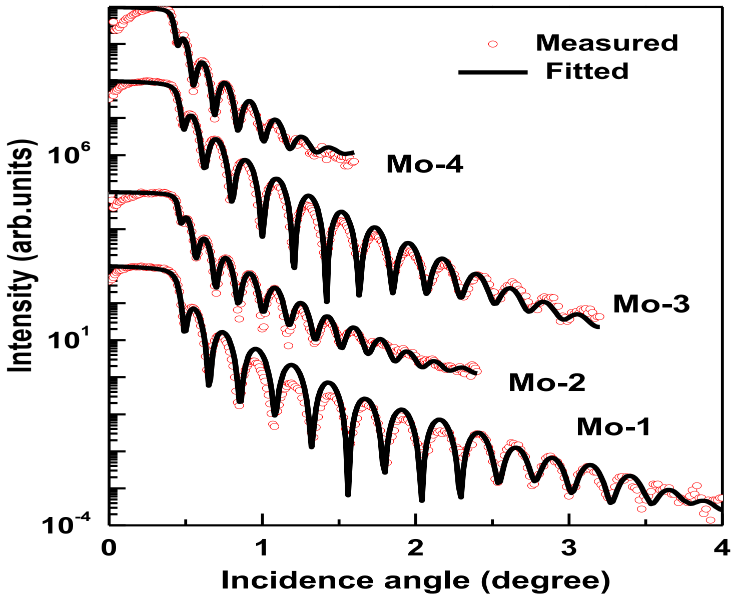

Figure 3.2: Measured and fitted XRR profile at Cu K_α wavelength (λ=1.54Å) for Mo thin films as a function of Ar pressure. The best fit results are given in Table 3.1.

The film thickness, surface roughness and mass density obtained from the best-fit to measured XRR data are shown in Table 3.1.

Table 3.1: Mo film quality in-terms of thickness (t), roughness (σ) and density (ρ) as a function of Ar pressure obtained from the best-fit XRR results of Figure 3.2.

Film	P(mbar)	t (Å)	σ(Å)	ρ(g/cc)
Mo-1	3×10^{-3}	155	3.0	10.2
Mo-2	4×10^{-3}	180	6.0	10.1
M0-3	5×10^{-3}	160	6.5	9.8
Mo-4	8×10^{-3}	175	8.0	8.9

The roughness of film increases with increasing thickness and for same thickness, roughness increases with increasing pressure. Previously it was observed that with increase in working pressure, the growth pattern of sputtered films changes from compact structure to a columnar structure. [19,86,87] The increase in roughness of film at higher gas pressure is attributed to decrease in surface energy of add-atoms during film growth. Similarly, the influence of power, target-substrate distance etc. are examined on the film quality. To realize good interface, the process parameters are optimized for both Mo and Si. In case of Si, we have optimized process parameters by fabricating Si-on-Mo bi-layer to get high contrast from Si-substrate. We varied the RF power of Si, at optimized sputtered-gas pressure of 3×10^{-3} mbar. Fig. *5* shows XRR spectra of Si-on-Mo bilayers fabricated at different RF power (250 to 350W) on Si target, keeping Mo target power constant (150 W). The corresponding best-fit results are tabulated in Table 3. Low surface roughness and high density of Si film is observed at RF power of 300 W (sample No. BL

2).Furthermore, at this power, thickness of interlayer formed due to intermixing of Mo and Si at interface is smaller. As RF power decreases to 250 W (Sample No. BL 1), Si film density decreases and roughness increases. This effect is due to decrease in Si ad-atom kinetic energy as they arrive at substrate. Similarly, as RF power increases to 350 W (sample No. BL 3), although Si density remains unchanged with small increases in roughness (with respect to BL 2), but the interlayer thickness increases significantly. The increase in interlayer thickness is due to increase in inter-diffusion at the interfaces as the Si ad-atoms kinetic energy increases due to increases in RF power. However, for Mo film, the rms surface roughness, σ remains constant. Small variation in Mo thickness, for different samples, is due to variation in interlayer silicide thickness which consumes different amount of Mo for formation of silicides.

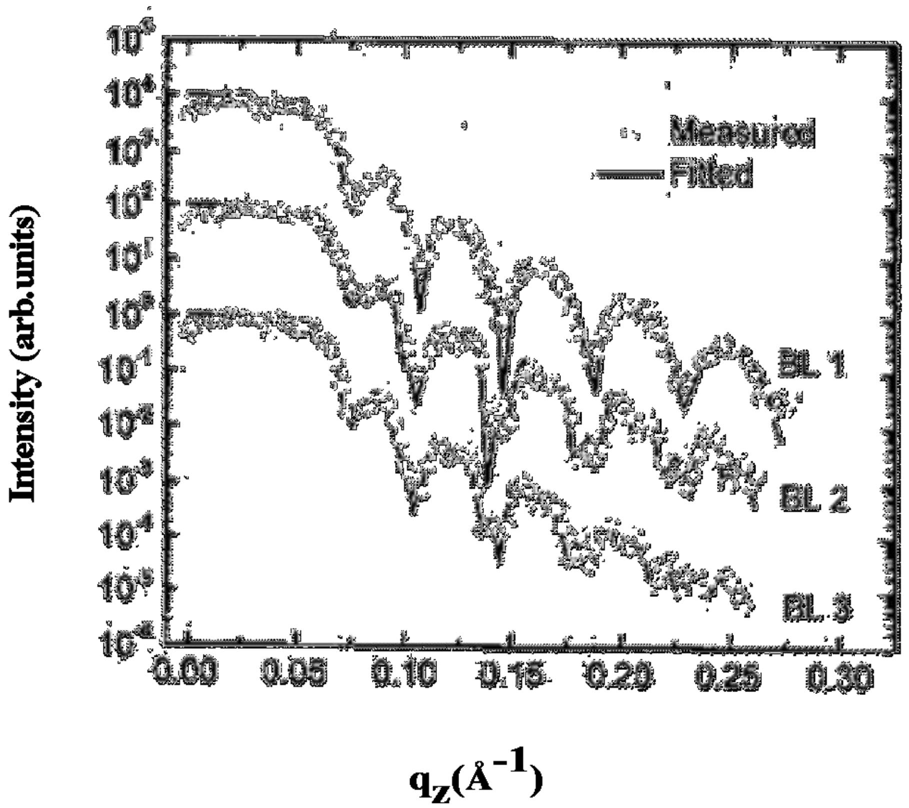

Figure 3.3: Measured and fitted GIXR profile at Cu K_α wavelength (λ=1.54Å) for Si-on-Mo bi-layers deposited at different RF power of Si at a constant sputter gas pressure of 3x10^{-3} mbar. The best fit results are given in Table 3.2.

Table 3.2: Best-fit results obtained from Figure 3.3 for Si-on-Mo bi-layer demonstrating variation in Si film quality as function of RF sputtered power of Si.

Sample	Si RF power (W)	Layer	Fitted parameters		
			t(Å)	σ(Å)	ρ(g/cc)
BL1	250	Si	293	12	1.8
		Si-on-Mo interlayer	5	3	5.7
		Mo	144	5.5	10.2
BL2	300	Si	290	4	2.1
		Si-on-Mo interlayer	6	4	5.8
		Mo	143	5.5	10.2
BL3	350	Si	296	7	2.1
		Si-on-Mo interlayer	12	4	5.8
		Mo	140	5.5	10.2

Similarly, we examined the influence of substrate motion speed and target-substrate distance on the film quality. For the good quality film, the rate of deposition is maintained at 3 Å/s and 0.4 Å/s for Mo and Si, respectively at working pressure 3 x 10^{-3} mbar and 7 seem Ar gas flow rate. For this deposition rate the sputtering power for Mo and Si are 150 W and 350 W respectively. These powers provide appropriate optimized activation energy to the deposited atoms for surface diffusion, at 3 x 10^{-3} mbar sputtered-gas pressure, enabling growth of smooth films. Again, at these average impact energies of sputtered atoms, the inter diffusion at the interface is minimum. Subsequently, for improving film morphology, the geometrical parameters like substrate motion are adjusted. For best film morphology, substrate motion is optimized for Mo and Si as 9.2 mm/s and l.34 mm/s, respectively.

A challenging task during fabrication of ML stacks is to achieve a stable deposition condition for precise control of thickness in atomic scale from layer to layer. This needs that discharge plasma and its distribution over the target should be stable during fabrication of ML, which takes approximately few hours. The key parameters for stable and uniform plasma depend on purity of Ar gas, uniform gas flow over the target, conditioning of vacuum chamber (degassing and quality of vacuum) and a stable plasma power supply. Quality of vacuum in the process chamber is maintained by constantly pumping without breaking vacuum in the chamber. The out-gassing from inner wall of process chamber was pre-conditioned by fabricating test samples for many runs before final fabrication of actual samples. For stable plasma and to avoid contamination from target surface during film growth before fabrications of actual ML samples, the target is pre-sputtered for about 30 minutes. The stabilization of gas flow rate, power, and vacuum is maintained within ±0.01 sccm, ±0.5 W and $\pm 0.02\times10^{-3}$ mbar respectively during the deposition process. For the determination of layer structure, intentionally, we fabricated multilayer samples with lower number of layer pairs for clarity in Kiessig oscillation between higher order Bragg peaks in the x-ray reflectivity pattern. Figure3.3 shows a case study of two Mo/Si MLs with N=10 but different periodicity. The successive higher order Bragg peaks reveal good quality of ML structure. The best-fit results are shown in Table 3.2. For ML-1, the measured full width at half maxima (FWHM) of 1st order Bragg peak is $\Delta q_z = 0.0114\ \text{Å}^{-1}$ which is close to the FWHM of ideal ML structure$\Delta q_z = 0.0111\ \text{Å}^{-1}$. Similarly for ML-2, the measured FWHM of 1st order Bragg peak is $\Delta q_z = 0.0116\ \text{Å}^{-1}$ which is also close to FWHM of real ML structure $\Delta q_z = 0.0114\ \text{Å}^{-1}$. The best-fit results reveal high contrast in density between Mo and Si with interfacial roughness in the range of 2 to 4 Å. There is a presence of interlayer (IL) in between Mo and Si, which is asymmetric in thickness.

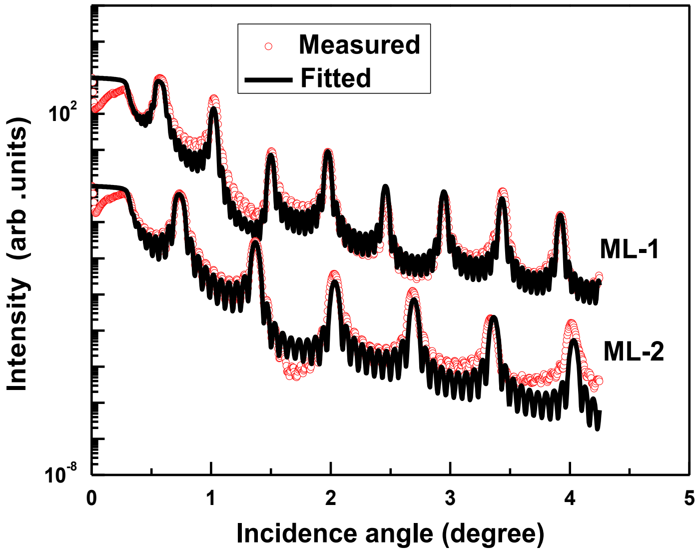

Figure 3.4: Measured and fitted XRR profile at Cu K_α wavelength (λ=1.54Å) for Mo/Si MLs with N=10 and with different periodicity. d=90Å for ML-1 and d=66 Å for ML-2. The best fit results are given in Table 3.3.

After optimizing process parameters by fabricating smaller number of layer pairs, MLs are fabricated with larger number of layer pairs. Figure 3.4 shows the measured and fitted XRR profile of two Mo/Si MLs. ML-3 has N=65 and periodicity d= 68 Å where as ML-4 has N=60 and d= 93.4 Å. Figure 3.4 shows well-defined successive higher order Bragg peaks indicate good quality of ML structure in terms of roughness, thickness error and density contrast. A calculated thickness error of ~ 0.03% per layer is obtained from higher order peak broadening. The best-fit results are shown in Table 3.3. XRR profile is fitted using four layer model taking account of interlayer formation at the both the interface viz. Mo-on-Si and Si-on-Mo. The interlayer arises because of inter diffusion/compound formation at the interfaces of Mo/Si system, which is commonly observed for Mo-Si system.[88]

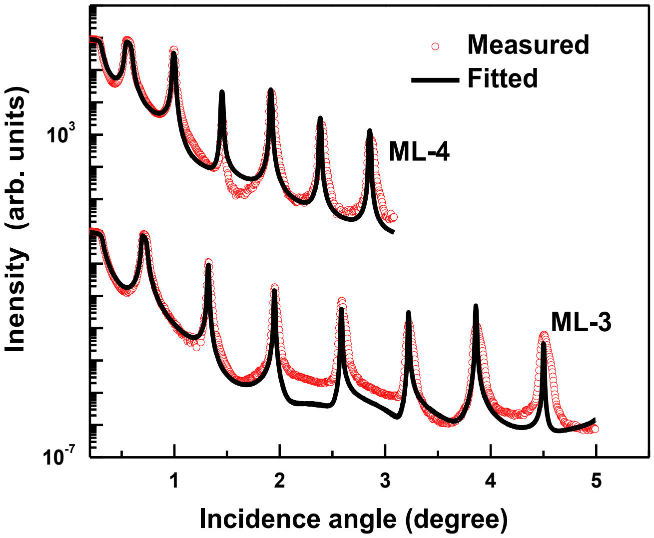

Figure 3.5: Measured and fitted XRR profile at Cu K_α wavelength (λ=1.54Å) for Mo/Si MLs. ML-3 has N=65 and d=68 Å and ML-4 has N=60 and d=93.4 Å. The best fit results are given in Table 3.3.

Table 3.3: Thickness and roughness of the various layers of Mo/Si MLs deduced from the fit of XRR results of Figures 3.4 and 3.5. IL1stands for interlayer at the Mo-on-Si interface, IL2 stands for interlayer at the Si-on-Mo interface. δ is unit decrement of real part of the refractive index.

Sample	Total thickness(Å)	Mo thickness(Å)	δMo(x10^{-6})	Mo roughness (Å)
		IL1 thickness (Å)	δIL1(x10^{-6})	IL1 roughness (Å)
		Si thickness (Å)	δSi(x10^{-6})	Si roughness (Å)
		IL2 thickness (Å)	δIL2(x10^{-6})	IL2 roughness (Å)
ML-1	90.3	28.0	26.0	4.7
		8.9	9.5	3.0
		47.4	6.0	4.0
		6.0	22.8	2.0
ML-2	66.0	16.7	26.0	4.7
		8.0	9.5	3.0
		35.0	6.0	4.0
		6.3	23.8	2.0
ML-3	68	21.0	28.0	5.0
		9.0	9.5	4.0
		31.0	7.6	4.0
		7.0	18.5	2.0
ML-4	93.4	30.4	28.0	5.0
		10.0	7.5	4.0
		44.5	8.0	4.0
		8.5	19.5	3.0

Cross-sectional electron microscopy studies are undertaken to study the interfaces and periodicity of Mo/Si ML. Figure 3.6 shows cross-sectional TEM micrograph of Mo/Si ML-3 with N=65 layer pairs. The dark and light bands correspond to Mo and Si layers respectively. Molybdenum has a higher atomic number (Z = 42) and therefore appears darker as it scatters more electrons than does silicon (Z = 14). ML shows a well defined periodic structure with sharp interface. However, very thin asymmetric interlayers are observed in the zoomed region.

Figure 3.6: Cross-sectional TEM image of sample ML-3. Dark lines correspond to Mo and bright lines to Si.

3.3.2. Lateral uniformity and Reproducibility of Mo/Si MLs:

Desired lateral thickness profile of the coating on large area substrate is obtained by iterative control of pumping port opening, argon flow from two sides of chamber, substrate motion, installation of masking arrangements and optimization of target-substrate distance. Uniform flow of argon across the target is realized by flowing unequal gas flow rate on two sides of targets (along length) and adjusting opening of pumping port. After assuring uniform gas flow, the spatial distribution of sputtered atoms depend upon the geometry of target and target-substrate distance. A planner rectangular magnetron source produces a rectangular-shaped sputtering track.. The spatial distribution of deposition rate profile over a planner rectangular cathode is cosine like structure.[89] The deposition rate is more at centre and decreases systematically at both side along the length. Furthermore, the spatial distribution of deposited flux is strongly dependent on target-substrate distance. As the target-substrate distance increases, the spatial distribution profile becomes uniform over the length of the target. However, as the target-substrate distance increases the deposition rate decreases. Furthermore, the film quality is affected if target-substrate distance is large. There is a trade-off between target-substrate distance which in-turn depends on uniformity and deposition rate, as well as film quality. Thus, the strategy for controlling uniformity over length of target is to use appropriate masking geometry and to optimize target- substrate distance. For the present system, we have optimized target-substrate distance as 70 mm. To average out spatially variation of deposition rate along length of target, we employed different masking arrangements. To evaluate the lateral uniformity of periodicity, initially multilayers are fabricated on small substrates (size 2×3 cm^2) are placed at different positions over the area 300x100 mm^2. Finally, the actual large size multilayers fabricated on float glass with size 300×100 mm^2. Figure 3.7 shows measured reflectivity profile of Mo/Si ML at different positions along the length of substrate which are fabricated using a rectangular masking arrangement in between target and substrate.

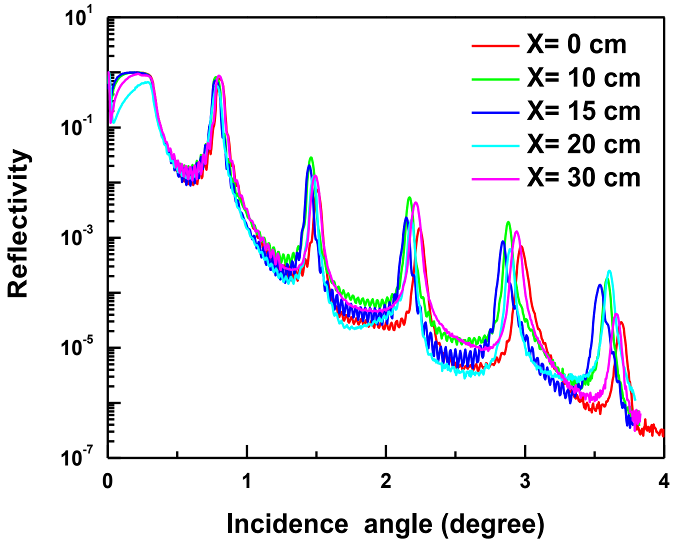

Figure 3.7: XRR profile of Mo/Si MLs with N=20, Γ=0.35 and d=62 Å by placing substrates at different positions (X) along the length of the substrate holder and putting a rectangular mask.

Figure 3.8 shows the periodicity of fabricated multilayer verses distances along the length of target which are obtained from best-fit XRR measurements. In Figure 3.8, it is evident that there is systematic decrease in periodicity in both sides along the length with respect to centre of substrate. This is due to decrease in deposition rate from centre to side along the length of target. The maximum variation in periodicity is (Δd) 1.7 Å.

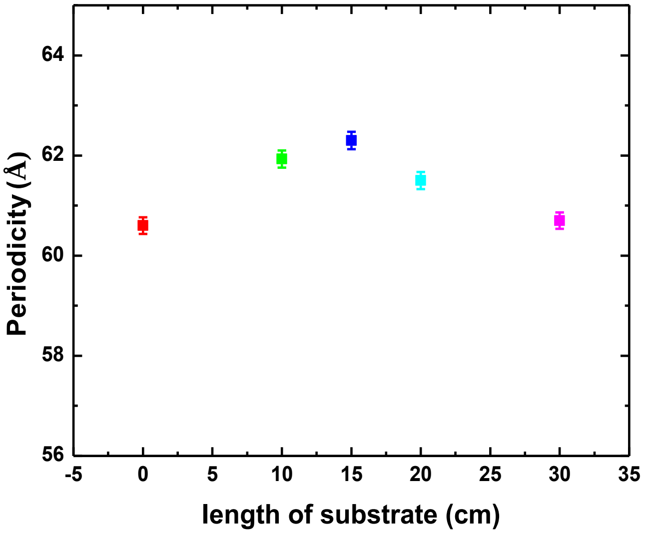

Figure 3.8: Measured lateral variation of periodicity along the length obtained from best-fit results of Figure 3.7.

In order to further minimize spatially variation of deposition rate along the length, we figured the mask, with tapering towards centre. More flux of deposited material at the centre compared to both sides is compensated by adjusting amount of tapering of mask towards centre. Figure 3.9 shows the measured reflectivity profile of Mo/Si MLs at different positions along the length of substrate which are fabricated using a modified masking arrangement with tapering towards centre. The corresponding variation in lateral periodicity which is obtained from the best-fit data is shown in Figure 3.10. The maximum lateral variation in periodicity is within 0.5Å along 300 mm length of target. Furthermore, the linear motion of the substrate across the full opening of mask averages out the spatial variation of the deposition rate in the motion direction (i.e. along the width of target). In our present deposition system, the maximum width of sample is 100 mm. This limitation in sample width is to avoid cross talk between the targets during deposition.

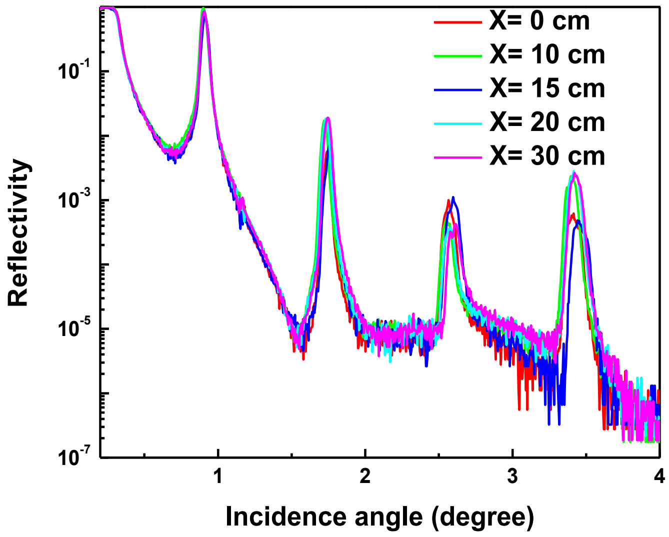

Figure 3.9: XRR spectra of Mo/Si MLs with N=65. Γ=0.45 and d=52 Å by placing substrates at different positions (X) along the length of the substrate holder and using a mask with tapering towards center of target.

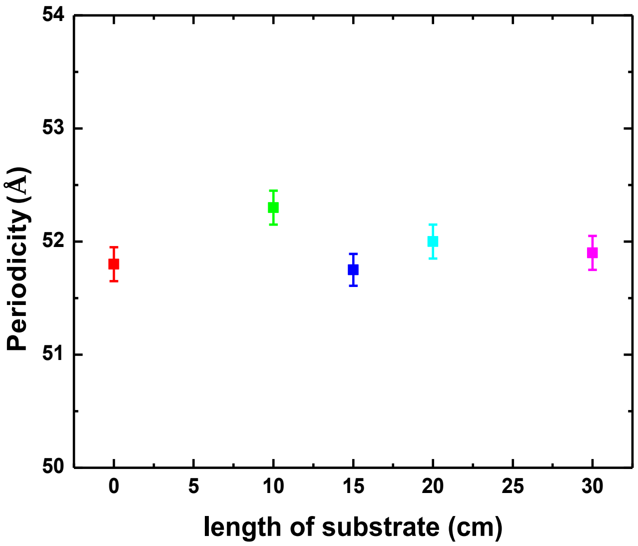

Figure 3.10: Measured lateral variation of periodicity along the length obtained from best-fit results of Figure 3.9.

Reproducibility is the crucial issue for larger area multilayer for device applications. Our pre-conditioned system ensures reproducibility of system in-term of density contrast, interface quality and thickness control from run-to-run. A typical example of reproducibility of fabricated multilayers from run-to-run is shown in Figure 3.11. Here, we show three different deposition runs keeping number of layer pair fixed at N=10. The identical critical angle and similar reflectivity of 1st order Bragg peak of three samples indicate insignificant variation in film density. The best-fit results reveal identical interface quality for all the samples. Moreover, best-fit results reveal the variation in periodicity from run to run is better than 0.5Å.

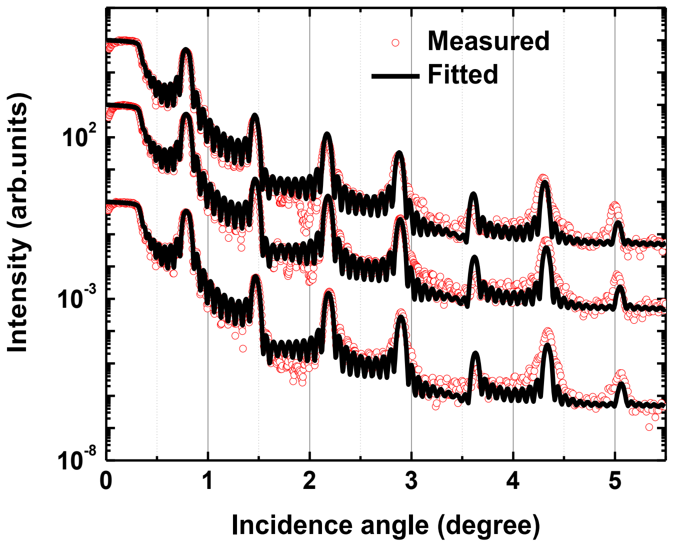

Figure 3.11: XRR spectra of Mo/Si MLs with N=10, and d= 61 Å deposited from run-to-run under identical experimental conditions.

3.3.3. Soft x-ray performance of Mo/Si MLs:

The actual performance of MLs is tested using reflectivity beam line on Indus-1 SR source. Figure 3.12 shows the angle versus reflectivity scan of ML-3 with d=68 Å and N=65 layer pairs at a wavelength of 127 Å. The ML has 63% peak reflectivity at an incidence angle of 71°. In inset, wavelength versus reflectivity scan measured at a Bragg angle of 72.5° is presented. The ML with suitable varying periodicity will be used for potential application in the wavelength range of 126 -150 Å. The 63% of reflectivity obtained is comparable with 69% peak reflectance reported on standard Mo/Si system.[90] The spectral width of ML-3 is 2.3eV. Mo/Si ML would be used as a polarizer and analyzer in soft x-ray region because of high throughput and polarizing power.

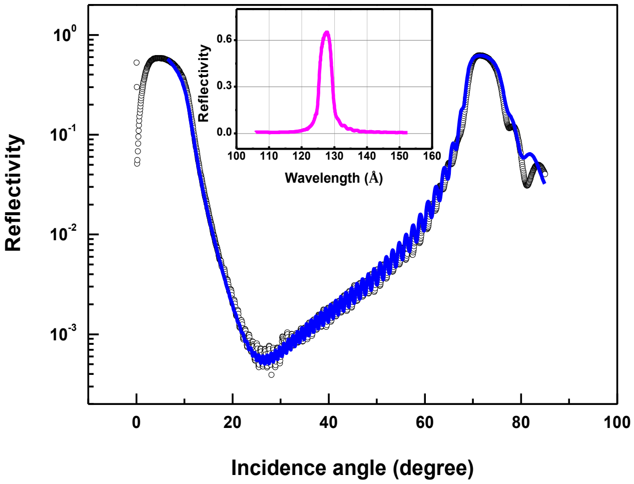

Figure 3.12: Measured (open circle) and fitted soft x-ray reflectivity (solid line) profile of Mo/Si ML (sample No. ML-3) at the wavelength λ = 127 Å using synchrotron radiation. Inset shows wavelength versus reflectivity curve measured at angle of incidence of 72.5°.

Figure 3.13 shows the angle versus reflectivity scan of ML-4 which is designed to use as a polarizing element at wavelength of 130 Å with d= 93.4 Å and N= 60 layer pairs. This sample has Bragg peak at quasi Brewster angle 45^0 at wavelength of 130 Å. The spectral width of ML-4 is 5.36 eV. In sample ML-4 numbers of layer pairs are optimized to get maximum s-reflectance to p-reflectance ratio.

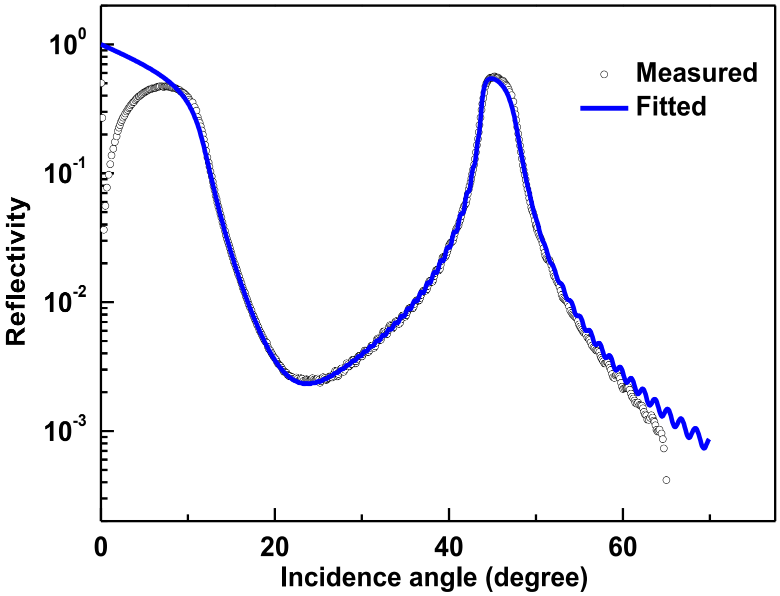

Figure 3.13: Measured (open circle) and fitted soft x-ray reflectivity (solid line) profile of Mo/Si ML (sample No. ML-4) at the wavelength λ = 130 Å using synchrotron radiation.

3.4. Conclusions

High reflectivity and large area Mo/Si MLs are developed using specially designed magnetron sputtering system. The process parameters are optimized for growth of thin film suitable for x-ray ML fabrication. Mo/Si MLs are fabricated with rms interface roughness in the range of 2 to 5 Å. The lateral variation in periodicity of ML is minimized to 0.5Å over 300×100 mm^2 area by proper masking arrangement, substrate motion and choosing appropriate system configuration. The run-to-run variation in periodicity and thickness errors are less than 0.5 Å and 0.03% per layer, respectively. Reflectivity of more than 60% is routinely achieved at the wavelength above the silicon L-edge (~124 Å).

Chapter 4.

Thermal stability and reflective characteristics of W/B_4C multilayers for EUV-SXR application

In this chapter, we discuss the normal incidence reflectance of W/B_4C *MLs near the B K-edge. We have also investigated thermally induced structural changes and its detrimental effect on reflectivity performance. An effort has been made to understand the cause of period variation due to annealing. Different ML samples were deposited using magnetron sputtering. Hard x-ray reflectivity, grazing incidence x-ray diffraction using both lab and synchrotron radiation sources and soft x-ray reflectivity measurements were performed. The results obtained are presented in this chapter.*

4.1. Introduction:

Multilayer (ML) mirrors consisting of alternating layers of high and low electron density contrast are used as artificial Bragg reflectors in x-ray region.[10] Different ML combinations are studied so far in the literature. The advantage of using the ML optics is that they can be operated near normal incidence geometry which improves resolution and ML period thickness can be tailored according to operating wavelength. Mo/Si ML is the most studied combination in the extreme ultraviolet region. A near normal incidence reflectivity of >60% can routinely be achieved using Mo/Si ML at wavelengths above Si L-edge (124 Å).

The motivations for studying the optics for shorter wavelengths are that the imaging at shorter wavelengths can provide an increase in resolution and increases the penetration depth. ML mirrors near the B K-edge are of interest for x-ray analysis of boron content in doped semiconductors, plasma diagnostics and lithography. Few ML combinations like Ru/B_4C[15], La/B_4C [17, 91-93], Mo/B [94], Mo/B_4C [31,32] and Pd/B_4C[16] were studied near the B K-edge. The ML combinations were chosen based on selection criteria i.e., high optical contrast between absorber and spacer elements as well as low absorption in both spacer and absorber elements. Even though there is high optical contrast between W and B_4C, because of high absorption in W as compared to other elements like Ru, Mo and La, this is an unstudied combination near the B K-edge.[95] The high absorption in W film limits the total number of layer pairs contributing to reflectivity. We have chosen W/B_4C ML as a reflecting mirror near the B K-edge because B_4C can form smooth interfaces with W and tendency for interface reaction is less in W/B_4C as compared to Ru/B_4C and Mo/B_4C.[32, 33, 96]

MLs exposed to high intense synchrotron radiation showed quick rise in temperature. Recent studies on Mo/Si[30] MLs exposed to intense pulsed extreme ultraviolet source showed that the silicide formation causes for irreversible structural changes. The observed damage mechanism is similar to that observed during annealing treatments. Study of the thermal stability of any optical element is important as it is exposed to high power density synchrotron/x-ray free electron lasers radiation. The emerging technology requires improved optical components and therefore lots of research is going on to find out high stability multilayer mirrors. Many ML systems are investigated on this context.[25, 31, 97, 98] Thermal loads on optics causes interdiffusion changing the ML period thickness and reduce the optical contrast. The reduction in optical contrast results in reflectivity drop and change in ML period thickness causes change in optimally reflected wavelength (or incidence angle). W/B_4C MLs undergo period thickness changes on thermal annealing. Jankowski *et al*.[33] could not explain the observed period thickness changes up on annealing using transmission electron microscopy and Auger electron spectroscopy. A detailed study is essential to understand the period thickness changes in W/B_4C MLs.

In this chapter, we explore the application of W/B_4C ML as a stable reflecting mirror near the B K-edge. A detailed study is carried out to understand the period thickness changes in W/B_4C MLs up on thermal annealing. The structural changes due to annealing were studied using XRR. Near normal incidence reflectance measurements in the vicinity of B K-edge were performed using Indus-1 soft x-ray reflectivity beamline. Annealing products were studied using lab based as well as synchrotron radiation based GIXRD.

4.2. Experimental Methods:

4.2.1. Sample preparation:

W/B_4C MLs were deposited using magnetron sputtering system. The B_4C target with purity 99.5% was used at constant RF power of 700 watts and the W target with purity 99.95% was used at constant direct current power of 100 watts. The deposition was carried out under Ar ambient at constant pressure of 0.5 Pa. The ML samples were coated on ultrasonically cleaned, first in acetone and then in methanol, Si (100) wafer. The ML sample consists of 50 bilayers (N) with period thickness (d) of 34.7 Å where W layer thickness is ~10 Å and B_4C layer thickness is ~24.7 Å is used to study the normal incidence reflectance near the B K-edge. Four W/B_4C ML samples consisting of 20 layer pairs, with fixed period thickness, d~ 38 Å, and layers thickness ratio, Γ(ratio of W layer thickness to period thickness) = 0.21, 0.27, 0.46 and 0.62, were used to study the thermally induced structural changes. These MLs were named as ML-1 (Γ= 0.21), ML-2 (Γ= 0.27), ML-3 (Γ= 0.46) and ML-4 (Γ= 0.62).

4.2.2. Heat treatments:

The ML samples were placed in an alumina boat inside the quartz tube. The quartz tube was pumped to a base pressure of ~10^{-4} Pa. The furnace reached the set temperature within 25 minutes. Each ML sample was cut into two pieces, one was kept for reference and other was sequentially annealed from 500 to 900 °C in step of 100 °C. The sample was heated for 1 h at respective temperatures and then cooled down to room temperature over several hours.

4.2.3. XRR measurements:

XRR measurements were performed at Cu $K_\alpha$radiation (λ=1.542 Å) on Bruker Discover D8 diffractometer with Ge (220) two bounce monochroamtors. XRR measurements were performed using 100 μm slits in incident beam and 200 μm slits in reflected beam.

4.2.4. GIXRD measurements:

GIXRD measurements were performed using both lab source and synchrotron radiation. Lab based GIXRD measurements were performed using Cu $K_\alpha$radiation (λ=1.542 Å). A 200 μm slit is used in incident beam and a long solar slit to collect the data in diffraction beam arm. Synchrotron radiation based GIXRD spectra were taken at Indus-2 synchrotron source on the angle dispersive x-ray diffraction beamline, (BL-12) at photon energy of 13 keV using image plate area detector (Mar-345 dtb).[62] The radiation energy and distance between the sample and detector were accurately calibrated using the diffraction pattern of LaB_6 NIST standard.

4.2.5. Soft x-ray reflectivity measurements:

The angle dependent reflectance measurements in soft x-ray region were carried out using reflectivity beamline at Indus-1 synchrotron facility. SXR scans were performed between grazing incidence angle of 0^0 and 85^0 to study the variation in SXR with annealing temperature. SXR measurements were performed in the wavelength region of 60 -70 Å.

4.3. Results and Discussions:

4.3.1. Study carried on normal incidence W/B_4C mirror:

4.3.1a. Hard X-Ray Reflectivity (XRR):

Structural evaluation of W/B_4C ML with temperature has been studied using XRR. The measured and fitted XRR curves of as-deposited and annealed W/B_4C ML sample are shown in Figure 4.1. The Bragg peaks shifted towards smaller angle after 500 °C annealing suggests the increase in ML period thickness. The XRR data was fitted using Parratt formalism.[54] The interface roughness was taken into account according to Nevot-Croce model.[24] The best fitted model suggests that ML period thickness increases from as-deposited value of 34.6 ± 0.1 Å to 35.0 ± 0.1 Å after 500 °C annealing. However, the ML period thickness remains within the experimental error after annealing at 700 °C and above. We observed broadening at higher order

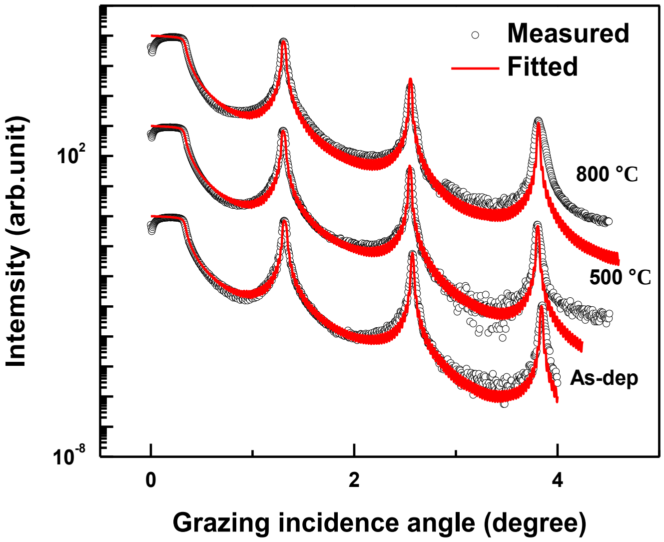

Figure 4.1: Measured (open circle) and fitted (solid line) XRR results of the W/B_4C ML structure sequentially annealed from 500 to 800 °C in steps of 100 °C for 1 h at each step.

Bragg peaks after 700 °C annealing which suggests the increase in interface width. The first Bragg peak reflectivity was reduced from 70% to 64% after 800 °C annealing. We assumed two-layer model consists of W and B_4C to fit the XRR data. The best fitted model reveals that W layer thickness is 10.3±0.5 Å, B_4C layer thickness is 24.3±0.5 Å, root mean square (rms) roughness for W-on-B_4C interface is 3 Å and B_4C-on-W interface is 4.7 Å in as-deposited sample. The density of B_4C is 2.29 g/cc and density of W is 16.8 g/cc for as-deposited sample. The rms interface roughness changed to 3.2 Å and 6.2 Å for W-on-B_4C and B_4C-on-W interfaces respectively after 800 °C annealing.

4.3.1b. Grazing Incidence X-Ray Diffraction (GIXRD):

GIXRD was used to investigate the annealing products. [99] GIXRD measurements performed using Cu Kα (1.54Å) radiation on W/B_4C ML at fixed incidence angle of 1^o are shown in

Figure4.2. GIXRD pattern consisted of two broad peaks corresponding to W (110) and (211), which indicates that the W layer is polycrystalline with very small grain size. A sharp peak at the centre of GIXRD pattern was observed due to asymmetric reflection from Si substrate. After 800 °C annealing no visible changes were observed as compared to as-deposited sample.

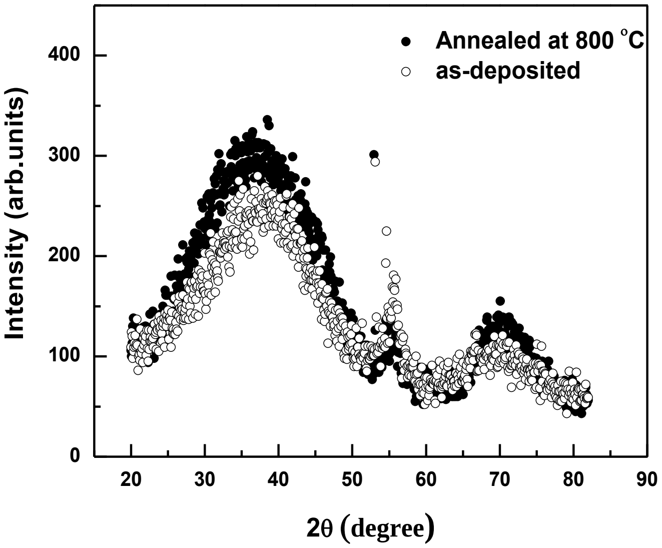

Figure 4.2: GIXRD pattern of W/B_4C ML measured at λ=1.542 Å at fixed incident angle of 1°. Open and filled circles represent the measured GIXRD data before and after 800 °C annealing respectively.

4.3.1c. Soft X-Ray Reflectivity (SXR) near the B K-edge:

Normal incidence soft x-ray reflectivity measurements are more sensitive to period thickness and compositional changes. The SXR measurements performed near the B K-edge are shown in Table 4.1. W/B_4C ML structure yielded a near normal incidence reflectivity of ~8% and changed to ~ 7% at 68 Å wavelength after 800 °C annealing.

Table 4.1: ML period thickness d, peak reflectivity R, peak wavelength λ, and corresponding Bragg angle θ_{Bragg} as a function of annealing temperature T.

T (°C)	d (Å)	θ_{Bragg} (deg)	λ (Å)	R(%)
as-deposited	34.6±0.1	76.54	67.0	7.4
		81.66	68.0	7.6
500	35.0±0.1	73.82	67.0	8.1
		77.45	68.0	8.3
		82.48	69.0	8.1
600	35.0±0.1	73.74	67.0	8.3
		77.29	68.0	8.3
		82.43	69.0	8.1
700	34.9±0.1	72.98	66.5	7.4
		78.25	68.0	7.6
800	34.9±0.1	74.35	67.0	7.1
		78.33	68.0	7.1

SXR measurements at constant grazing incidence angle of 76.54^0 as a function of wavelength at different annealing temperatures are shown in Figure 4.3. The measured SXR shifted towards higher wavelength after 500 °C annealing indicating increase in ML period thickness. The ML period expansion observed in SXR measurements is in good agreement with XRR measurements. The Bragg peak shifted towards shorter wavelength at 700 °C and above annealing temperatures. The slight change in ML period thickness during the annealing treatments is due to atomic rearrangements or due to stress relaxation. W/B_4C ML showed two types of period thickness changes, one is period expansion up to 600 °C annealing and other is period contraction above 600 °C annealing.

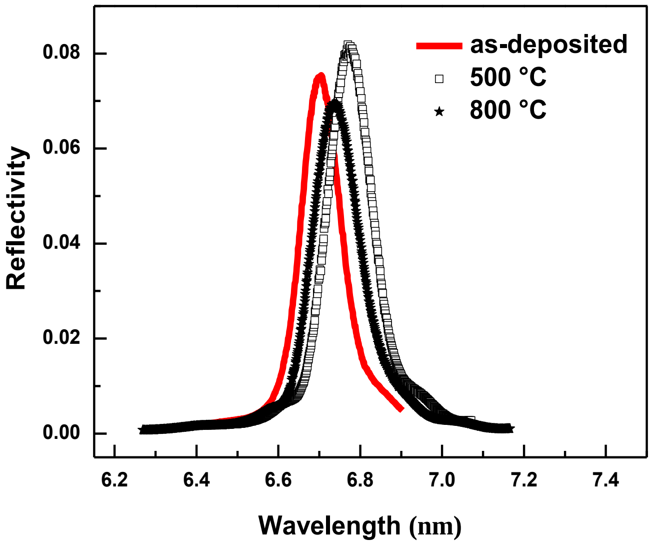

Figure 4.3: SXR data measured as a function of wavelength at fixed incidence angle of 76.54 degree. Continuous line, open diamond and open circles represent the SXR data of as-deposited, annealed at 500 °C and 800 °C respectively.

SXR measurements performed on as-deposited and after 500 °C and 800 °C annealing sample at wavelength of λ= 67 Å along with best fitted model are shown in Figure 4.4. SXR measured data was fitted with the structural parameters derived from XRR data. The SXR data was fitted with two-layer model. During fitting, no interlayer formation was observed even at higher annealing temperature. This might be due to weak interface reaction between W and B_4C.

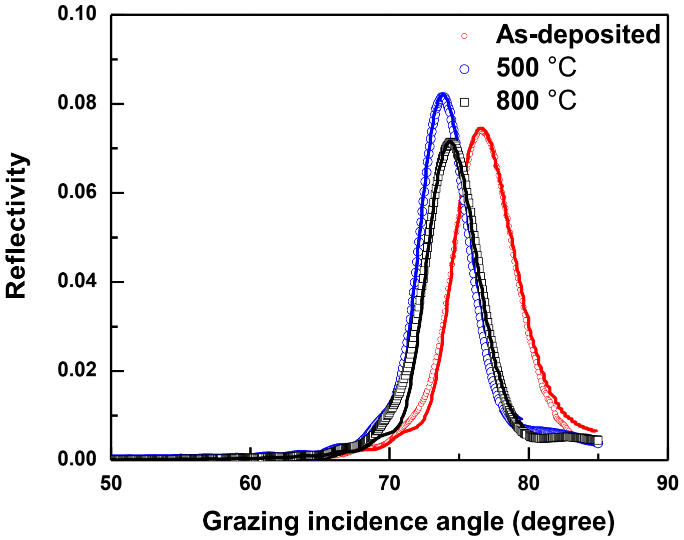

Figure 4.4: Measured and fitted SXR data of as-deposited and annealed sample at 500 °C and 800 °C at 67Å wavelength. The open circle, filled circle and open diamond represents the measured SXR data of as-deposited sample, annealed at 500 °C and 800 °C respectively and continuous line represents the fitted data.

The reflectivity variation also gives the information about ML structural changes with annealing temperature. Figure 4.5 shows the measured SXR as a function of annealing temperatures at wavelength of λ= 68 Å. The increase in peak reflectivity after 500 °C annealing as compared to as-deposited sample is due to increase in ML period thickness. The reduction in peak reflectivity after 700 °C was observed due to increase in interface rms roughness.

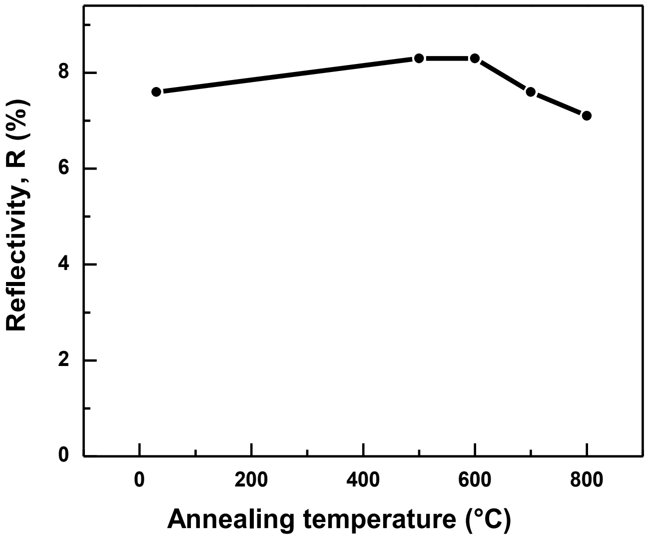

Figure 4.5: The measured SXR as a function of annealing temperature measured at 68 Å wavelength.

La/B_4C ML structure gives highest reflectivity (~40%) as compared to other material combination studied so far near the B K-edge.[91,93] The disadvantages of using this combination are that La is not a stable material, high chemical reaction between La and B_4C, tendency to form products like LaB_6, and LaC_2.[92] A near normal incidence reflectivity of ~20% was obtained using Ru/B_4C[15] ML structure but this combination is stable up to 250 °C only. Annealing at 500 °C for 10 h causes the reflectivity drops to ~4%. More recently, a near normal incidence reflectivity of ~25% was obtained using Mo/B_4C ML combination consisting of 300 bilayers at wavelength of λ= 67 Å.[31] Thermal stability studies carried out on the same combination consisting of 60 bilayers suggested significant drop in reflectivity at temperature higher than 600 °C. The measured reflectivity of Mo/B_4C structure drops from ~6.3% to 2.8% after 900 °C annealing. In the present study, a near normal incidence reflectivity of ~8.3% was observed at wavelength of λ= 68 Å. A little drop in reflectivity (~ 1%) after 800 °C annealing was observed.

On comparing the annealing performance of W/B_4C it can be said that this combination shows highest thermal stability hence very much suitable for high heat load applications of future FEL like sources.

4.3.2. Study of thermally induced structural changes in W/B_4C MLs:

The period expansion observed on annealing has been observed earlier also by Jankowski et al. [33] No one has given a clear reasoning of the observed changes. To understand the period thickness change and influence of the ratio of W to B_4C layer on the annealing performance, we prepared few more samples consisting of 20 layer pairs, with fixed period thickness, d~ 38 Å, and different layers thickness ratio, Γ(ratio of W layer thickness to period thickness) = 0.21, 0.27, 0.46 and 0.62,. These MLs were named as ML-1 (Γ= 0.21), ML-2 (Γ= 0.27), ML-3 (Γ= 0.46) and ML-4 (Γ= 0.62).

4.3.2a. XRR results:

The measured and simulated XRR curves of W/B_4C ML samples ML-1 at different annealing temperatures are shown in Figures 4.6. From Figure 4.6, it is clear that no visible changes in reflectivity profile is observed and only Bragg peaks shift towards smaller angle after annealing which suggest increase in ML period thickness.

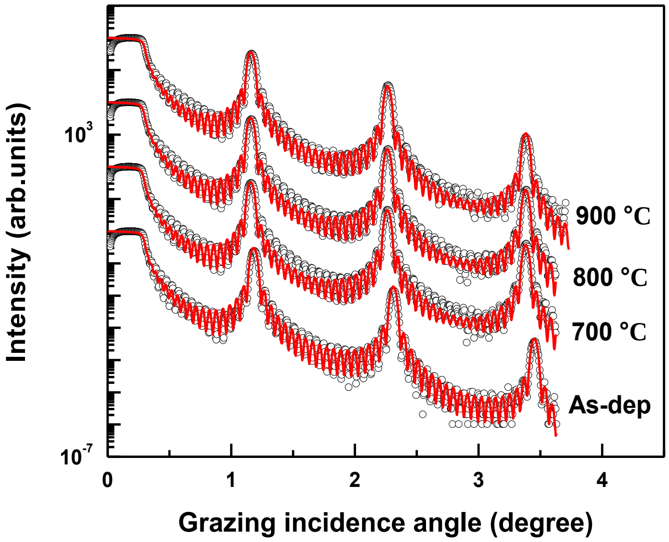

Figure 4.6: Measured (open circle) and fitted (solid line) XRR curves of the W/B_4C ML sample ML-1 after annealing at the temperatures indicated on the plot.

The measured and simulated XRR curves of W/B_4C ML samples ML-2 and ML-3 at different annealing temperatures are shown in Figures 4.7 and 4.8, respectively. In Figure 4.7, the third Bragg maximum disappears after 900 °C annealing. In Figure 4.8, the second Bragg maximum disappears and reappears as annealing proceeds. In general nth order Bragg reflection is suppressed if thickness ratio is 1/n due to phase cancellation of reflected amplitude from each interface.[100] The successive appearance and disappearance of Bragg maxima implies redistribution of atomic density within bilayer connected with the displacement of interface as annealing proceeds, which is in consensus with other reports.[101] Depending upon the initial Γ, different Bragg maxima disappear at different annealing temperatures. From Figure4.7, it is clear that the third Bragg maxima disappear after 900 °C annealing, indicating that Γ changes from 0.27 to 0.33. On the other hand no significant change in reflectivity of the first order Bragg peak could be detected; the peaks remains sharp but shift to lower angles (or higher d values). We interpret the results using two layer model consisting of W and B_4C. Simulated parameters suggested that thickness of the W layer increases from 10.4 ±0.5 to 13.0 ±0.5 Å while that of the B_4C layer decreases from 28.0±0.5 to 26.0 ±0.5 Å. The best fit for the measured data shown in Fig 4.7 is obtained for a root mean square (rms) roughness value of 2.6 Å for both the interfaces of W layer i.e., W-on- B_4C and B_4C-on-W. From Figure4.8, it is seen that the second Bragg maxima disappear after 700 °C annealing, indicating that Γ changes to 0.5. After annealing at 500 °C, Bragg peaks shift to lower angle indicating increase in period thickness. After annealing at and above the 700 °C, Bragg peaks shift to higher angles indicating decrease in period thickness. Simulated parameters suggested that thickness of the W layer increases (up to 1.7 Å) while that of the B_4C layers decreases (up to 2.1 Å).

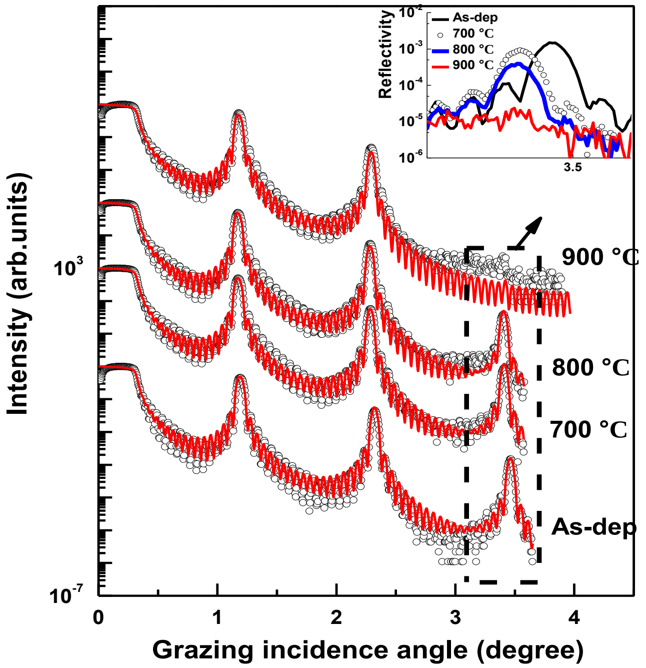

Figure 4.7: Measured (open circle) and fitted (solid line) XRR curves of the W/B_4C ML sample ML-2 after annealing at the temperatures indicated on the plot. In the inset, shows the development of third Bragg maxima with annealing temperature.

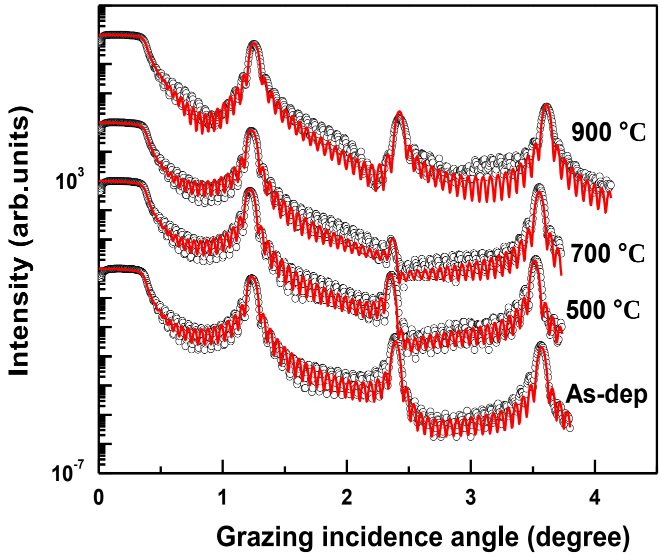

Figure 4.8: Measured (open circle) and fitted (solid line) XRR curves of the W/B_4C ML sample ML-3 after annealing at the temperatures indicated on the plot.

Figure 4.9 shows the measured and simulated XRR curves for as-deposited and annealed W/ B_4C ML sample ML-4. The ML period thickness determined form the position of Bragg peak was 38.5±0.1 Å. The measured first order Bragg peak reflectivity was 42 % and all peaks were sharp in as-deposited ML sample. After annealing at and above 600 °C, Bragg peaks shift to higher angles indicating decrease in period thickness. The first Bragg peak reflectivity changed to 16 % and broadening in Bragg peaks was observed after 800 °C annealing. These changes suggested that ML sample has undergone significant structural changes like increase in inter layer roughness, interdiffusion or interlayer coarsening. We interpret the XRR spectra at 600 °C and higher annealing temperatures, using four layer model consisting of W and B_4C separated by tungsten carbide or tungsten boride layers. The best fitted model suggested the formation of interlayer of thickness 8 ±0.5 Å and 13 ±0.5 Å per period after the 600 °C and 800 °C annealing respectively. The simulated parameters are shown in Table 4.2. It is clear that the W plus interlayer thickness increases from 24.0 ±0.5 to 28.0±0.5 Å while that of the B_4C layer decreases from 14.5±0.5 to 8.0±0.5 Å.

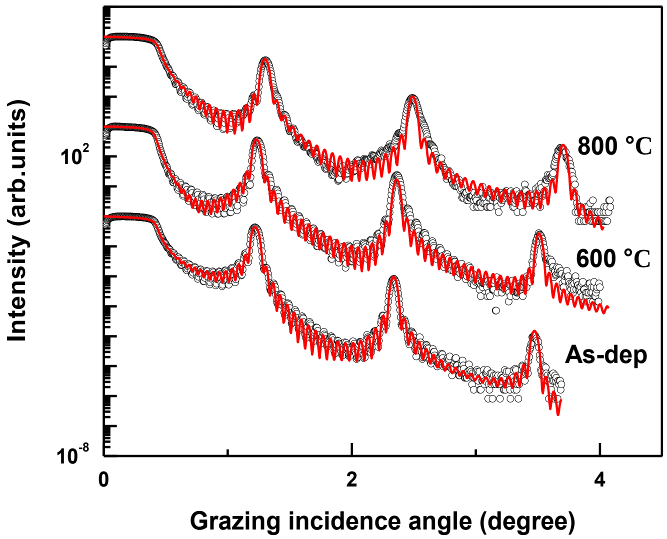

Figure 4.9: Measured (open circle) and fitted (solid line) XRR curves of the W/B_4C ML sample ML-4 after annealing at the temperatures indicated on the plot. The parameters of theoretical simulations are given in Table 4.2.

The ML period thickness and the real part of refractive index (δ) of the W layer decreases by 6.5% and 12.1% respectively after 800 °C annealing. The decrease in δ of W plus interlayer suggested that B or C (or both) atoms diffuse into the W layer causing an interlayer formation during annealing treatments. This B or C content increase causes the increase of thickness of the W layer.[102,103] In W/ B_4C ML system as W and B_4C layer are in direct contact there is possibility of formation of borides and carbides even at low processing temperatures.[96,104] Thermodynamically W and B_4C are expected to react.[105] Tungsten forms two carbides (WC, W_2C) and four borides (WB, W_2B, W_2B_5, WB_4). An experimental phase diagram published by

E. Rudy et al.[106] suggested that W can react with B and C and form stable borides and carbides and no ternary compounds. The W layer thickness can increase from 1.0 to 6.5 Å when 6.5 Å thick B or C layer gets consumed in to it. The observed change (4.0 Å) is within the expected changes.

Table 4.2: Structural parameters derived from the simulation of XRR curves of W/B_4C ML with thickness ratio, Γ=0.62. d_{B_4C}, d_W and d are thicknesses of the B_4C, W (as-deposited) or the mixture of W plus carbides/borides (in annealed samples) layer and ML period, respectively. δ is real and imaginary parts of the complex refractive index n=1-δ+iβ and σ is the rms interface roughness.

parameter	As-dep	600 (°C)	800 (°C)
d_W (Å)	24.0±0.5	26.0±0.5	28.0±0.5
$\mathbf{d_{B_4C}}$(Å)	14.5±0.5	12.0±0.5	8.0±0.5
d (Å)	38.5±0.1	38.0±0.1	36.0±0.1
δ_W ($X10^{-6}$)	40±1.6	36±1.4	35±1.4
$\boldsymbol{\delta_{B_4C}}$($X10^{-6}$)	6.8±0.27	6.8±0.27	8.3±0.30
σ (Å)	5.5	6.8	7.5

The derived change in period thickness on annealing as obtained by fitting the measured XRR data is shown in Figure 4.10. The derived ML period thickness changes, yielding information on the process of interlayer formation.

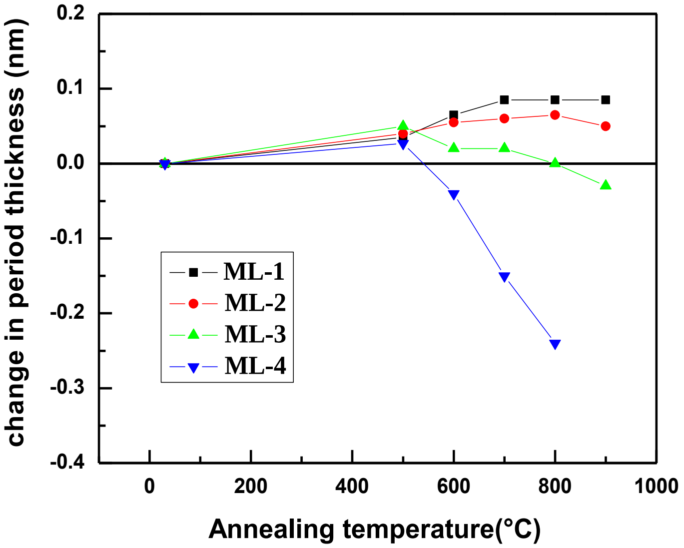

Figure 4.10: ML period thickness changes as a function of annealing temperature in various W/B_4C MLs. The as deposited values of thickness ratio, Γ in corresponding ML are indicated on the plot.

W/B_4C MLs have undergone different period thickness changes depending upon the initial Γ. MLs with the W layer thickness less than the B_4C layer, show period expansion while those with the W thickness greater than or close to the B_4C layer show period expansion initially and then compaction as annealing proceeds. Bulk densities and molar volumes of existing tungsten carbides and borides suggested that period compaction in W/ B_4C MLs due to the formation of compounds at an interface.[96,107] An observed expansion in W/B_4C MLs when the W layer thickness less than the B_4C layer may be due to low density compound formation or mixed phase compounds like WBxCy. The simulated parameters of reflectivity profile suggested that decrease of refractive index and increase in the thickness of W layer with annealing. The W layer thickness increases when C or B atoms are consumed into it. An expansion in the dense W layer due to addition of C and Si atoms at elevated temperatures was also observed in W/C and W/Si

MLs.[101-103] Therefore W plus interlayer layer grows at an expense of the B_4C layer. The nature of grown interlayer is different in different MLs, resulting in net expansion or compression of period thickness. Period thickness changes in W/B_4C MLs can be related to initial B_4C layer thickness. MLs have shown maximum period expansion of 2.2% when B_4C layer thickness is greater than 20 Å and not much loss in reflectivity. MLs with B_4C layer thickness less than 20 Å show net compression which increase with reduction in B_4C layer thickness. Hence it can be concluded that ML with B_4C layer thickness more than 20 Å show better thermal stability.

4.3.2b. GIXRD results:

GIXRD measurements performed using Cu K_α (1.54Å) radiations on W/B_4C MLs ML-3 and ML-4 at fixed incidence angle of 1° are shown in Figure 4.11. We observed broadening in diffraction peaks and could not see any new phases peaks after annealing. In spite of increasing data collection time it was not possible to get better statistics.

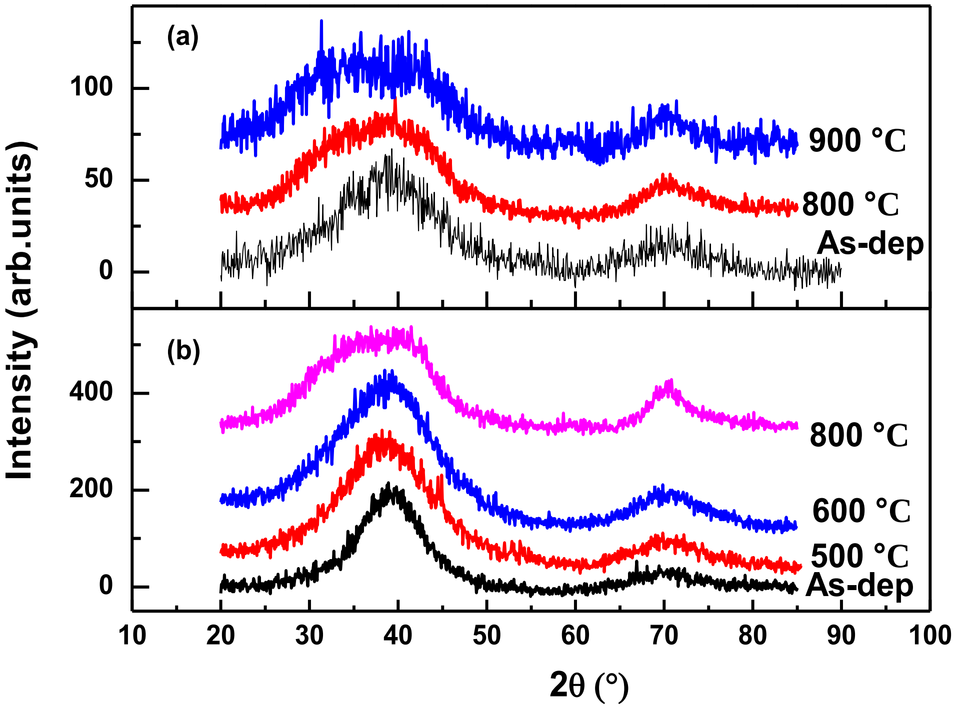

Figure 4.11: GIXRD pattern of W/B_4C MLs (a) ML-3 and (b) ML-4 measured at λ=1.542 Å at fixed incident angle of 1°.

To improve the diffraction signal GIXRD measurement were performed using synchrotron radiation. GIXRD measurements performed on W/B_4C MLs at photon energy of 13 keV are shown in Figure 4.12. GIXRD data is taken at an incidence angle larger than critical angle. The measured data is converted for 8 keV photon energy to compare diffracted peak positions with lab source data.[108] Figure 4.12a, displays the GIXRD pattern obtained from the ML sample ML-2 with the W layer thickness per period is 10 Å. In as-deposited sample the weak and broad features centered at 36.0°, and 65.8° are corresponds to W (110) and W (211) respectively in the W/B_4C ML structures. These peaks are broad and away from bulk W peak positions because of disordered and nanocrystalline nature of the thin W layer.[115] Figures 4.12b and 4.12c, corresponds to GIXRD pattern obtained from the ML samples ML-3 and ML-4 respectively. The peak widths and position changed in these samples as the crystallite size increases. The peak position of the diffraction maximum increases from 36.0º to 39.4º and from 65.5.0º to 70.4º indicating that lattice parameter is approaching bulk value. We interpret this shift, which is toward bulk W (110) reflection at 40.3º and W (211) reflection at 73.2º, due to increasing structural long range ordering associated with increasing W layer thickness.[109]

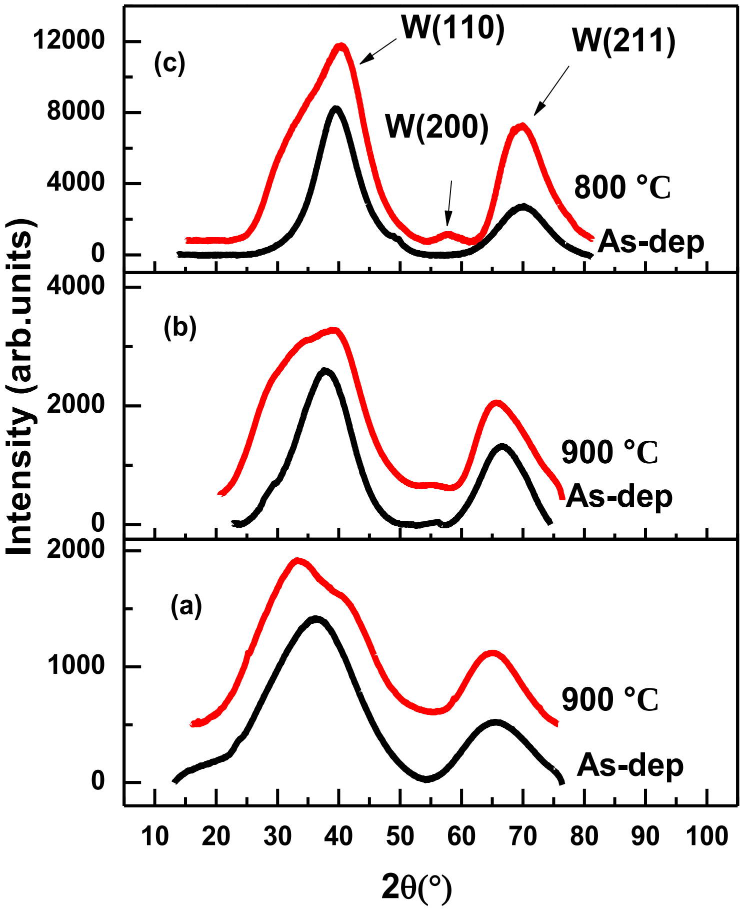

Figure 4.12: (a) GIXRD profile of W/B_4C ML sample ML-2 (b) sample ML-3 and (c) sample ML-4. Diffraction peaks coming from bare Si substrate and corresponding annealing temperatures are indicated on the plot.

The GIXRD pattern obtained from annealed ML samples undergone shift in Bragg peak to higher angles indicating further reduction in lattice parameter. It is also clear from Figure 4.12, that for all the annealed ML samples, GIXRD pattern shows the presence of new shoulder in the diffraction peak. The presence of new shoulder in the diffraction peak suggested that formation of new phases like carbides or borides of W as annealing proceeds.[110] As discussed earlier tungsten carbide and boride phases can be formed at W/B_4C interface even at low processing temperatures. According to JCPDS database [108] the peak position of various possible phases WB, W_2B, W_2B_5, WB_4, WC, and W_2C are very close and are lying within the broad peaks observed for annealed samples. Hence, the GIXRD spectra confirm the possible presence of multiple phases of tungsten carbides and boride. But considering very close peak positions, the particular phase cannot be distinguished.

4.4. Conclusion:

Thermally induced structural changes and its detrimental effect on the normal incidence reflectance of W/B_4C MLs in the vicinity of B K-edge are studied. The main findings of this study is as follows

- W/B_4C is used as optical element in both hard and SXR regime. In this study we extend the application of this combination to EUV regime.
- We observed maximum peak reflectivity of ~8.3% at 68 Å wavelength. W/B_4C ML structure yielded a peak reflectivity of ~7% even after 800 °C annealing. This confirms that W/B_4C combination is good for high heat load applications.
- GIXRD measurements performed using lab source and synchrotron radiation suggested that interface reaction is happening and formation of phases like W-C and/or W-B is

possible. This observation is concluded by appearance of new shoulder near W (110) peak in synchrotron based measurements.

- We observed successive disappearance and reappearance of ML Bragg maxima in XRR. Such behavior suggested that redistribution of atomic density within bilayer, the displacement of interface and the ML period thickness changes as annealing proceeds.
- The formed phases in W/B_4C MLs could not affect the reflectivity performance of ML with B_4C layer thickness more than 20 Å.

Chapter 5.

Structural and compositional analysis of C/B_4C a low-Z/low-Z ML structures and its thermal stability.

In this chapter, we present structural and compositional analysis methodology for a low-Z/low-Z ML combination. C/B_4C combination was examined. Annealing studies were also carried out on this combination. All samples were deposited using ion beam sputtering. Different characterization techniques like hard x-ray reflectivity, resonant soft x-ray reflectivity, transmission electron microscopy, and Raman spectroscopy are used. Results obtained are discussed in this chapter.

5.1. Introduction:

X-ray multilayer (ML) structures are alternating layers of absorber and spacer with periods in the range of few nm.[10,111] Absorption of incident radiation in the ML structure limits the number of layer pairs contributing to reflection of incident beam and hence the resolution. The energy resolution, ($E/\Delta E \sim N$) of the ML mirrors increases with increase in layer pairs, N. In particular high resolution MLs are realized by using the low-Z/low-Z combination. The anomalous dispersion in C and B_4C provide strong optical contrast between these two materials at C and B K edges. The criteria required to achieve high reflectance is to have large difference in dispersion (δ) and low absorption coefficient (β). C/B_4C combination fulfills the criteria required for high reflecting mirror near K absorption edges of C and B. These low electron density contrast (EDC) structures have potential applications as a narrow band pass filter,[112] beam splitter,[113] and to study interaction of high intense radiation with matter. [40,114]

The properties of x-ray ML structures (like Bragg peak width, peak and integrated reflectivity) are strongly influenced by the physical and chemical nature of the interfaces, the composition of the individual layers, and their relative thicknesses.[11] The compositional changes in the buried layers, either due to stoichiometry change or due to presence of impurities, reduce the optical contrast between the materials, which results in significant drop in reflectivity at the application wavelength.[35] It is important to derive the structural parameters like period thickness, relative layers thickness ratio, and interface roughness/width and composition of these nanometer scale length materials, so that the ML preparation techniques can be optimized to yield better performance.

Hard x-ray reflectivity (XRR) is a routinely used non destructive tool to characterize nanometer scale thin films and MLs.[53,115] It provides information about layer densities, thicknesses, and interface roughness/width with sub-nm accuracy. Sensitivity of the conventional XRR depends on EDC between the constituent materials.[116] In the case of MLs containing low-Z/low-Z elements, the electron densities in the two layers are very similar, resulting in limited applicability of XRR to get structural information. It is difficult to get a unique model to fit the XRR data for low-Z/low-Z elements. The structural model obtained from the analysis of the XRR data is generally not able to accurately predict the performance of ML structures in extreme ultraviolet-soft x-ray (EUV-SXR) regime. This is due to fact that the reflectivities at different wavelengths have different sensitivities to the ML parameters.[34]

The XRR measurements are more sensitive to the layer thickness and the interface roughness/width of the ML, and are less sensitive to the compositional changes of the layers.[117] For example, in a Pt/C ML, even a 15% change in the electron density of C layers due to diffusion of Pt atoms into the C layer does not produce significant change in conventional XRR data.[118] Soft x-ray reflectivity measurements performed near the absorption edges are more sensitive to the compositional changes in the layers. Resonant soft x-ray reflectivity measurements were performed to investigate the constituent elements in the low EDC structures.[119,120] Resonant soft x-ray reflectivity (RSXR) has been used to study magnetic multilayers[121,122], polymeric materials[119,123], ionic liquids[124], and compositional analysis of soft x-ray/extreme ultraviolet ML optics.[125]

Multilayers, when exposed to high intense synchrotron radiation, show a quick rise in temperature up to 600 °C [25] and with x-ray free electron lasers (XFELs) the rise in temperature could be even higher. Study of thermal stability of any optical elements is important as it is exposed to high power density synchrotron/XFEL radiation. Many multilayer systems are investigated on this context.[31]

In case of low-Z/low-Z elements, as discussed above, getting precise structural information is difficult. One can use cross-sectional TEM (CXTEM) to get additional structural information and reach a unique solution for XRR data fitting. In the present study, we have used a combination of techniques like XRR, transmission electron microscopy (TEM), and RSXR to derive both structural and compositional information and to test the thermal stability of C/B_4C ML which is a low EDC combination.

5.2.Theoretical background:

In the x-ray region, the response of a medium is described by its energy dependent complex refractive index n (=1- δ + iβ, where δ (dispersion coefficient) and β (absorption coefficient) are the optical constants).[10] The fundamental quantity which tells about the scattering strength and absorption of an atom is the atomic scattering factor (f), which can be written as

$$f = f_{NR}^{o}(q) + f_{R}^{'}(\lambda) - i f_{R}^{''}(\lambda) \qquad \textbf{5.1}$$

where $f_{NR}^{o}(q)$ is the non resonant atomic scattering factor which arises from the free electrons in the atom, $f_{R}^{'}(\lambda)$ and $f_{R}^{''}(\lambda)$ are the resonance and absorption corrections to the atomic scattering factor arising from anomalous dispersion. When electromagnetic radiation is incident on a medium, the electrons in the atom start oscillating. The amplitude of these oscillations has a peak when the frequency of the incident wave is close to the natural frequency of the atom. In a multi element system, the total scattering is the sum of scattering from both resonant and non-resonant atoms. The interaction between the incident radiation and the resonating atoms is stronger as compared to the interaction between the incident radiation and the non-resonant atoms. These interactions cause large change in the refractive index near the absorption edges and causes strong modulation in the reflectivity profile. Hence analysis of a reflectivity profile near absorption edges gives the information of spatial variation of number density of the resonating atoms perpendicular to the material surface. The optical constants of such a multi element layer can be written as[56]

$$\delta = 2.7007\times10^{-4}\lambda^{2}\rho\frac{\sum_{j} X_{j}\left(f^{0}_{NR,j} + f^{'}_{R,j}(\lambda)\right)}{\sum_{j} X_{j}\mu_{j}} \qquad \textbf{5.2}$$

$$\beta = 2.7007\times10^{-4}\lambda^{2}\rho\frac{\sum_{j} X_{j} f^{''}_{R,j}(\lambda)}{\sum_{j} X_{j}\mu_{j}} \qquad \textbf{5.3}$$

Here λ is the incident wavelength [nm], ρ is the density [g/cm^3], X_j is the atomic fraction of j atoms, and μ_j is the atomic weight of j atoms [g/mol].

Conventional XRR performed at higher photon energy is only sensitive to phase shift related to δ. In the resonant region, both the dispersive and the absorption properties of the matter are important and provide orders of magnitude more contrast for materials having a strong resonance effect (particularly in the soft x-ray region) than conventional XRR. Hence, simultaneous analysis of conventional XRR and resonant soft x-ray reflectivity (RSXR), can give the information about the structure and the composition of the buried layers. The knowledge of optical constants is essential to derive the composition of the buried layers. In this work optical constants data base of Henke *et al.*[95], available at CXRO[126] web site for carbon, which works well away from the absorption edge, has been used. The atomic scattering factors for boron, extracted from the measured B_4C films, were used to calculate optical constants of the boron carbide layer with different atomic percent (at.%) of B and C.[127] The tabulated and measured optical constants used in the present study are displayed in Figure 5.1.

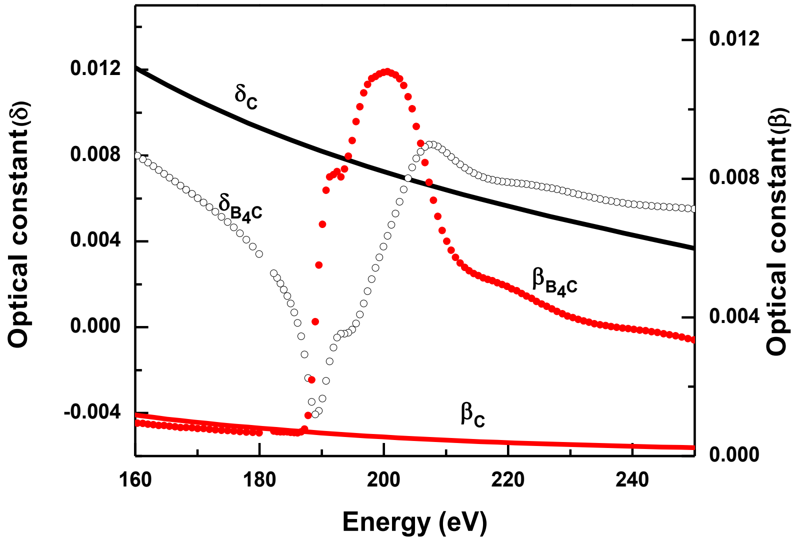

Figure 5.1: Energy dependence of the optical constants (δ and β) for C and B_4C in the vicinity of the boron K-edge of B_4C.

5.3. Experimental:

C/B_4C ML samples were deposited on ultrasonically cleaned Si (100) wafer using ion beam sputtering technique. Commercially available four inch sputtering targets of 99.95% purity for C and 99.9% purity for B_4C was used. Ar ions were used to sputter the target materials. Structural and compositional analysis studies were carried out on two ML samples consisting of 10 layer pairs, with period thickness of approximately 45 Å. These two samples were deposited under identical experimental conditions to confirm the validity of the results. In both the samples, the thicknesses of the layers were kept similar to avoid any compositional changes in the layers with thickness.[118] Annealing studies were carried out on the multilayer with period thickness of approximately 55 Å and consisting of 10 layer pairs.

Hard x-ray reflectivity measurements were carried out using Bruker discover D8 diffractometer at Cu K_α (λ=1.54 Å). The angle dependent soft x-ray reflectance measurements in the vicinity of B K-edge were carried out using the Reflectivity Beamline at Indus-1 synchrotron facility. A nonlinear least square curve fitting technique based on χ^2 minimization method was applied for the determination of structural parameters and optical constants.[54] The transmission electron microscope investigations were carried out on a Philips CM 200 TEM, operated at 200 kV accelerating voltage.

For annealing studies the multilayer sample was placed in a tantalum boat inside the quartz tube. The quartz tube was pumped to a base pressure of $\sim10^{-4}$ Pa. The furnace reached the set temperature within 25 minutes. The sample was heated for 3 hours at respective temperatures and then cooled down to room temperature over several hours. After RSXR and Raman measurements, the same sample was heated again at higher temperatures. The Raman scattering was excited using the Ar laser at 4880 Å and was analysed using a Jobin Yvon micro-Raman spectrometer (HR800) over the range 250-2000 cm^{-1}.

5.4.Results and discussions:

5.4.1. Structure and compositional studies

XRR reflectivity curves obtained from measurement at Cu K_α wavelength (λ=1.54 Å), along with theoretically calculated profile as a function of scattering vector (q_z), are shown in Figure 5.2. Bragg peaks only up to second order are observed. The q range in XRR is limited by the low EDC between the layers. The low EDC between C and B_4C layers causes weak reflection at boundary between these layers. The small oscillations are due to the total thickness of the ML stack. Structural parameters of the ML structure have been derived by fitting the experimental reflectivity data with two layer model consisting of C and B_4C.

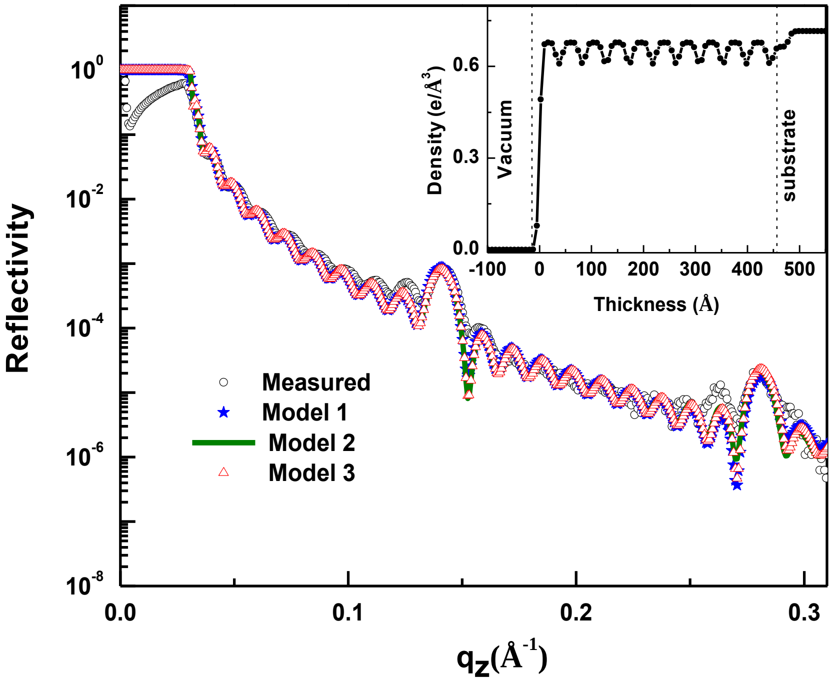

Figure 5.2: Measured and simulated XRR profiles of the C/B_4C ML structure. The inset shows the electron density profile obtained from the model-3.

The difference between the experimentally measured and the calculated reflectivity is minimized by varying the layer thickness (d), densities (ρ)/optical constants, and roughness/width for the C-on-B_4C (σ_1), and the B_4C-on-C (σ_2) interfaces. During the fitting of the XRR data, different structural models may yield similar curves. The structural parameters obtained from different structural models are presented in Table 5.1. As can be seen from Table 5.1 we have simulated reflectivity pattern with two different structural Models 1 and 2 having different thickness of C and B_4C layer but same reflectivity pattern. During fitting, the layer thickness ratio is slightly compensated by changing the interface parameter. This is due to the fact that reflection coefficient between two materials having low EDC is small and causes weak modulation in the Bragg peak intensity. Changing the layer thickness ratio causes negligible change in the average density of the ML structure made up of low EDC combination, and hence negligible change in critical angle. The layer thickness ratio and the interface parameters have similar effects on the reflectivity profile in low EDC systems. This makes it difficult to decide which structural model is correct. From this simulation one is sure of only the total thickness and average stack density. One needs some other complementary technique to solve the structural details completely.

Table 5.1: Structural parameters obtained from different structural models as shown in Figure 5.2.

Structural model	$\mathbf{d_C}$ (Å)	$\boldsymbol{\sigma_1}$ (Å)	$\mathbf{d_{B_4C}}$ (Å)	$\boldsymbol{\sigma_2}$(Å)
Model 1(XRR only)	16.5	4.0	28.5	2.5
Model 2(XRR only)	12.5	4.0	32.5	7.0
Model 3(XRR+TEM)	14.0	4.0	31.0	4.0

The transmission electron microscopy provides information about the layer thicknesses, interface structure, and the diffusion at the interface. Therefore, it is helpful to have a complementary technique like TEM, which acquires the real space information directly to confirm the layer model. A cross-sectional TEM (CXTEM) image of C/B_4C ML is shown in Figure 5.3(a). The bright and thin layer represents the C layer, which has a low density that allows more electrons to transmit and appears to be bright. The darker and thicker region represents the B_4C layer. A layer profile extracted from the TEM image is also shown in Figure 5.3(b). It can be seen that there is a sharp transition between C and B_4C layers. The sharp transition in the line profile is used to determine ML period thickness as well as the individual layer thicknesses. The cross-sectional

TEM image in Figure 5.3(a) suggests that C and B_4C interfaces are not smooth. The interfaces of C on B_4C and B_4C on C are symmetric. This is consistent with the earlier studies on a similar combination.[98] As a result of CXTEM investigation, we got the layer thickness ratio and also that symmetric interface model should be used for fitting XRR data.

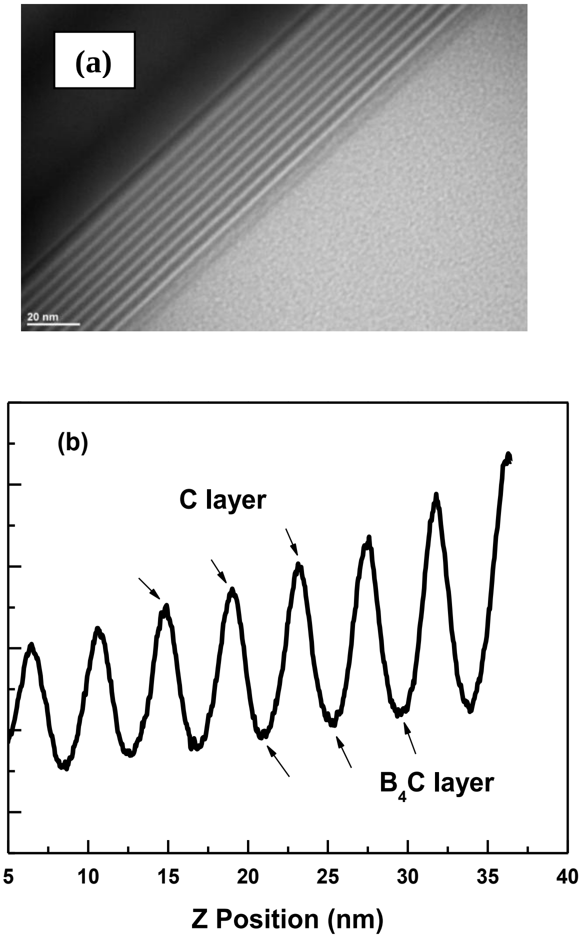

Figure 5.3: a) Cross-sectional TEM image of the C/B_4C multilayer structure, b) A plot showing a layer profile obtained from the TEM image.

Using the information obtained from CXTEM, the XRR data was revisited. The geometrical parameters obtained from in the best fitted model (i.e Model-3), as shown in Figure 5.2, were d_C = 14 Å, d_{B_4C} = 31 Å, and 4.0 Å interface roughness/width for both the interfaces. The ML period thickness was d = 45 Å. The optical constants are $\delta_C = 6.41\text{x}10^{-5}$, $\beta_C = 1.15\text{x}10^{-8}$, δ_{B_4C} = $7.21\text{x}10^{-6}$ and β_{B_4C} = $7.95\text{x}10^{-9}$. The electron density profile obtained from the best fitted model is also shown in the inset of Figure 5.2. The EDC between C and B_4C interface, $(\rho_{B_4C} - \rho_C)/\rho_{B_4C}$ was 11%. This value is larger than the EDC (~7%) calculated from the tabulated values from Henke *et al.*[95,126] This is due to the fact that the density of a film is different from the bulk value of the material used to make the film. The structural parameters of ML stack are known. To derive the compositional information of SXR near the absorption edges were performed and structural parameter derived from XRR and CXTEM are used while analyzing the SXR data.

RSXR measurements near the boron K-edge of B_4C were performed to derive the composition of these low EDC structures. RSXR utilizes the variation in energy dependent atomic scattering factors, which undergo strong variation near the absorption edges. Figure5.4 shows the sensitivity of RSXR to the compositional changes in B_4C layer, through simulation on the ML structure. The optical constants shown in Figure5.1 were used in simulating the RSXR profile. A change in the atomic percentage of B and C in the boron carbide layer causes significant modulations in the reflectivity profile. The peak reflectivity increases with increase in the at.% of B into the B_4C layer. This is due to the fact that as boron atoms are the resonating atoms, increase in its atomic percent enhances the optical contrast between C and B_4C layer. Similarly, the peak reflectivity decreases with decrease in the atomic percent of B of B_4C layer. The sensitivity of the simulated RSXR profile to the variation of at.% is sufficient to experimentally probe the changes in the atomic compositions of the grown films.

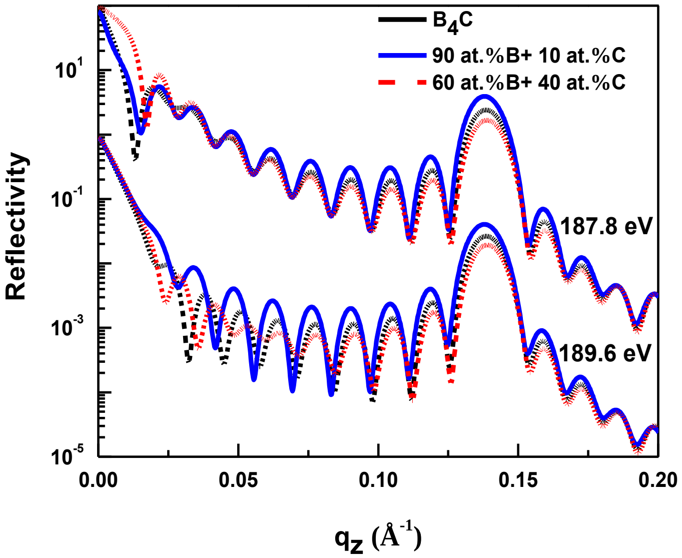

Figure 5.4: Simulated RSXR profile of C (14 Å) / B$_4$C (31 Å) for an ideal ML consisting of 10 layer pairs, at two different energies in the vicinity of the boron K-edge, for varying atomic percentages of B and C of the boron carbide layer .

The experimental RSXR data of C/B$_4$C ML and the simulated reflectivity curves as a function of scattering vector for different photon energies near the boron K-edge are shown in Figure 5.5. From Figure 5.5, in the low q_z range of data, the critical angle appears only at 185. 6 eV and disappears for other energies. The Bragg peak at two different energies 186.7 eV and 185.6 eV is also shown in the inset of Figure 5.5. The peak reflectivity decreases when one moves away from the boron K- absorption edge (~189 eV). This is due to the fact that away from the boron K-absorption edge, the optical contrast between C and B$_4$C decreases, which results in a drop in the peak reflectivity. The free parameters in simulating RSXR profile are : individual layer thickness, interface roughness/width, and optical constants. To reduce the number of free parameters in simulating RSXR profile, structural parameters obtained from XRR and optical constants displayed in Figure 5.1 were used. The difference between the simulated and the experimentally measured RSXR was minimized by changing the

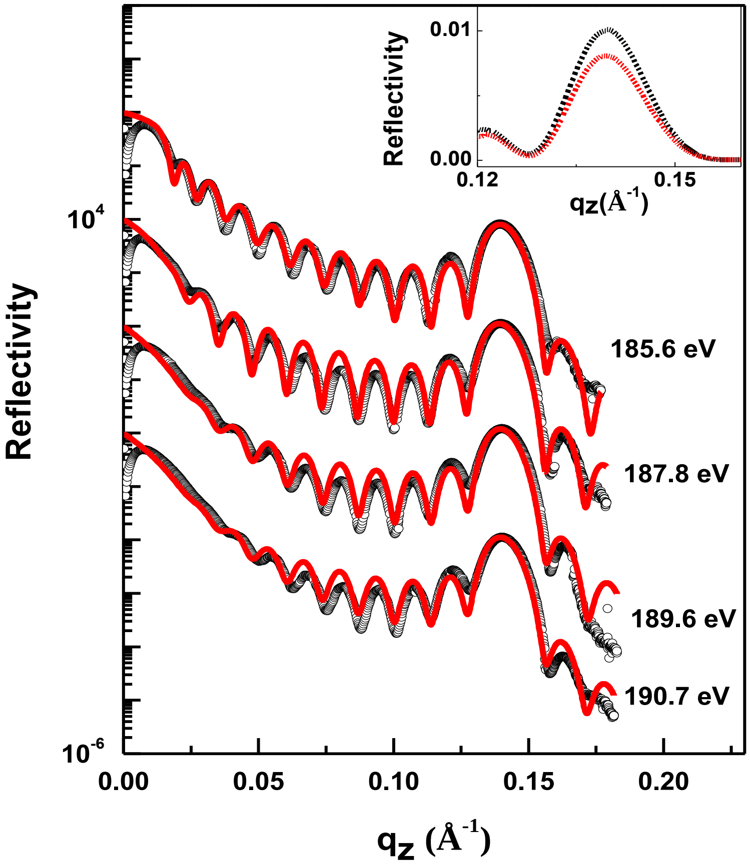

Figure 5.5: The measured RSXR profiles of the C/B_4C ML, along with the simulated profiles, at four different photon energies near the boron K-edge. The inset shows the variation of the Bragg peak intensity when moving away from the absorption edge, at two different energies: 186.7 eV (black curve) and 185.6 eV (red curve).

optical constants of each layer. Generally, a thin capping layer at the surface of ML structure, which is due to ML sample exposed to air, and a native oxide layer on top of Si substrate, is included in fitting the RSXR data. Optical constants of both C and B_4C layers obtained from the best fit of RSXR curves are given in Table 5.2. The optical constants of C are in agreement with values reported by the Henke *et al.*[95,126], given in Table5.2 within square brackets, whereas optical constants of B_4C differ significantly from those in square brackets. These discrepancies in optical constants near the absorption edges may be due to high sensitivity to error in energy calibration or resolution, and compositional changes in buried B_4C layer due to stoichiometry changes or due to presence of impurity.

Table 5.2: Presents the optical constants of C and B_4C derived from the fitting of RSXR data. The square brackets show the Henke et al. data[95,126] for C and R. Soufli et al.[127] data for B_4C.

Energy (eV)	δ_C	β_C	δ_{B_4C}	β_{B_4C}
190.7	0.0074 [0.00814]	0.000607 [0.00065]	-0.00114 [-0.00250]	0.00753 [0.00766]
189.6	0.00783 [0.00824]	0.000615 [0.00067]	-0.00136 [-0.00390]	0.00674 [0.005507]
187.8	0.00797 [0.00843]	0.000707 [0.00069]	-0.00139 [-0.00237]	0.00381 [0.00117]
186.7	0.00835 [0.00855]	0.000715 [0.000711]	-0.000210 [-0.00043]	0.00144 [0.000693]
185.6	0.00845 [0.00888]	0.000724 [0.00072]	0.000852 [0.000690]	0.00078 [0.000667]

Near the absorption edge, the optical constants undergo sharp variation with energy. From Figure 5.1, it is clear that the absorption coefficient (β) has abrupt variation in the energy range 198 to 187 eV. For example, β changes (~ 8%) from 0.005507 (189.6eV) to 0.003871 (189 eV). From Table 5. 2, it is clear that β has slightly higher value than the reported values. This may be due to error in energy calibration or resolution of the beamline. However the dispersion coefficient δ deviates significantly (more than ~200%) from the values reported in literature. This cannot be simply explained based on the energy resolution. It indicates that composition /stoichiometry of the layer is different from that of bulk B_4C.

It is reported that sputtered boron carbide thin films can have carbon composition varying from 10 atomic percent (boron rich) to 40 atomic percent (carbon rich).[128] Different compositions of the boron carbide layer can be understood from its structure. Boron carbide has a complex structure. Crystalline boron carbide with B_4C stoichiometry consists of twelve atom icosahedral units at the vertices of the rombhohedral unit cell and C-B-C chains on its main diagonal coinciding with crystallographic c-axis. As the carbon content increases, the C-B-C chains are replaced with C-C-C chains.[128] In the case of amorphous boron carbide, it is believed that the structure is still based on a random icosahedral network at a carbon content less than 50 at.%. The presence of different at.% of C or B atoms into the boron carbide layer causes a significant change in optical constants near the absorption edge, which limits the optimal reflectivity achieved from the boron carbide based MLs. For example, when the composition of boron carbide with B_4C stoichiometry changes to 90 at.% B and 10 at.% C, δ changes from -0.00237 to -0.00556 and β changes from 0.00117 to 0.00115 at 187.8 eV energy, and δ changes from -0.00393 to -0.0075 and β changes from 0.00507 to 0.0061 at 189.6 eV energy. Similarly, when the composition of boron carbide layer changes to 60 at.% B and 40 at.% C, δ changes to -0.00049 and β changes to 0.00096 at 187.8 eV energy, and δ changes to -0.00018 and β changes to 0.0041 at 189.6 eV energy. The deviation in the experimentally derived optical constants of our boron carbide films from the reported values suggests the presence of excess C in it. Presence of excess C in the born carbide layer is either due to inter-diffusion of C atoms from the C layer or due to change in stoichiometry of boron carbide layers from the target (B_4C) during deposition.

To confirm the validity of results obtained from the present ML sample, RSXR measurements were performed on another sample of similar thickness, deposited under identical experimental conditions. The RSXR curves of two samples measured near the B K-edge are shown in Figure 5. 6. The measured RSXR of these two samples are similar, so that the results obtained from one sample are applicable to the other sample also. The knowledge of both structural and composition of buried layers deposited under certain experimental conditions is essential to predict maximum achievable reflectivity from the structure.

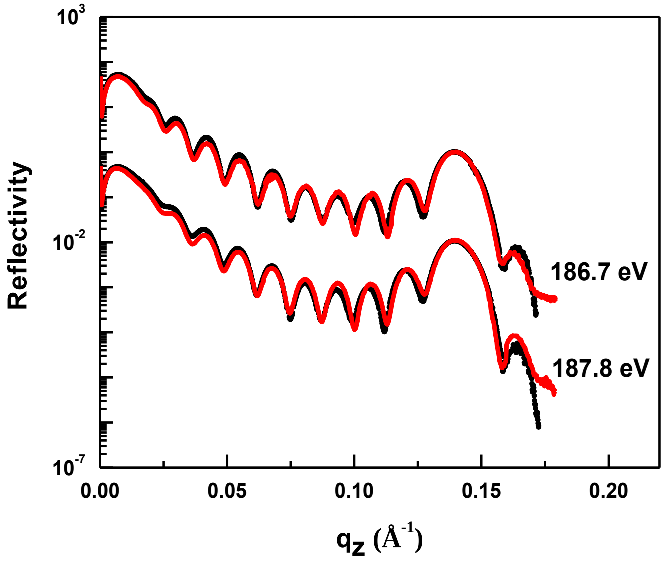

Figure 5.6: Resonant soft x-ray reflectivity curves of two samples deposited under similar experimental conditions, at two different energies.

5.4.2. Annealing studies

Annealing studies also carried out on this combination. RSXR measurements performed on annealed ML in the vicinity of B K-edge are shown in Figure 5.7. The Bragg peak shifted to lower angle after annealing at temperatures up to 600 °C, indicating increase in multilayer period. After 700 °C annealing, Bragg peak shifted to higher angle, indicating a decrease in multilayer period. The broadening in Bragg peak and reduction in SXRR after 800 °C annealing suggested that the structural modification like inter diffusion or increase in interface roughness

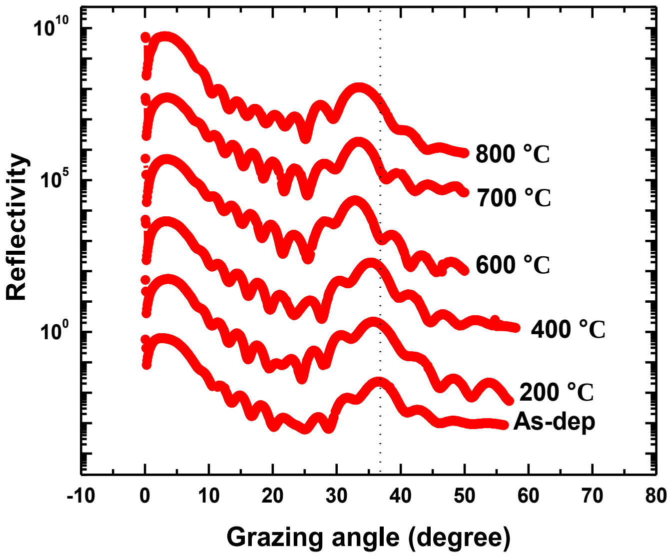

Figure 5.7: Angle dependent RSXR curves of C/B$_4$C ML sample at various annealing temperatures in the vicinity of B K-edge (65.6 Å).

takes place. The measure peak reflectance is decreases after 700 °C annealing suggest that the ML structure is stable up to 700 °C. However the presence of well defined Kiessig oscillations and Bragg peak suggested that the overall structure of multilayer is preserved even after 800 °C annealing. Raman Spectroscopy measurements were performed to investigate the period thickness changes in C/B$_4$C MLs on annealing. It is known that Raman spectra is sensitive to changes in translation symmetry and are thus useful for the study of disorder and crystallite formation in thin carbon films and it is expected that it will provide information about the C/B_4C layer structure. Figure 5.8 shows the Raman spectrum of the as prepared sample and the strong line at 521 cm^{-1} represents the first order Raman line of Si substrate and the broad feature over 900-1050 cm^{-1} represents the second order Si spectrum. The strong Raman feature of Si substrate shows that C/B_4C multilayer sample is transparent to the incident laser wavelength. The other broad feature over 1000-2000 cm^{-1} is characteristic of Raman spectrum of disordered carbon films.

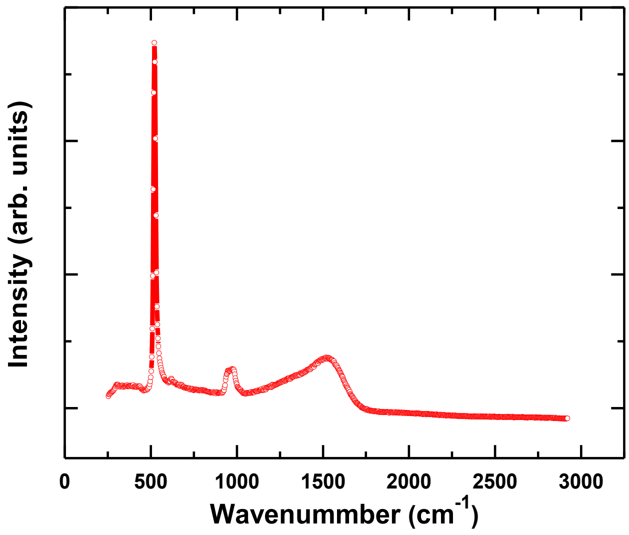

Figure 5.8: Raman spectra of the as-deposited C/B_4C sample.

The spectra were recorded at each stage of the annealing and Figure 5.9 shows the background subtracted spectra over 1100-1800 cm^{-1} for as-deposited and annealed sample at 200 °C, 400 °C, 600 °C, and 800 °C respectively. The spectra without annealing can be convoluted with two Gaussians, one at 1386 and the other at 1547 cm^{-1} which can be assigned to the D and G peak respectively. In general *a*-C film can have any mixture of sp^3, sp^2 and even sp^1 sites. The extreme composition consisting of single crystalline graphite (sp^2) has a mode at 1581 cm^{-1} and that for diamond (sp^3) at 1332 cm^{-1}. For carbon film the G mode involves in-plane bond stretching motion of pairs of C sp^2 atoms and varies over 1500 to 1630 cm^{-1}. The D peak around 1355 cm^{-1} is the hexagonal carbon ring breathing mode of A_{1g} symmetry involving phonons near the K point of the zone boundary and this is inactive in crystalline graphite and only becomes active in presence of disorder. Its intensity is strictly connected with the presence of six fold aromatic ring and inversely proportional to the cluster diameter. The important feature of the Raman spectrum of small graphite crystallites is that the appearance of an additional disorder, or D line and changes occur in the region of the G line.

Figure 5.9 shows the change in Raman spectra as a function of annealing temperature. The Raman spectra shown in Figure 5.9 are similar to those observed by Wada et al.[129] and Dillon et al.[130] for sputtered annealed carbon films.

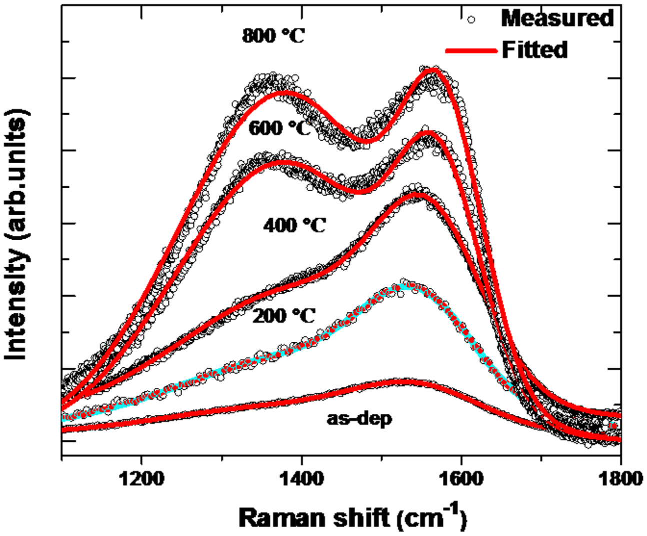

Figure 5.9: Raman spectra of the C/B_4C at different annealing temperatures. The solid is a fit to data points using two Gaussian peaks.

All the line profiles have been analyzed into D and G bands which are shown in Figure 5.9 along with the variation in their peak position shown in Figure 5.10a. The position of G-peak shifts upwards to higher frequencies, indicative of a reduction of the number of sp^3 coordinated carbon atoms. The full width half maximum of peaks (FWHM) is shown in Figure 5.10b. The FWHM of the peaks G and D is sensitive to bond-angle disorder and the crystallite formation. We observed decrease in FWHM of the peaks D and G as annealing temperature is increased. The large FWHM in the as-deposited films is because of the bond-angle disorder. The FWHM of the peaks decreases as the disorder is removed by annealing and as crystallites become more dominant. Figure 5.10c shows I(D)/I(G) ratio as a function of annealing temperature. The I(D)/I(G) ratio increases with annealing temperature.

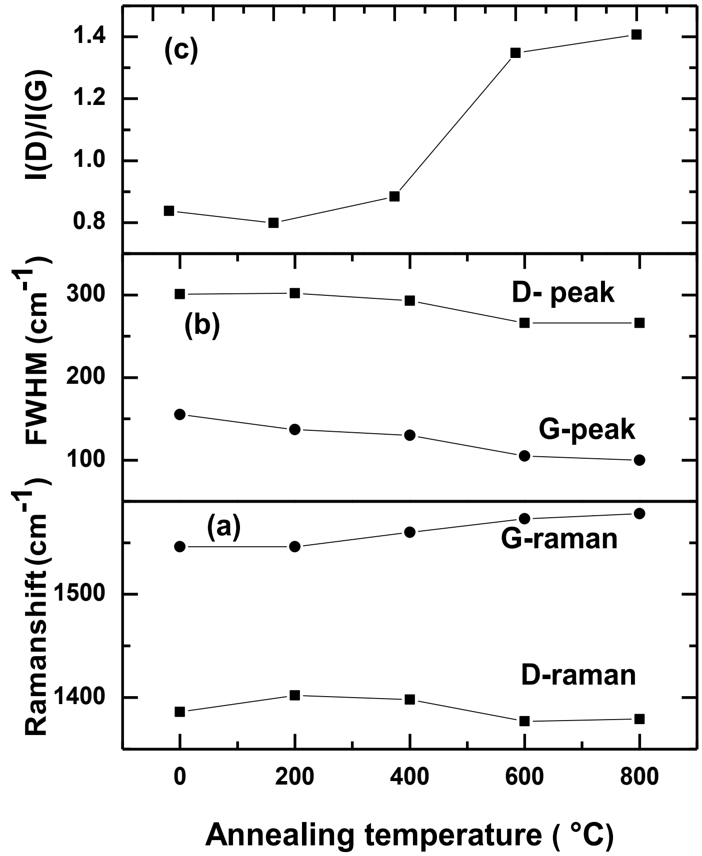

Figure 5.10: Variation of Gaussian fitted Raman parameters (a) peak position, (b) full width half maximum (FWHM), (c) intensity ratio I(D)/I(G) with annealing temperature.

As the annealing temperature is increased the crystallites grow in size and/ or number and thus contribute to Raman spectrum causing the I(D)/I(G) ratio to increase. It can be seen that the G band frequency increases from 1546 to 1578 cm^{-1} and the I(D)/I(G) increases from 0.83 to 1.5. Both the peak position of G band and the I(D)/I(G) ratio are very important parameters to characterize the bonding pattern of carbon atoms. The sp^3 fractions are calculated using three-stage model described by Ferrari et al.[131] to explain the visible Raman spectra of amorphous carbon. It can be seen that the value of 1546 $cm\text{-}^{1}$ for the G band and 0.83 for I(D)/I(G) suggest a sp^3 fraction of about 10-12% implying that the *a*-C layer is predominantly graphitic with presence of significant fraction of nanocrystalline clusters. As the annealing temperature increases, the G band value increases with corresponding increase in I(D)/I(G) implying decrease in sp^3. The decrease in sp^3 fraction to 5% decreases the transparency of the layer which is evident from the decreasing signal to noise ratio of the Raman signal. Further it is known that the density of graphite is lower than that for diamond and this implies that reduction in sp^3 fraction results in decrease in density which will lead to increase in layer thickness.

5.5.Conclusions:

In this chapter we studied structural and compositional analysis of C/B_4C, a low-Z/low-Z ML structures and its thermal stability. The main findings of this study is as follows

- XRR provide limited structural information when electron density difference between layers is small
- Combining XRR with TEM provided improved structural information.
- Compositional information of B_4C layer was estimated using structural information obtained from XRR and TEM with RSXR.
- The derived optical constants of boron carbide from SXR measurements suggested presence of excess C into the boron carbide layer
- This change in composition of B_4C has reduced the reflectivity of the ML near B K-edge.
- The method present in this chapter can be applied to any low EDC combination
- C/B_4C ML structure is stable up to 700 °C. Graphitization of C layer with annealing temperature causes period thickness expansion in C/B_4C MLs.

Chapter 6.

Investigation of composition of boron carbide thin films

In this chapter, we investigate the change in composition of boron carbide thin films with thickness. Boron carbide thin films were deposited using ion beam sputtering. We used different characterization techniques like hard x-ray reflectivity, resonant soft x-ray reflectivity, x-ray photo electron spectroscopy, resonance Rutherford backscattering spectrometry and time of flight secondary ion mass spectrometry. Results obtained are discussed in this chapter.

6.1. Introduction:

Boron carbide is an important x-ray optical element in both hard and soft x-ray regions.[10,36,56,132] It is also an important barrier material to minimize the inter diffusion in multilayers (MLs).[42] Boron carbide which has a very high melting and sublimation point is one of the suitable candidates for free electron laser applications.[39-41] It is used as capping layer on top of the ML structure to protect ML structure from oxidation.[133] Boron carbide is also a promising material for the next generation photo lithography applications at 6.x nm (the value of x still has to be determined by industry) wavelength.[37,38] The compositional changes in the boron carbide causes significant changes in its optical constants in the vicinity of B K-edge and limits maximum achievable throughput from boron carbide based MLs.[134] The optical band gap of boron carbide and the properties of boron carbide/Si diodes can be varied by simply changing composition of boron carbide.[135-137] In many practical applications boron carbide thin films with thickness ranging from a fraction of a nanometer to several nanometers have been used. It is thus important to study the thickness dependent compositional changes in boron carbide thin films.

In the last chapter on C/B_4C MLs, we observed deviation in derived optical constants of boron carbide from the values available in literature.[127] A detailed analysis, suggested that the boron deficient/carbon rich growth in boron carbide layer is happeining. In that analysis we concluded that presence of excess carbon in the boron carbide layer is either due to inter-diffusion of C atoms from the C layer or due to change in stoichiometry of deposited boron carbide layer from the target (B_4C) stoichiometry. To investigate further the compositional changes in boron carbide we have chosen thin films of boron carbide in this study. This should confirm if composition of B_4C layer has changed during deposition itself.

In general ion and electron beam techniques are used to determine concentration profiles of films .[52] Electron beam techniques for examples X-ray photo electron spectroscopy and Auger electron spectroscopy have been used in multi component thin films, solid samples to determine the concentration profile from the surface with a depth resolution of ~ 10 Å. In-depth information is obtained by etching the material under study. Ion beam techniques like Rutherford backscattering spectrometry (RBS) and secondary ion mass spectrometry (SIMS) have also been used the concentration profiles. Rutherford scattering cross-section is small for lighter elements and decreases with decrease in the thickness of sample understudy. The typical depth resolution is ~ 100 Å. Ion beam technique like SIMS has excellent depth resolution (~ 10 Å) and in-depth information is obtained by etching out the material. It provides the qualitative information for quantification we need standard samples. Destructive nature of characterization technique prohibits the successive measurements on one sample. X-ray standing wave technique in combination with XRR was used to study composition of periodic layer structures with depth resolution down to 1 Å for Pt/C ML. However X-ray fluorescence signal for low-Z elements is weak.[118]

In the vicinity of the absorption edges optical index is strongly depends on the composition of layers as discussed in last chapter. The reflectivity measured in the vicinity of absorption edges has opened up possibility to derive composition of thin films in non destructive way. The angular dependence inherent to reflectivity measurements provides the depth resolution down to nm with penetration depths over tens of nanometers. Resonant soft x-ray reflectivity (RSXR) has been used for characterization in low contrast organic thin films[119] and compositional analysis in thin film[138] and periodic multilayers.[134]

In this chapter we investigate the compositional changes in boron carbide thin films as a function of its thickness by combining XRR and RSXR. X-ray photo electron spectroscopy (XPS), resonance Rutherford backscattering spectrometry (RRBS) and time of flight secondary ion mass spectrometry (TOF-SIMS) measurements were performed to complement the observation made from RSXR.

6.2. Experimental techniques:

6.2.1. Sample preparation:

Boron carbide thin films of various thicknesses were deposited on ultrasonically cleaned Si (100) wafer using ion beam sputtering technique. We used commercially available four inch sputtering target of 99.5% purity for B_4C. The base pressure of the system was ~ 3×10^{-5} Pa. During the deposition the Ar gas flow was fixed at 3 standard cubic centimeters which results in a vacuum drop to 6×10^{-2} Pa in the chamber. Ar ion-beam of current about 25 mA and voltage 1000 V was used to sputter the target material. Target material was pre sputtered for 30 min before the deposition of films. In the present study boron carbide thin films of thickness (d) ranging from 100 to 900 Å were used.

6.2.2 Reflectivity measurements:

XRR measurements were carried using Bruker discover D8 diffractometer at Cu K_α radiation (λ=1.54 Å). The angle dependent soft x-ray reflectance measurements in the vicinity of B K-edge were carried out using the reflectivity beamline at Indus-1 synchrotron facility. A nonlinear least square curve fitting technique based on χ^2 minimization method was applied for the determination of structural parameters and optical constants from reflectivity curves.[56] Optical index profile obtained from RSXR measurements were used to derive the composition of films. In order to take into account the effects of bonding between B and C in B_4C on the ASFs, we used ASFs for B derived from magnetron sputter deposited boron carbide thin films.[127] ASFs for non-resonating atoms like C and O were taken from the Henke *et al*. [95] tabulated values. The mass density obtained from XRR measurements were used and best fits to the derived optical constants was obtained by varying the atomic fraction of different chemical elements in the film.

6.2.3 XPS measurements:

XPS measurements were carried out using photoelectron spectrometer at a base pressure better than $5x10^{-10}$ mbar. Al K_α radiation (λ=83.4 Å) was employed for recording the spectra with the source operated at an emission current of ~10 mA and an anode voltage of ~ 10 kV. XPS spectra were taken on the samples after sputter cleaning sample surface with Ar ions. Sputter cleaning of sample surface was achieved by the bombardment of 1 keV Ar ions for 5min.

6.2.4 RRBS measurements:

In general Rutherford backscattering spectrometry (RBS) is used for analysis of heavier elements on lighter substrate. However RBS is ineffective for detection of lighter elements on heavier substrate due to small scattering cross-section and overlap of background signal coming from heavier substrate. RRBS has been widely used for analysis of light elements on heavier substrate. The RRBS measurements were performed using 3.045 MeV He^{++} particles for the quantification of oxygen, 3.9 MeV He^{++} particles for the quantification of boron and 4.27 MeV He^{++} particles for the quantification of carbon as alpha particles has enhanced scattering cross-section with these elements at these energies. The 1.7 MV Tandetron accelerator (HVEE, The Netherlands) available at IGCAR, Kalpakkam was used for the RRBS analysis. The backscattered particles were detected using a Si surface barrier detector kept at an angle of 165° with respect to the incident beam direction. The concentrations of oxygen, boron and carbon in the samples were obtained from the best-fit of RRBS data using the SIMNRA program.[139]

6.2.5 TOF-SIMS measurements:

TOF-SIMS depth profile analysis of B_4C thin films were carried out in interlaced mode with pulsed Bi_1+ at 30 keV (~5pA) as the analysis gun and 1keV Cs+ as the sputter gun operating at a constant current of ~75nA. The area of analysis across all measurements was 100µm x 100µm inside the sputter area of 300µm x 300µm. The sputter gun parameters were selected to ensure that erosion is slow enough to reveal the variation in 100 Å thin B_4C sample which was again used to profile the thicker deposited B_4C.

6.3. Results and discussion:

6.3.1. XRR measurements:

Reflectivity curves obtained from the XRR measurements at Cu K_α radiation (λ=1.54 Å), along with the theoretically calculated curves as a function of scattering vector (q_z) are shown in Figure 6.1. The thicknesses of films are indicated on the plot. The oscillations are due to interference between the rays reflected from different interfaces in the sample and the damping of these oscillations depends on the surface roughness of the sample. From Figure 6.1, it is clear that the different samples have different q_z range. This indicates that the root mean square (rms) surface roughness of the grown film changes significantly with thickness and deviates from the substrate rms roughness.

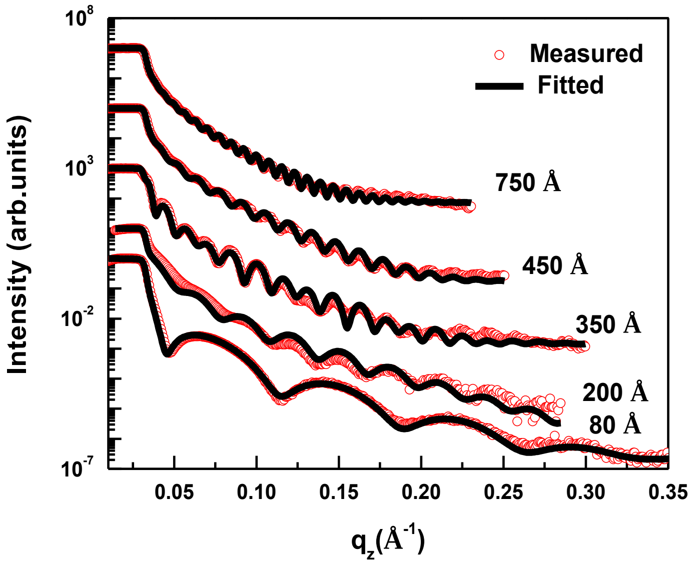

Figure 6.1: Measured and simulated XRR curves of boron carbide thin films. Deposited film thicknesses are also indicated in the graph

We assumed two layer model consisting of boron carbide/SiO_2/Si to simulate the measured XRR curves. In general, an oxide layer is formed on top of Si substrate due to exposes to ambient. The difference between measured and calculated reflectivity curves is minimized by changing thickness, density and roughness of the assumed layers. The coated film with uniform density gives a satisfactory fit for all the samples except for the sample of thickness 350 Å. In fact, this coated layer needs to be divided in two parts of different densities to obtain a best fit. Therefore, we use a tri-layer model consisting of boron carbide layer-2/boron carbide layer-1/SiO_2/Si. The best fitted model suggested that the density of layer-1 is less than the layer-2. Thickness, density and roughness of deposited films obtained from the best fitted model shown in Figure 6.1 are presented in Table 6.1.

Table 6.1: Thickness, density and roughness of deposited films obtained from the best fitted models shown in Figure 6.1.

Deposited film thickness (Å)	Estimated thickness (Å)	Density (g/cc)	Roughness (Å)
80	83.5±0.5	1.76±0.07	6.0
200	187±1	2.50±0.04	6.5
350	293±2	2.46±0.07	9.0
	72±2	2.08±0.07	7.0
450	408±2	2.50±0.04	10.0
750	768±3	2.50±0.04	12.0

From Table 6.1, it is clear that the rms roughness of the films increases with increasing the thickness. The density of the low thickness film deviates significantly from the bulk value (~2.52 g/cc). The geometrical parameters of deposited films were known. Using XRR we cannot distinguish between B and C atoms because of low electron density difference (~2%). The compositional profile of film consisting of low electron density contrast elements cannot be determined using XRR. The compositional profile of deposited layers can be determined by simulating the measured soft x-ray reflectivity curves in the vicinity of the B K-edge. The geometrical parameters like thickness and rms roughness obtained from analysis of XRR curves were used as input parameters while analysis of RSXR data.

6.3.2. RSXR measurements:

In the vicinity of the absorption edge both the optical constants δ and β underwent strong variation. RSXR utilizes the optical contrast due to both δ and β and shows strong modulation in reflectivity profile as the energy of incident radiation changes. Depth profile of the chemical elements composing the film is reconstructed based on analysis of reflectivity curve measured in the vicinity of the absorption edge. The factors which influence the determination of optical constants and hence a reconstructed composition profile of film using soft x-ray reflectivity are (i) A contaminated layer (CLR) present on top of the sample surface (ii) geometrical parameters like thickness and roughness.[140-142] CLR on the sample surface is mainly consisting of hydrocarbons, water, and oxygen. A CLR of thickness 20-30 Å is assumed to simulate measured RSXR curves. The geometrical parameters obtained from the XRR are used as input parameters while analyzing the RSXR data and best fit is obtained by changing the optical constants of the deposited films. This method improves the reliability of reconstructed composition profile of film.

RSXR measurements were performed in the energy ranging from 184 to 197 eV. The measured and simulated RSXR curves of the samples 410 Å and 365 Å are shown in Figure 6.2(a) and (b) respectively at selected energies in the vicinity of B K-edge. From Figure 6.2, it is clear that reflected intensities are entirely different for different energies. In the vicinity of the absorption edge optical constants changes significantly as energy changes and that can gives a clear change in a reflectivity pattern. From Figure 6.2b, it is clear that a shoulder in the reflectivity profile appears at 184.5 eV and disappears for other energies. At lower energies away from the B K-edge of B_4C (~189.6 eV) β decreases and δ become positive results in appearance of shoulder in the reflectivity curve.

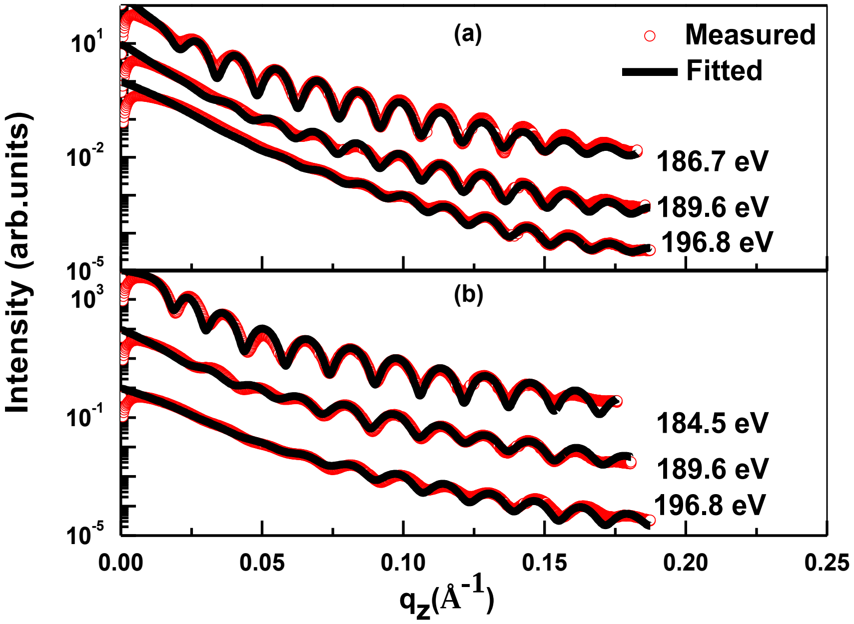

Figure 6.2: Showing the measured and simulated RSXR curves of the sample of thickness (a) 410 Å and (b) 365 Å in the vicinity of B K-edge.

Figure 6.3(a) and (b) shows the measured and simulated RSXR curves of the samples 187 Å and 83.5 Å respectively at selected energies in the vicinity of B K-edge. From Figure 6.3b, it is clear that a shoulder in lower q_z appears and reflected intensities are similar for all energies. An appearance of the shoulder in lower q_z and flat response of the reflectivity profile suggests that no or little amount of B atoms present in the deposited layer. The simulated curves are obtained by varying optical constants of each constituent layers. A satisfactory fit is obtained without CLR in the case of sample 83.5 Å. This might be due to similar optical behavior of both CLR and deposited film.

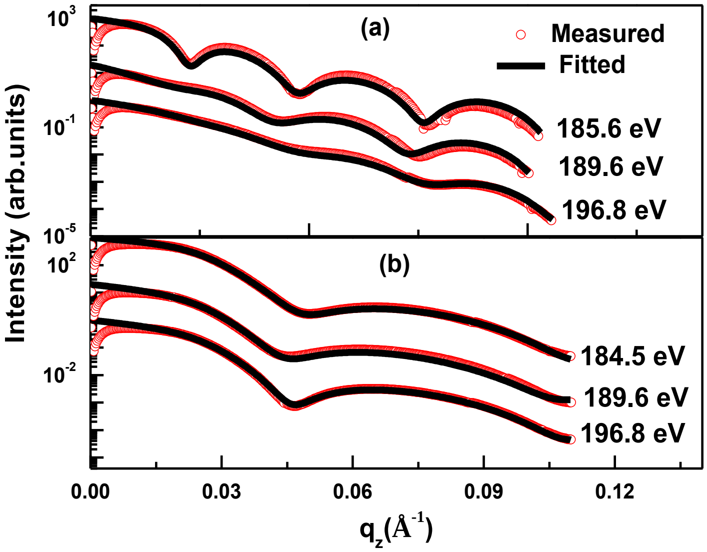

Figure 6.3: Showing the measured and simulated RSXR curves of the sample of thickness (a) 187 Å and (b) 83.5 Å in the vicinity of B K-edge.

Figure 6.4 (a) shows the optical index profile as a function of depth of all samples obtained from the best fitted model shown in Figures 6.2 and 6.3 at energy of 189.6 eV. The optical index profile suggested film is uniform across the depth except in the 365 Å thickness sample. A gradual change in optical index profile is observed in the 365 Å thickness sample. This gradient in optical index profile is not seen in other samples. The optical index profile of layer-2 is used to compare the compositional changes in films with thickness. The value of optical index increases with decreasing the film thickness. At this energy B is a resonating atom C and O are non resonating atom. Polarizability of the resonating atom is out of phase with the electric field which results in real part of ASF or δ become negative. Polarizability of non-resonating atoms is in phase with electric field which results in real part of ASF or δ become positive. The increase in the value of optical index suggested that the decrease in the B atomic content in the film with decrease in the film thickness.

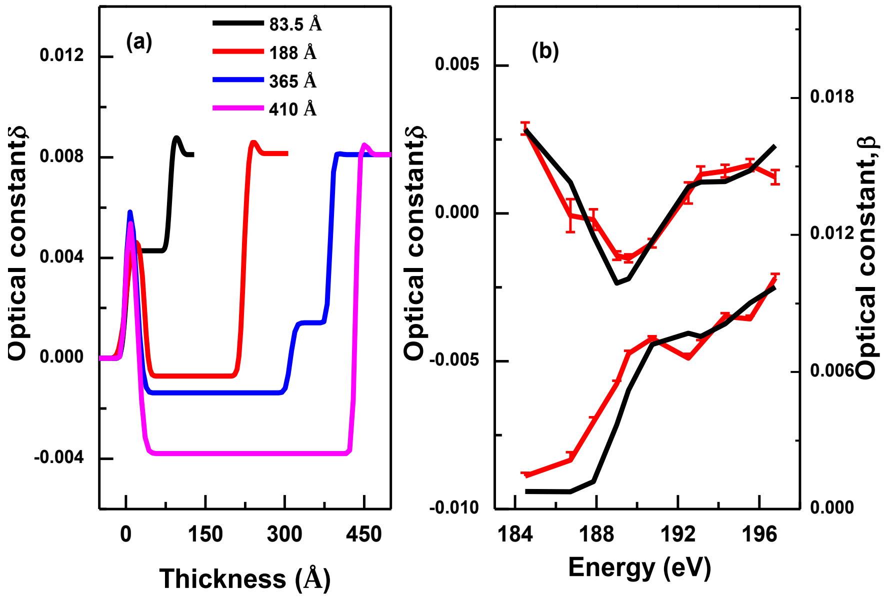

Figure 6.4: (a) Showing the optical constant, δ profile obtained from the fitting of RSXR data at energy of 189.6 eV. (b) Showing the (color line) Optical constant profile of layer-2 of the sample of thickness 365 Å as a function of photon energy in the vicinity of B K-edge (black line) model composition consisting of different at.% B, C and O.

The composition of the films was estimated using the optical index profile derived over extended region in the vicinity of the B K-edge. In case of 410 Å thickness sample, the derived optical constants are in close agreement with the values reported by R. Sofuli *et al.*,[127] measured on the magnetron sputtered boron carbide thin films of composition 74 at.% B, 20 at.% C and 6 at.% O. The derived optical constants of the sample of thickness 770 Å are also similar to the 410 Å thickness sample. The close agreement in optical constants with the reported values suggested that the samples of thicknesses 410 and 770 Å have composition similar to magnetron sputtered boron carbide thin films.[127] The presence of oxygen in our grown films is either due to oxygen coming from the sputtered target (i.e was incorporated during target fabrication) or due to oxygen being present in the environment during deposition.

Figure 6.4(b) shows optical constants profile of layer-2 of sample of thickness 365 Å as a function of photon energy in the vicinity of B K-edge as obtained from the RSXR fits. For quantitative analysis, atomic fractions of B and C were varied to obtain the best fit to the measured optical constants. Oxygen which comes from the target or the deposition environment is also included to determine the composition of the films. In these calculations, the mass density of layers obtained from the XRR measurements, ASFs of B derived from the measured optical constants reported by R. Sofuli *et al.*, [127] and tabulated[95] ASFs for C and O were used. A composition which gives the best fit to the experimental data is 63 at. % B, 32 at. % C, and 5 at. % O. Similarly we estimated the composition of the samples of thickness 187 Å and the sample of thickness 83.5 Å. The composition which gives the best fit to the experimental data of samples of thickness 187 Å and 83.5 Å are 58 at. % B, 32 at. % C, 10 at. % O and 23 at. % B, 62 at. % C, 15 at. % O respectively. The composition of the all samples estimated from RSXR is shown in Table 6.2.

Table 6.2: Showing the composition of all the samples estimated from RSXR

Sample thickness (Å)	Composition
83.5	23 at. %B, 62 at. %C, 15 at. %O
187	58 at. %B, 32at. %C, 10 at. %O
293 (layer-2)	63 at. %B, 32 at. %C, 5 at. %O
410	74 at. %B, 20 at. %C, 5 at. %O

From this table it is clear that the B atomic content increases with increases in film thickness. Low thickness film (less than 100 Å) is mainly composed of C and O and very little amount of B. This has serious implications on low period B_4C based multilayer used near Boron edge. In our work with C/B_4C multilayer observed reflectivity was less than the expected due to less boron present in the B_4C layer. Composition analysis in that case also had indicated presence of excess carbon. It was assumed that excess carbon might have diffused from C layer to B_4C layer. Present study reveals that it has happed due to growth related issues. To confirm above observation we used other tools as discussed below.

6.3.3. RRBS measurements:

The RRBS measurements were performed on the samples of thicknesses 900, 750, 120 and 100 Å. In case of thin film of thickness 100 Å we could not find any RRBS signal. Figure 6.5 shows the RRBS spectra of films of thicknesses 900, 750 and 120 Å. The signals backscattered from O, B, and C are clearly seen in the spectra. The simulated RRBS spectra are also shown in the figures along with the experimental data. The simulated spectra suggested that the films of thickness 900 and 750 Å have similar composition. From the best-fit of RRBS spectra the estimated atomic composition of O, B and C was found to be 8%, 74% and 18% respectively in these films. This corresponds to B/C ratio ~4 which is consistent with the sputtering target stoichiometry. In the case of sample of thickness 120 Å, the estimated atomic composition of O, B and C was found to be 10%, 50% and 40% respectively in these films. The RRBS measurements suggested that decrease in B/C ratio with decrease in film thickness. The composition estimated from the derived optical constants from the SXR measurements are also in agreement with the composition estimated from the RRBS.

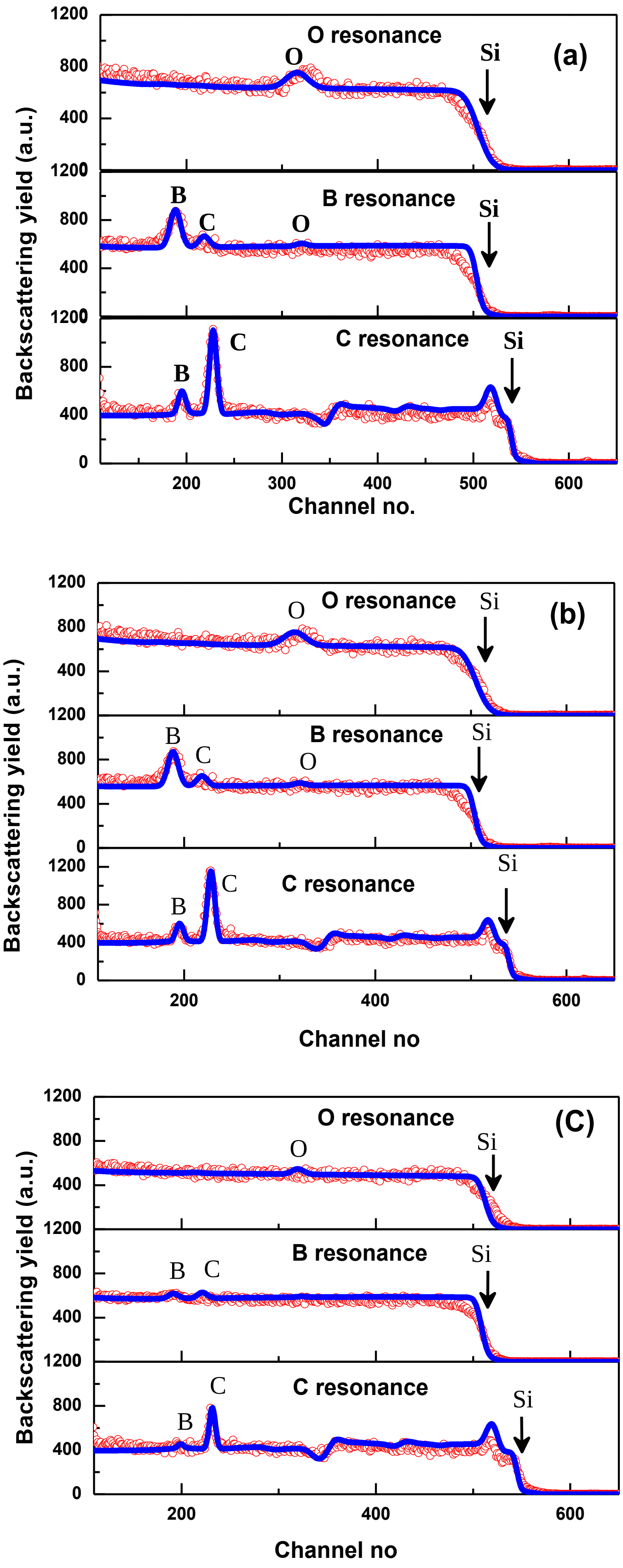

Figure 6.5: RRBS spectra of samples of thicknesses (a) 900 Å, (b) 750 Å and (c) 120 Å. The open circles are the experimental data and the solid trace is the simulated.

6.3.4. XPS measurements:

In addition to reflectivity, we also performed spectroscopic measurement like XPS, which deals with electronic states of elements. Using this technique we can get elemental and compositional information. Figure 6.6 shows survey scan of samples of thicknesses 83.5 and 365 Å.

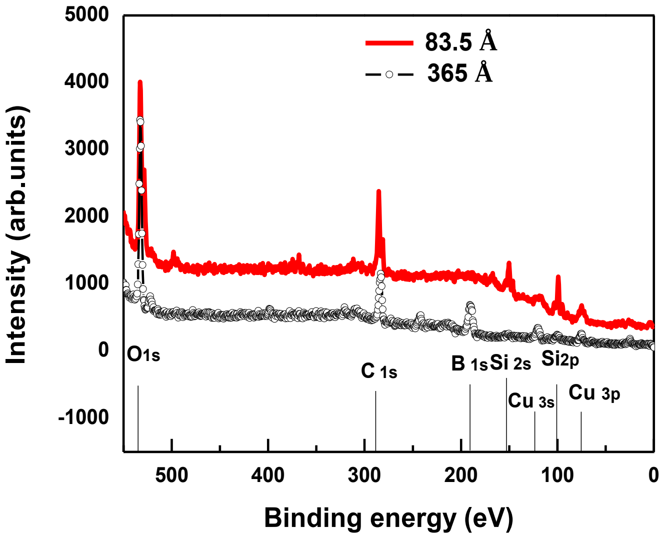

Figure 6.6: Survey XPS spectra of the samples of thicknesses 83.5 and 365 Å.

XPS spectrum of sample of thickness 365Åcontains significant contribution from O, C and B, where as in sample of thickness 83.5 Å, signal from B is very weak. These XPS spectra suggested the depletion of B from the surface of the sample of thickness 83.5 Å which corroborates with the observation made from the RSXR measurements. Copper peaks coming from the substrate holder are also appearing in the spectra. Sputter cleaning process removes the most of the boron carbide coating as a result Si 2s and Si 2p peaks appear in the survey scan of sample of thickness 83.5 Å. The core level spectra of C 1s, B 1s and O 1s obtained from the surface of sample of thickness 83.5 Å together with the spectrum deconvolution and Shirley background is shown in Figure 6.7. Figure 6.7(a) shows an asymmetric C 1s spectrum where two different chemical states at around 282.8 and 285 eV were identified after deconvolution procedure. The major contribution to the C 1s core level asymmetric peak is coming from the peak at 285 eV and we assigned it to graphitic C-C bonds.[143] The deconvolution of B 1s spectrum presented in Figure 6.7(b) showed two different chemical states at 189.5 and 192.5 eV. The peak at 282.8 eV in C 1s spectrum and 189.5 eV in B 1s spectrum corresponds to B-C bonds.[144] The deconvolution of the O 1s spectrum showed two different chemical states at 532.8 and 530.5 eV. Peak at 530.5 eV in the O 1s spectrum corresponds to native oxygen sitting on the sample surface.[64] The peak at 192.5 eV in B 1s spectrum and 532.8 eV in O 1s spectrum corresponds to boron oxide.[145] The surface of low thickness boron carbide like composed of mainly graphitic carbons and little amount of B_4C and boron oxide like compounds.

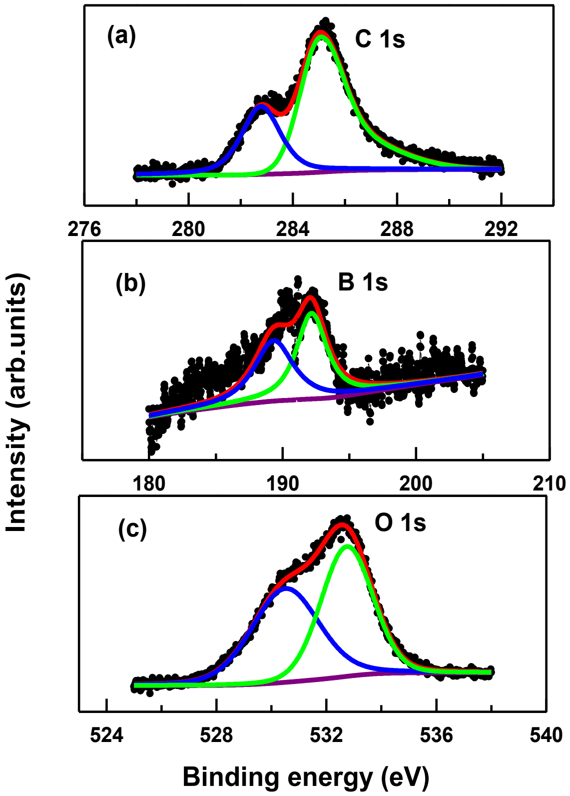

Figure 6.7: XPS core level spectra of the sample of thickness 83.5 Å in the vicinity of (a) C 1s, (b) B 1s and (c) O 1s lines together with spectrum deconvolution and Shirley background.

6.3.5. TOF-SIMS measurements:

The depth profiles of samples of thicknesses 187 and 410 Å are plotted in Figure 6.8, where the X-axis represents time and the Y-axis the relative intensities. Assuming similar analysis conditions the relative intensities of B^-, C_3^-, $18O^-$ can be plotted to estimate their variation depending on deposition thickness. From Figure 6.10a, it is clear that the intensity of B decreases with decrease in film thickness which suggested that the decrease in B atomic content with decrease in the film thickness. Figure 6.8b and c compares the variation of C and O respectively at various deposited thickness. As evident from Figure 6.8b, the C concentration was found to increase with decrease in film thickness. From Figure 6.8c, it is clear that O concentration increases with film thickness. These results well correlates with the observation made from RSXR.

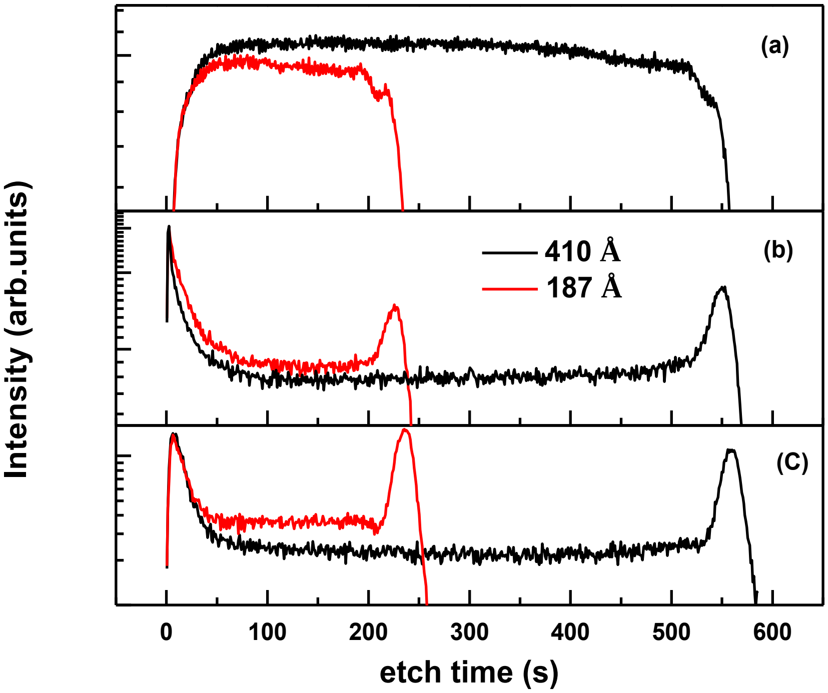

Figure 6.8: TOF-SIMS depth profile of samples of thickness 187 and 410 Å. TOF-SIMS signal of (a) B atoms (b) C atoms and (c) O atoms are shown in the graph.

The depth profiles of thin films of thicknesses 900 and 100 Å are plotted in Figure 6.9(a) and (b) respectively.

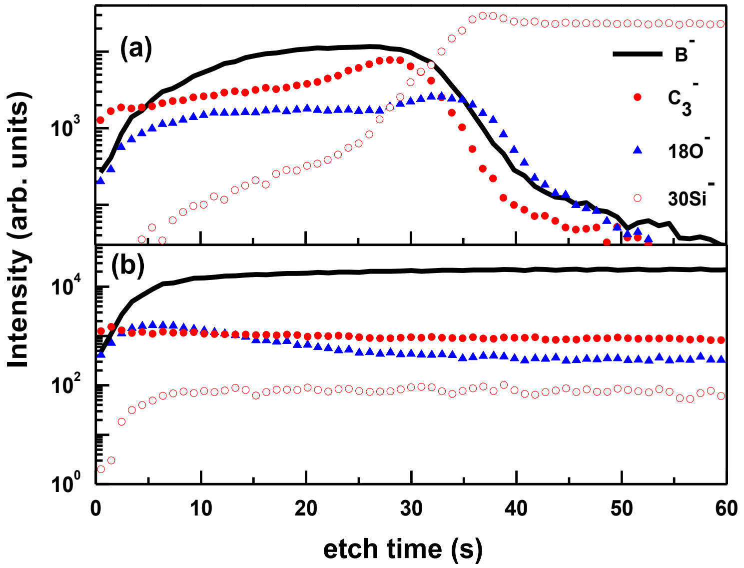

Figure 6.9: TOF-SIMS depth profile spectra of (a) 100 Å and (b) 900 Å thin film. SIMS signal of B, C, O and Si are shown in the graph.

The ratio of B atom present in the 900 Å thin film to 100 Å thin film is ~2. This means that boron content increases with increasing the film thickness. The C and O content is high in 100 Å thin film as compared to 900 Å thin film. TOF-SIMS confirms that the low thickness film contains more C and less B content as compared to high thickness films. The reason for such observed composition changes in low thickness films is as follows.

In physical vapor deposition process such as evaporation and sputtering never molecules of the starting compound or multicomponent material are evaporated/sputtered and deposited on substrate.[146] The individual atoms of components sputter out and recombine on a surface of the substrate(or in vapor phase if the number density of such atoms is large). Recombination on a surface depends on a large no of parameters such as : Sticking coefficient which depends on substrate temp, substrate chemistry, chemical bonds between the arriving atoms, reactive gases present in the chamber, roughness & temperature of substrate, velocity and angle of vapor atoms on a substrate, surface impurities, etc. Sticking coefficient of B and C is expected to be different on a given substrate. In our study it appear that in the initial stages of growth more carbon is sticking to substrate than boron as the film thickness increases sticking of boron improves and composition slowly changes and ratio of B to C increases.

This study shows that composition of compound layers may not be maintained during deposition. It can have severe impact on the performance of ML mirror. RSXR can be used successfully to find out the composition of compound ML a non destructive tool. Results obtained from all the techniques are summarized in the Table 6.3.

Table 6.3: Presents the composition of boron carbide thin films estimated from different techniques.

Samples thicknesses (Å)	RSXR	RRBS	TOF-SIMS	XPS
Low thickness samples (less than 100 Å)				
80, 100	23 at.%B, 62 at. %C, 15 at. %O in case of 80 Å thickness film	No RRBS signal	B at. % is lower, C and O at.% are as compared to mid and high thickness samples	Observed B deficient on the surface as compared to mid thickness samples
Mid thickness samples (100- 300 Å)				
120,180,290	58 at. %B, 32at. %C, 10 at. %O in case of 180 Å thickness film 63 at. %B, 32 at. %C, 5 at. %O in case of 290 Å thickness film	50 at.%B, 40 at.%C,10 at.%O in case of 120 Å thickness film	B at. %is lower, C and O at.% are higher as compared to high thickness samples	Observed B rich on the surface as compared to low thickness samples
High thickness samples (more than 400 Å)				
410,770,900	74 at. %B, 20 at. %C, 5 at. %O	74 at.%B, 18 at.%C ,8 at.%O	B at.% is higher, C and O at.% are lower as compared to low and mid thickness samples B	……..

6.4. Conclusions:

In this chapter we studied compositional changes of boron carbide layer as a function of thickness. The main findings of this study is as follows

- Reflectivity measurements at different energies allow combining the sensitivity of XRR data to structural parameters like layer thicknesses and interfacing roughness, with the layer composition sensitivity of RSXR.

- The optical index profile derived over extended region in the vicinity of the B K-edge was used to estimate the composition of the films quantitatively.
- At low thickness we observed boron deficient or carbon rich growth.
- XPS, TOF-SIMS and RRBS confirm the results obtained from RSXR.
- The RSXR technique is a photon in photon out processes which provides excellent spatial resolution, down ~ nm with penetration depths over tens of nanometers and gives the composition of films in nondestructive manner.

Chapter 7.

Summary and Future Scope

In this chapter, we briefly summarize the essence of work carried out in this thesis along with the scope of the future work.

X-ray ML structures find potential application in EUV-SXR regime. The properties of ML structure are influenced by structure and composition of layers. Thermally induced structural changes and its detrimental effect at an application wavelength is interesting to study as MLs are exposed to highly intense synchrotron radiation for their application as optical elements. In this thesis a detailed study on the thermal annealing induced structural changes and its influence on the performance of W/B_4C ML structures were carried out. Analysis of structure and composition of low electron density contrast system with an example of C/B_4C ML were presented. Thickness dependent compositional changes in B_4C layer was investigated in detail. In addition to some basic understanding on ML structures, development of high reflectivity W/B_4C and large area, high reflectivity Mo/Si MLs was also carried out in this thesis.

Structural and normal incidence reflectance changes in an annealed W/B_4C MLs

W/B_4C is an important x-ray optical element for both hard and soft x-ray region. Even though there is a high optical contrast between W and B_4C, because of high absorption in W as compared to other elements like Ru, Mo, and La, this is an unstudied combination near the B K-edge (~189 eV). We have chosen W/B_4C as a reflecting mirror near the B K-edge because of its ability to form smooth and stable interfaces. We observed a maximum peak reflectivity of ~ 8.3% at 68 Å wavelength. A little drop in reflectivity (~1%) is observed after 800 ºC annealing. This confirms that W/B_4C MLs are considered for applications using high power light sources. W/B_4C MLs undergo two regime of period thickness. W/B_4C systems with B_4C layers thickness less than 20 Å exhibit compaction, while the systems with B_4C layers thickness greater than 20 Å expand. GIXRD performed using synchrotron radiation suggested that formation of new phases like W-C and/or W-B phases after annealing. However the formed phases in W/B_4C MLs could not affect the reflectivity performance of ML with B_4C layer thickness more than 20 Å.

Structural and compositional analysis of low-Z/low-Z MLs

ML structures have finite absorption which limit the number of layer pairs contributing to reflectivity and also causes structural changes when exposed to high intense synchrotron radiation. Low-Z/low-Z MLs have potential application as a narrow band filter and can also minimize structural changes caused by finite absorption of incident radiation. Structural parameters and composition of layers influence the performance of ML structures. It is thus important to drive these parameters so that the preparation technique can be optimized to yield the better performance. These aspects are studied in low-Z/low-Z MLs with an example of C/B_4C ML. Structural parameters were studied by combining XRR and TEM techniques. In XRR many structural models yield similar results because of low electron density contrast between C and B_4C. Layers thickness ratio is slightly compensated by changing the interface roughness. TEM is used to get interface information. TEM results suggested that interfaces are symmetric in nature. A symmetric interface model is used to get structural information from XRR spectra. Soft x-ray reflectivity measurements in the vicinity of B K-edge were performed to derive compositional information. The structural parameters obtained from XRR and TEM are used as input parameters and best fit to the SXR spectra were obtained by changing the optical constants of individual layers. This method improves the reliability of derived optical constants and hence the compositional information. The derived optical constants of B_4C suggested the presence of excess C into it. It has been concluded that the presence of excess C is either due to diffusion of C atoms from the C layer or change in the stoichiometry of deposited boron carbide layer from its target stoichiometry.

Investigation of thickness dependent compositional changes in boron carbide layers

To investigate further the compositional changes in boron carbide, we have chosen thin films of boron carbide with different thicknesses. An in-depth profile of the chemical elements constitute the thin films is reconstructed based on the analysis of reflectivity curves measured in the vicinity of B K-edge. The main advantage of RSXR technique is that it is a photon in photon out process which provides excellent spatial resolution down to ~nm with penetration depths over tens of nm and gives the composition of films in non-destructive manner. For quantitative analysis, atomic fraction of B and C can be varied to obtain the best fit to the measured optical constants. Oxygen which comes from the target or the deposition environment is also included to determine the composition of films. The composition of films is closely dependent on film thickness. The B/C ratio decreases with decreasing the film thickness and reaches the value ~4 in case of high thickness films. RRBS, XPS and TOF-SIMS were also performed to compliment the observation made from RSXR. RRBS measurements were performed on three different thickness thin films. The B/C ratio estimated from RRBS changes from 4 to ~1.2 as the thickness of films changes from 900 to 120 Å. TOF-SIMS also suggested that the ratio of B atoms in 900 Å film to 100 Å film is ~2 and also low thickness film contain higher C and O content. XPS measurements suggested that surface of low thickness film is boron deficient. RRBS, TOF-SIMS and XPS measurements are complement the observation made from the RSXR.

Development of high reflectivity MLs in the EUV-SXR regime

High reflectivity MLs in EUV-SXR regime require atomically smooth interfaces, ultra thin layers with thickness control on atomic scale and number of layer pairs ranging from ~ 50 to 500. We need deposition system capable of meeting these requirements. We developed high reflectivity W/B_4C MLs and large area, high reflectivity Mo/Si MLs. We have discussed the influence of process parameters on the quality of deposited thin films and MLs. We have successfully deposited Mo/Si ML structure over the 300x100 mm^2 area with period thickness variation less than 1%. We observed maximum peak reflectance of ~63% from Mo/Si ML near the Si L-edge (~100 eV) which is comparable with 69% reflectivity obtained from this combination.

W/B_4C multilayers with periods in the range of 5 to 50 Å have wide spread of applications such as polarizing element, and normal incidence applications in soft x-ray regime. Various W/B_4C ML structures with period thickness ranging from 10 to 50 Å and layer pairs as high as 300 were deposited. Near normal incidence reflectance of W/B_4C ML structures with period thickness of ~ 20 Å consist of layer pairs 100, 200, and 300 in water window region (22-44 Å) was measured at BESSY optics beamline. We observed near normal incidence reflectance of ~ 2% at wavelength of ~ 40 Å.

Scope of the future work

In this work we have found that W/B_4C is a suitable combination for high heat load applications near the B K-edge. We have observed near normal incidence reflectivity of ~ 8.3% at 68 Å wavelength. One can further improve the reflectivity obtained from this combination by increasing number of layer pairs but due to presence of residual stresses the ML structure containing more than 50 layer pairs are under stress and could not adhere to the substrate. Thus further study is required to understand presence of residual stresses and minimization of these stresses.

We have also studied the thermally induced in W/B_4C MLs with same period thickness but varying B_4C layer thickness from 30 Å to 14 Å. GIXRD measurements performed using synchrotron radiation suggested that formation of new phases like W-C and/or W-B. XRR measurements suggested that the formed phases could not affect the performance of ML structures except the ML structure consisting of B_4C layer of thickness 14 Å. A further study is required to understand the mechanism for structural degradation in W/B_4C MLs consisting of low thickness boron carbide layer.

We have observed compositional changes in B_4C with decrease in the film thickness. The composition changes causes significant changes in optical constants which results into drop in maximum achievable reflectivity from B_4C based MLs. The influence of compositional changes on the performance of ML structures needs to be addressed.

Low-Z/Low-Z MLs seems to be promising combination near the absorption edges. We need number of layer pairs more than 200 to use as a high reflecting mirror. The deposition rate for low-Z elements like C, B_4C is less. Depositing large layer pair low deposition rate combinations is a challenging task.

Bibliography:

[1] D. Attwood, “Soft X-Rays and Extreme Ultraviolet Radiation” Cambridge University Press, Cambridge, UK, (1999).

[2] W. Chao, B. D. Harteneck, J. A. Liddle, E. H. Anderson, and D. T. Attwood, “soft x-ray microscopy at a spatial resolution better than 15 nm” Nature **435**, 1210 (2005).

[3] National Technology Roadmap for Semiconductors (Semiconductor Industry Association, San Jose, CA 95110, 1997).

[4] Harun H Solak, “Nano lithography with coherent extreme ultraviolet light” J. Appl. Phys D. **39**,171 (2006).

[5] M. Born and E. Wolf, “Principles of Optics” The MacMillan Company, New York, (1964).

[6] J. Kirz, “Soft x-ray microscopy- Physical basis and recent developments” World scientific, (1994).

[7] H. M. Hertz, L. Rymell, M. Berglund, G. A. Johansson, T. Wilhein, Y. Platonov, and D. Broadway, “Normal-incidence condenser mirror arrangement for compact water-window x-ray microscopy” Proc. SPIE. **3766**, 247 (1999).

[8] H. M. Hertz, M. Berglund, G. A. Johansson, M. Peuker, T. Wilhein, and H. Brismar, “Compact water-window X-ray microscopy with a droplet laser-plasma source” AIP Conference Proceedings, **507**, 721 (2000).

[9] G. A. Johansson, A. Holmberg, H. M. Hertz, M. Berglund, “Design and performance of a laser-plasma-based compact soft X-ray microscope” Rev. Sci. Instr., **73**, 1193 (2002).

[10] E. Spiller, “Soft X-ray Optics” SPIE, (1994).

[11] J. H. Underwood and T. W. Barbee, Jr. “Layered synthetic microstructures as Bragg diffractors for x-rays and extreme ultraviolet: Theory and predicted performance” Appl. Opt. **20**, 3027 (1981).

[12] N. Ghafoor, F. Erikson, P. O. Å. Persson, F. Schäfers, and J. Birch, “Interface engineered ultra-short period Cr/Ti multilayers as high reflectance mirrors and polarizers for soft x-rays of λ=2.7 nm wavelength” Appl. Opt. **45**, 137 (2006).

[13] F. Erikson, N. Ghafoor, F. Schäfers, E. M. Gullikson, and J. Birch, “Interface engineering of short-period Ni/V multilayer x-ray mirrors” Thin Solid Films. **500**, 84 (2006).

[14] T. W. Barbee, S. Mrowka, and M. C. Hettrick, “molybdenum-silicon multilayer mirrors for the extreme ultraviolet” Appl. Opt. **24**, 883 (1985).

[15] D. G. Stearns, and R. S. Rosen, “Normal-incidence x-ray mirror for 7 nm” Opt. Lett. **16**, 1283 (1991).

[16] Alian Jody corso, Paola Zuppella, David L. Windt, Marco Zangrando, and Maria Guglielmina Pelizzo, “Extreme ultraviolet multilayer for the FERMI @ Elettra free electron laser beam transport system” Opt. Express **20**, 8006 (2012).

[17] D. S. Kuznetsov, A. E. Yakshin, J. M. Sturm, R. W. van de Kruijs, E. Louis, and F. Bijkerk, “High-reflectance La/B-based multilayer mirror for 6.x nm wavelength” Opt.Lett. **40**, 3778 (2015).

[18] J. F. Seely, G. Gutman, J. Wood, G. S. Herman, M. P. Kowalski, C. Rife, and W. R. Hunter, " Normal-incidence reflectance of W/B_4C multilayer mirrors in the 34-50-Å wavelength region" Appl. Opt. 32, 3541 (1993).

[19] D. G. Stearns, R. S. Rosen, and S. P. Vernon, "Multilayer mirror technology for soft-x-ray projection lithography" Appl. Opt. **32**, 6952 (1993).

[20] Alexander Kazimirov, D. M. Smilgies, Q. Shen, X. Xiao, Q. Hao, E. Fontes, D. H. Bilderback, Sol M. Gruner Y. Platonov and V. V. Martynov, "Multilayer X-ray optics at CHESS" J. Synchrotron Radiation. **13**, 204 (2006).

[21] A. B. C. walker, T. W. Barbee, R. B. Hoover, and J. F. Lindblom,"Soft x-ray images of the solar corona with a normal incidence cassegrain multilayer telescope" Science **241**, 1781 (1988).

[22] F. Cerrina, G. Margaritondo, J. H. Underwood, M. Hettrick, M .A. Green, L. J. Brillson, A. Franciosi, H. Hochst, P.M. DeLuca, Jr., and M. N. Gold, "Maximum, A Scanning Photoelectron Microscope at Aladden" Nucl. Instr. Meth. A **266**, 303 (1988).

[23] J.H. Underwood, J.B. Kortright, R.C.C. Perera, F. Cerrina, C. Capasso, A.K. Ray-Chaudhuri, W. Ng, J. Welnack, J. Wallace, S. Liang, and G. Margaritondo, "X-Ray microscopy with multilayer mirrors: the maximum Photoelectron Microscope" Synchrotron Radiation in the Biosciences, Oxford Univ. Press, (1994).

[24] L. Nevot and P. croce, "Characterization of surfaces by grazing incidence X-ray reflection Application to the study of polishing some silicate glasses" Rev. Phys. Appl. **15**, 761 (1980).

[25] E. Zeigler, Y. Lepetre, Ivan K. Schuller, and E. Spiller, “Stability of multilayers for synchrotron optics” Appl. Phys. Lett. **48**, 1354 (1986).

[26] J. Bosgra, J. Verhoeven, R.W.E. van de Kruijs, A.E. Yakshin, and F. Bijkerk, “Non-constant diffusion characteristics of nanoscopic Mo-Si interlayer growth” Thin Solid Films. **522**, 228 (2012).

[27] V. I. T. A. de Rooij-Lohmann, A. E. Yakshin, R. W. E. van de Kruijs, E.Zoethout, A. W. Kleyn, E. G. Keim, M. Gorgoi, F. Schäfers, H. H. Brongersma, and F. Bijkerk, “Chemical interaction of B4C, B, and C with Mo/Si layered structures” J. Appl. Phys. **108**, 014314 (2010).

[28] X. W. Zhou, and H. N. G. Wadley, “Atomistic simulation of the vapor deposition of Ni/Cu/Ni multilayers: Incident adatom angle effects”J. Appl. Phys. **87**, 553 (2000).

[29] J. M. Freitag, and B. M. Clemens,” Stress evolution in Mo/Si multilayers for high-reflectivity extreme ultraviolet mirrors” Appl. Phys. Lett. **73**, 43 (1998).

[30] A. R. Khorsand, R. Sobierajski, E. Louis, S. Bruijn, E. D. van Hauttum, R. W. E. van de Krujis, M. Jurek, D. Klinger, J. B. Pelka, L. Juha, T. Burian, J. Cihelka, V. Hajkova, L. Vysin, U. Jastrow, N. Stojanovic, S . Toleikis, H. Wabnitz, K. Tiedtke, K. Sokolowski-Tinten, U. Shymanovich, J. Krzywinski, S. Hau-Riege, R. London, A. Gleeson, E. M. Gullikson, and F. Bijkerk, “Single shot damage mechanism of Mo/Si multilayer optics under intense pulsed XUV exposure” Opt. Express **18**, 700 (2010).

[31] Miriam Barthelmess, and Saša Bajt, “Thermal and stress studies of normal incidence Mo/B_4C multilayers for a 6.7 nm wavelength” Appl. Opt. **50**, 1610 (2011).

[32] A. F. Jankowski, and P. L. Perry, “Characterization of Mo/B_4C multilayers” Thin Solid Films. **206**,365 (1991).

[33] A. F. Jankowski, L. R. Schrawyer, and M. A. Wall, “Structural stability of heat-treated W/C and W/B_4C multilayers” J. Appl. Phys. **68**, 5162 (1990).

[34] S. N.Yakunin, I.A.Makhotkin, K.V. Nikolaev, R. W. E. van de Kruijs, M. A. Chuev, and F. Bijkerk, “Combined EUV reflectance and X-ray reflectivity data analysis of periodic multilayer structures” Opt. Express **22**, 20076 (2014).

[35] V. V. Martynov, Yu. Platonov, A. Kazmirov, and D. H. Bilderback, “High selective x-ray multilayers” Proc. SPIE **5195**, 46 (2003).

[36] G.M.Blumenstock, and Ritva A.M. Keski-kuha, “Ion-beam-deposited boron carbide coatings for the extreme ultraviolet” Appl. Opt. **33**, 5962(1994).

[37] I. A. Makhotkin, E. Zoethout, E. Louis, A.M. Yakunin, S. Müllender, and F. Bijkerk, “Spectral properties of La/B - based multilayer mirrors near the boron K absorption edge” Opt. Express **20**, 11778(2012).

[38] S. S. Andreev, M. M. Barsheva, N. I. Chkhalo, S. A. Gusev, A. E. Pestov, V. N. Polkonikov, N. N. Salashchenko, L .A. Shmaenok, Yu. A. Vainer and S. Yu. Zuev, “Multilayered mirrors based on La/B_4C(B_9C) for X-ray range near the anomalous dispersion of boron ($\lambda \approx 6.7$ nm)” Nucl. Instrum. Methods. Phys. Res. A **603**, 80(2009).

[39] I.V.Kozhevnikov, E.O.Filatova, A.A.Sokolov, A.S.Konashuk, F.Siewert, M.Störmer,J.Gaudin,B.Keitel,L.Samoylova, and H.Sinn, “Comparative study of the X-ray reflectivity and in-depth profile of a-C, B_4C and Ni coatings at 0.1–2 keV” J.Synchrotron Radiat. **22**, 348 (2015).

[40] S.P.Hau-Riege, R.A.London, R.M.Bionta, M.A.McKernan, S.L.Baker, J.Krzywinski, R.Sobierajski, R.Nietubyc, J.B.Pelka, M.Jurek, L.Juha, J.Chalupský. J.Cihelka,

V.Hájková, A.Velyhan, J.Krása, J.Kuba, K.Tiedtke, S.Toleikis, Th.Tschentsher, H.Wabnitz, M.Bergh, C.Caleman, K.Sokolowski-Tinten, N.Stojanovic, and U.Zastrau, "Damage threshold of inorganic solids under free-electron-laser irradiation at 32.5 nm wavelength" Appl. Phys. Lett. **90**, 173128(2007).

[41] R. Soufli, M.Fernandez-Perea, S.L.Baker, J.C. Robinson, E.M.Gullikson, P. Heinman, V.V.Yashchuk, W.R. Mckinney, W.F.Schlotter, and M. Rowen, "Development and calibration of mirrors and gratings for the soft x-ray materials science beamline at the Linac Coherent Light Source free-electron laser" Appl. Opt. **51**, 2118 (2012).

[42] I. Nedelcu, R. W. E. Vande Krujis, A.E.Yakshin, and F.Bijkerk, "Microstructure of Mo/Si multilayers with B_4C diffusion barrier layers" Appl. Opt. **48**, 155 (2009).

[43] K. Wasa, M. Kitabatake, and H. Adachi "Thin film materials technology" William Andrew publishing, Cambridge University Press, (2004).

[44] K. Wasa, and S. Hayakawa "Handbook of sputter deposition technology" Noyes publications, New Jersey, USA, (1992).

[45] John E. Mahan "Physical vapor deposition of thin films" Wiley-Interscience publication, (2000).

[46] G. Betz and G. K. Wehner, "Sputtering by Particle Bombardment II" edited by R. Behrisch, Springer, Berlin, (1983).

[47] M. Nayak, P. N. Rao, and G. S. Lodha, " Magnetron sputtering based x-ray multilayer deposition system at Indus SR facility" Asian Journal of Physics, **19**, 1 (2010).

[48] H.R. Kaufman, J.J. Cuomo, and J.M.E. Harper, "Technology and applications of broad-beam ion sources used in sputtering. Part I. Ion source technology" J. Vac. Sci. Technol., **21**, 725 (1982).

[49] M. Tolan, "X-ray Scattering from Soft-Matter Thin Films" Springer, Germany, (1999).

[50] V. Holý, U. Pietsch, and T. Baumbach, "High-Resolution X-ray Scattering from Thin Films and Multilayers" Springer, Germany, (1999).

[51] Jens Als-Nielsen, and Des McMorrow, "Morden X-ray Physics" John Wiley & sons, Ltd, (2000).

[52] T. P. Russell, "X-ray and neutron reflectivity for the investigation of polymers" Material Science Reports **5**, 171 (1999).

[53] Chason E. and Mayer T. M., "Critical Reviews in Solid State and Materials Sciences" **22**, 1 (1997).

[54] L.G. Parratt, "Surface studies of solids by total reflection of x-rays," Phys. Rev. **95**, 359 (1954).

[55] E. M. Gullikson, P. Denham, S. Mrowka, and J. H. Underwood, "Absolute photoabsorption measurements of Mg, Al, and Si in the soft-x-ray region below the $L_{2,3}$ edges," Phys. Rev. B **49**, 16283 (1994).

[56] P. N. Rao, M. H. Modi, and G. S. Lodha, "Optical properties of indium phosphide in the 50-200 Å wavelength region using reflectivity technique" App. Opt. **49**, 5378 (2010).

[57] R. V. Nandedkar, K. J. S. Sawhney, G. S. Lodha, A. Verma, V. K. Raghuvanshi, A. K. Sinha, M. H. Modi, and M.Nayak, "First results on the reflectrometry beamline on Indus-1" Curr. Sci. **82**, 298 (2002).

[58] David B. Williams, and C. Barry Carter, "Transmission electron microscopy, A text book for Material science" Plenum Press. New York and London (1996).

[59] A. Goswami, "Thin Film fundamentals" New Age International (P) Limited, Publishers, (1996).

[60] Bernt Flutz, and James Howe, "Transmission Electron Microscopy and diffractometery of materials" Springer (1998).

[61] Mario Birkholz, "Thin Film Analysis by X-ray Scattering" WILEY-VCH Verlag GmbH & Co. KGaA, (2006).

[62] A.K. Sinha, A. Sagdeo, P. Gupta, A. Kumar, M. N. Singh, R. K. Gupta, S. R. kane, and S. K. Deb, "Commissioning of angle Dispersive X-ray Diffraction Beamline on Indus-2" AIP Conf. Proc. **1349**, 503 (2011).

[63] J. R. Ferraro, "Introductory Raman spectroscopy" Amsterdam, Boston: Academic Press., (2003).

[64] C.D.Wagner, W.M.Riggs, L.E.Davis, J.F.Moulder, and G.E.Muilenberg, "Handbook of x-ray photoelectron spectroscopy" Perkin-Elmer Corporation, Physical elements division, Eden prairie, Minn. 55344 (1979).

[65] Stefan Hüfner, "Photoelectron Spectroscopy" Springer-Verlag, Berlin Heidelberg (1995).

[66] K. G. M. Nair and B. K. Panigrahi, "Perspectives in materials characterization" Universities press Pvt. Ltd, chapt-3, pg.77, (2009).

[67] J. J. Grob and P. Siffert, "Progress in crystal growth characterization," Chapt-8, pg.59, (1984).

[68] M. Mayer, "Rutherford backscattering spectrometry," Lectures given at the workshop on Nuclear data for science and technology: Materials analysis, Trieste, Italy, (2003).

[69] P.Sigmund, "Collision Theory of Displacement Damage, Ion Ranges, and Sputtering. I, II & III," Rev. Roum. Phys., **17**, 823-870, 969-1000, 1079-1106 (1972).

[70] A. Benninghoven, F. G. RÜdenauer, and H. W. Werner, "Secondary Ion Mass Spectrometry Basic Concepts, Instrumental Aspects, Applications and Trends," Angew. John Wiley & Sons, Inc. (1987).

[71] Sarah Fearn, "An Introduction to Time-of-Flight Secondary Ion Mass Spectrometry (TOF-SIMS) and its Application to Material Science," IOP Concise Physics, Morgan & Claypool Publishers, (2015).

[72] Hisataka Tanaka, Tomoaki Kawamura, Tsuneyuki Haga, Hiroo Kinoshita and Yoshikazu Ishi, "Evaluation of Large-Area Mo/Si Multilayer soft x-ray Mirrors Fabricated by RF Magnetron Sputtering," Japanese J. Appl. Phys. **34**, 5027 (1995).

[73] D. L. Windit and W. K. Waskiewicz, "Multilayer facilities required for extreme-ultraviolet lithography," J. Vac. Sci. Technol. *B*, **12,** 3826 (1994).

[74] Claude Montcalm, R. Frederick Grabner, Russell M. Hudyma, Mark A. Schmidt, Eberhard Spiller, Chirstopher C. Walton, Marco Wedowski, and James A. Folta, "Atomic-precision multilayer coating of the first set of optics for an extreme-ultraviolet lithography prototype system," Appl. Opt. **41**, 3262 (2002).

[75] J.B.Kortright, E.M.Gullikson, and P.E.Denham, “Masked deposition techniques for achieving multilayer period variations required for short-wavelength (68-Å) Soft-X-ray imaging optics,” Appl. Opt. **32**, 6961 (1993).

[76] C. Khan Malek, T. Moreno, R. Barchewitz, R. Rivoira and Y. Lepetre, “Performances of large multilayer mirrors for the 0.5-0.15 nm range,” Rev. Sci. Instrum. **63**, 4102 (1992).

[77] J. F. Mackay, D.W. Pearson, B. E. Nelms, P. M. DeLuca, jr., M. N. Gould, and M. G. Lagally, “A double mirror W/C multilayer monochromator for radiation biology applications,” Medi. Phys. **25**, 773 (1998).

[78] Ch. Morawe, J-Ch. Peffen, “Thickness control of large area x-ray multilayers,” Proc. SPIE. **7448**, 74480H (2009).

[79] K. D. Joensen, P. Hoghoj, F. E. Christensen, P. Gorenstein, J. Susini, E. Ziegler, A. K. Freund and J. L. Wood, “ Multilayered supermirror structures for hard x-ray synchrotron and astrophysics instrumentation,” Proc. SPIE. **2011**, 360(1993).

[80] L.Golub, G. Nystrom, E. Spiller, and J. Wilczynski, “Construction of Multilayered X-Ray Telescope for Solar Coronal Studies from Space,” Proc. SPIE. **563**, 266 (1985).

[81] E. Spiller, and L. Golub, “Fabrication and testing of large area multilayer coated x-ray optics,” Appl. Opt. **28**, 2969 (1989).

[82] M. Wohlschlögel, T. U. Schülli, B. Lantz, and U. Welzel, “Application of a single-reflection collimating multilayer optics for X-ray diffraction experiments employing parallel-beam geometry,” J. Appl. Cryst. **41**, 124 (2008).

[83] P. Gawlitza, S. Braun, S. Lipfert, and A.Leson, “Ion-beam sputter deposition of x-ray multilayer optics on large areas,” of Proc. SPIE. **6317**, 63170G (2006).

[84] H. Tsuruta, S. Brennan, Zofia U. Rek, Thomas C. Irving, W. H. Tompkins, and Keith O. Hodgson, “A Wide-Bandpass Multilayer Monochomator for Biological Small-Angle Scattering and Fiber Diffraction Studies,” J. Appl. Cryst. **31**,672(1998).

[85] R. Dietsch, Th. Holz, D. Weißbach, and R. Scholz, “Large are PLD of nanometer-multilayers,” Appl. Surf. Sci. **197-198**, 169 (2002).

[86] Y. G. Shen, Y. W. Mai, Q.C.Zhang, D. R. McKenzie, W. D. McFall, and W.E. McBride, “Residual stress, microstructure, and structure of tungsten thin films deposited by magnetron sputtering,” J. Appl. Phys. **87**, 177 (2000).

[87] R. R. Cola, D. L. Windt, W. K. Waskiewicz, B. E. Wier, R. Hull, G. K. Celler, and C. A. Volkert, “Stress relaxation in Mo/Si multilayer structures,” Appl. Phys. Lett. **60**, 3120 (1992).

[88] S. Yulin, T. Feigl, T. Kuhlmann, N. Kaiser, A.I. Fedorenko, V.V. Kondratenko, O.V. Poltseva, V. A. Sevryukova, A. Yu. Zolotaryov, and E. N. Zubarev, “Interlayer transition zones in Mo/Si super lattices,” J. Appl. Phys, **92**, 1216 (2002).

[89] Rointan F. Bunshah, “Handbook of deposition technologies for films and coatings” Noyes Publications, (1994).

[90] E. Louis, A. E. Yakshin, P. C. Georts, S. Oestreich, R. Stuik, L. G. M. Edward, M. J. H. Kessels, B. Fred, H. Markus, M. Stefan, M. Michael, S. Detlef, S. Frank, and U. Gerhard, “Progress in Mo/Si multilayer coating technology for EUVL optics,” Proc. SPIE. **3997**, 406 (2000).

[91] C. C. Michaelsen, J. Wiesmann, R. Borman, C. Nowak, C. Dieker, S. Hollensteiner, and W. Jäger, “ML mirror for X rays below 190 eV,” Opt. Lett. **26**, 792 (2001).

[92] T. Tsarfati, R. W. E. Van de kruijs, E. Zoethout, E. Louis, and F. Bijkerk, "Reflective ML optics for 6.7 nm wavelength radiation sources and next generation lithography," Thin Solid Films. **518**, 1365 (2009).

[93] Y. Platonov, J. Rodriguez, M. Kriese, E. Gullikson, T. Harada, T. Watanabe, and H. Kinoshita, "MLs for next generation EUVL at 6.X nm," Proc. SPIE **8076**, 80760N (2011).

[94] C. Montealm, P. A. Kearney, J. M. Slaughter, B. T. Sullivan, M. Chaker, H. Pepin, and C. M. Falco, "Sutvey of Ti-, B-, and Y- based soft x-ray-extreme ultraviolet ML mirrors for the 2- to 12 nm wavelength region," Appl. Opt. **35**, 5134 (1996).

[95] B. L. Henke, E. M. Gullikson, and J. C. Davis, "X-ray interactions photoabsorptio, scattering, transmission, and reflection at E= 50-30000 eV, Z= 1-92," Atomic dara and Nuclear Data Tables. **54**, 181 (1993).

[96] A. F. Jankowski, and D. M. Makowieecki, "W/B_4C ML x-ray mirrors," Opt. Engg. **30**, 2003 (1991).

[97] Mohammed H. Modi, S. K. Rai, Mourad Idir, F. Schaefers, and G. S. Lodha, "NbC/Si ML mirror for next generation EUV light source," Opt. Express **20**, 15114 (2012).

[98] P. N. Rao, M. H. Modi, S. K. Rai, V. G. Sathe, S. K. Deb, and G. S. Lodha, "Thermal stability studies of ion beam sputter deposited C/B_4C x-ray ML mirror," Thin Solid Films **527**, 244 (2013).

[99] Peter Siffalovic, Matej Jergel, Livia Chitu, Eva Majkova, Igor Matko, Stefan Luby, Andreas Timmann, Stephan Volker Roth, Jozef Keckes, Guenter Alois Maier, Alexandra Hembd, Frank Hertlein, and Joerg wiesmann, "Interface study of a high-performance W/B_4C X-ray mirror," J. Appl. Cryst. **43**, 1431 (2010).

[100] A. Kloidt, K. Nolting, U. Kleineberg, B. Schmiedeskamp, U. Heinzmann, P. MÜller, M. KÜhne, Enhancement of the reflectivity of Mo/Si multilayer x-ray mirrors by thermal treatment, Appl. Phys. Lett. **58**, 2601 (1991).

[101] M. Jergel, Z. Bochníček, E. Majková, R. Senderák, Š. Luby, Thermally activated interface shift in the tungsten/silicon multilayers, Appl. Phys. Lett. 69 (1996) 919.

[102] V. Dupuis, M. F. Ravet, C. Tête, M. Piecuch, Y. Lepêtre, R. Rivoria, E. Ziegler, Thermal evolution of X/C multilayers (with X=W, Ni, or SiWSi): A systematic study, J. Appl. Phys. **68,** 5146 (1990).

[103] Z.Jiang, V.Dupuis, B. Vidal, M.F. Ravet, M. Piecuch, Improvement of the thermal stability of W/C multilayers, J.Appl.Phys. **72,** 931 (1992).

[104] C. C. Walton, G. Thomas, J. B. Kortright, X-ray optical multilayers: Microstructure limits on reflectivity at ultra-short periods, Acta mater. **46,** 3767 (1998).

[105] C. C. Walton, "Ultra-short-period W/B_4C multilayers for x-ray optics-microstructure limits on reflectivity," Ph.D. dissertation University of California, Berkely, Berkely Calif., (1997).

[106] E. Rudy, Ternary phase equilibria in transition metal-boron-carbon-silicon system, part V, Compendium of phase diagram data, U.S. Air Force Reports AF 33 (615)-1249 and AF-33 (615)-67-C-1513.

[107] Erik Lassner, Wolf-Dieter Schubert, Tungsten: Properties, Chemistry, Technology of the element, Alloys, and Chemical Compounds, Kluwer Academic, New York, 1999.

[108] Joined committee for powder diffraction studies-International Centre for Diffraction Data (JCPDS, ICDD), Powder Diffraction File, Release, 2000.

[109] J. Gonzalez-Hernandez, B.S.Chao, S.R. Ovshinsky, D.D. Alred, "The Structure of W/C ($0.15<\gamma<0.8$) Multilayers Annealed in Argon or Air," J. X-ray Science and Technology **6,** 1 (1996).

[110] M. Balden, P. A. Sauter, S. Jong, C. Adelhelm, S. Linding, M. Rasinski, T. Plocinski, Carbide formation in tungsten-containing amorphous carbon films by annealing, Thin Solid Films **519,** 4049 (2011).

[111] P. N.Rao, M. Nayak, M. H. Modi, S. K. Rai, and G. S. Lodha, "Growth of Multilayer Optics for Synchrotron radiation Sources,"J. Phys.: Conf. Ser. **425**, 052023 (2013).

[112] J.M. Slaughter, B.S. Medower, R.N.Watts, C.Tarrio, T.B.Lucatorto, and C.M.Falco, "Si/B_4C narrow-bandpass mirrors for the extreme ultraviolet," Opt. Lett. **19**, 1786(1994).

[113] P.Boher, Ph.Houdy, L.Hennet, J.P.Delaboudiniere, M.Kuhne, P.Muller, Z.G.Li, and D.J.Smith, "Silicon/silicon oxide and silicon/silicon nitride multilayers for extreme ultraviolet optical applications," Opt. Eng. **30**, 1049 (1991).

[114] S. P. Hau-Riege, H.N.Chapman, J. Krzywinski, R. Sobierajski, S. Bajt, R. A.London, M. Bergh, C. Caleman, R. Nietubyc, L. Juha, J. Kuba, E. Spiller, S. Baker, R. Bionta, K.S. Tinten, N. Stojanovic, B. Kjornrattanawanich, E. Gullikson, E. Plönjes, S. Toleikis, and T. Tschentsher, "Subnanometer-Scale Measurements of the Interaction of Ultrafast Soft X-Ray Free-Electron-Laser Pulses with Matter," Phy. Rev.Lett. **98**, 145502(2007).

[115] K. N. Stoev and K.Sakurai, "Review on grazing incidence X-ray spectrometry and reflectometry," Spectrochimica Acta Part B **54**, 41 (1999).

[116] O.H.Seeck, and I. D. Kaendler, “Analysis of x-ray reflectivity data from low-contrast polymer bilayer systems using a Fourier method,” Appl. Phys. Lett. **76**, 2713 (2000).

[117] P. N.Rao, S. K.Rai, M. Nayak, and G. S. Lodha, “Stability and normal incidence reflectivity of W/B_4C multilayer mirror near the boron K absorption edge,” Appl. Opt. **52**, 6126 (2013).

[118] S. K. Ghose, and B.N.Dev, “Ion-irradiation-induced mixing, interface broadening and period dilation in Pt/C multilayers,” Phy. Rev. B **63**, 245409 (2001).

[119] C. Wang, T. Araki, H. Ade, “Soft x-ray resonant reflectivity of low-Z material thin films,” Appl.Phys.Lett. **87**, 214109 (2005).

[120] N.Kemik, M.Gu, F.Yang, C.-Y.Chang, Y.Song, M.Bibee, A.Mehta, M.D.Biegalski, H.M.Christen, N.D.Browning, and Y.Takamwra, Appl. Phys. Lett. **99**, 201908 (2011).

[121] E.Meltchakov, H.-C.Mertins, M.Scher, S.D.Fonzo, W.Jark, and F.Schäfers, “Soft X-ray resonant reflectivity of Gd/Fe multilayers,” J. Magn. Mater. **240**, 550(2002).

[122] K.S.Lee, S.K.Kim, and J.B.Kortright, “Atomic-scale depth selectivity of soft x-ray resonant Kerr effect,” Appl. Phys. Lett. **83**, 3764 (2003).

[123] H. Ade, and A. P.Hitchcock, “NEXAFS microscopy and resonant scattering:Composition and orientation probed in real and reciprocal space,” Polymer **49**, 643 (2008).

[124] M. Mezger, B.M.Ocko, H. Reichert, and M.Deutsch, “High-resolution *in situ* x-ray study of the hydrophobic gap at the water–octadecyl-trichlorosilane interface,” Proc. Natl. Acad.Sci. USA **110**, 3733(2013).

[125] M. Nayak, G. S. Lodha, A.K.Sinha, and R.V.Nandedkar, “Determination of interlayer composition at buried interfaces using soft x-ray resonant reflectivity,” Appl. Phys. Lett. **89**, 181920 (2006).

[126] See http://henke.lbl.gov/optical_constants/

[127] R. Soufli, A.L.Aquila, F.Salmassi, M.Fernández-Perea, and E. Gullikson, “Optical constants of magnetron-sputtered boron carbide thin films from photoabsorption data in the range 30 to 770 eV,” Appl. Opt. **47**, 4633 (2008).

[128] T. Hu, L. Steihl, W. Rafaniello, T. Fawceh, D. D. Hawn, J. G. Marshall, S. J. Rozeveld, C. L. Putzig, J. H. Blackson, W. Cermignani, and M. G. Robinson, “Structures and properties of disordered boron carbide coatings generated by magnetron sputtering,” Thin Solid Films **332**, 80 (1998).

[129] N. Wada, P. J. Gaczi, and S. A. Solin, “Diamond-like 3-fold coordinated amorphous carbon,” J. Non-Cryst. Solids **35-36**, 543 (1980).

[130] R. O. Dillon, J. A. Woollam, and V. Katkanant, “Use of Raman scattering to investigate disorder and crystallite formation in as-deposited and annealed carbon films,” Phys. Rev. B **29,** 3482 (1984).

[131] A. C. Ferrari, J. Robertson, “Interpretation of Raman spectra of disordered and amorphous carbon,”Phys. Rev. B **61**, 14095 (2000).

[132] P.N.Rao, S. K.Rai, A.K.Sinha, M.N.Singh, G.S.Lodha, Thermally induced interface changes in W/B_4C multilayers, Thin Solid Films **589**, 268 (2015).

[133] R. Supruangnet, Ch. Morawe, J-Ch. Peffen, H.Nakajima, S.Rattanasuporn, P. Photongkam, N. Jearanaikoon, W. Busayaporn, Chemical modification of B_4C cap layers on Pd/ B_4C multilayers, Appl. Surf. Sci. **367**, 347 (2016).

[134] P.N.Rao, S.K.Rai, A.K.Srivastava, T.Ganguli, R.Dhawan, P.A.Naik, Microstructure and composition analysis of low-Z/low-Z multilayers by combining hard and resonant soft X-ray reflectivity, J.Appl.Phys. **119**, 245301 (2016).

[135] S. Lee, P.A.Dowben, The properties of boron carbide/silicon hetrojunction diodes fabricated by Plasma-Enhanced Chemical Vapor Deposition, Appl. Phys. A **58**, 223 (1994).

[136] S.Lee, J.MAzurowski, W.L.O'Brien, Q.Y.Dong, J.J.Jia, T.A.Callcott, Y.Tan, K.E.Miyano, D.L.Ederer, D.R.Muller, P.A.Dowben, The structural homogeneity of boron carbide thin films fabricated using plasma enhanced chemical vapor deposition from B_5H_9+$CH_{4,}$ J. Appl. Phys. **74**, 6919 (1993).

[137] A.A.Ahmad, N.J.Ianno, S.D.Hwang, P.A.Dowben, Sputter deposition of high resistivity boron carbide, Thin Solid Films **335**, 174 (1998).

[138] S.P.Singh, M.H.Modi, P.Srivastava, Growth kinetics and compositional analysis of silicon rich a-SiN_x: H film: A soft x-ray reflectivity study, Appl. Phys. Lett. **97**, 151906 (2010).

[139] M. Mayer, SIMNRA User's Guide, Report IPP 9/113, Max-Planck-Institut für Plasmaphysik, Garching, Germany, 1997.

[140] E.O.Filatova, I.V.Kozhevnikov,A.A.Sokolov, E.V.Ubyivovk,S.Yulin,M.Gorgoi, F. Schäfers, Soft x-ray reflectometry and hard x-ray photoelectron spectroscopy and transmission electron microscopy investigations of internal structure of TiO_2(Ti)/SiO_2/Si stacks, Sci.Technol.Adv.Mat. **13**, 015001 (2012) .

[141] E.O.Filatova, A.A.Sokolov, I.V.Kozhevnikov, High-K Gate Dielectrics for SMOS Technology, edited by H. Gang, Wiley-VCH ,Verlag, 2012, pp.225.

[142] E.O.Filatova, A.A.Sokolov, I.V.Kozhevnikov, E.Yu. Taracheva, O.S. Grunsky, F.Schaefers, W Braunn, Investigation of structure of thin HfO2 films by soft x-ray reflectometry techniques, J.Phys.Condens. Mattter, **21**, 185012 (2009).

[143] Ch. Hollenstein, B.P.Deval. T.Dudok de Wit, B.Joye, H.J.Künzli, P.Oelhafen, R.Zehringer, R.Hauert, E.M.Moser, Cold boronisation in TCA, J.Nucl. Mater. **176**, 343 (1990).

[144] C. Ronning, D.Schwen, S.Eyhusen,U.Veter, H.Hofsass, Ion beam synthesis of boron carbide thin films, Surf. Coat. Technol. **158**, 382 (2002).

[145] L.G.Jacobsohn, R.K.Schulze, M.E.H.Maia da Costa, M. Nastasi, X-ray photoelectron spectroscopy investigation of boron carbide films deposited by sputtering, Surf. Sci. **572**, 418 (2004).

[146] K. L. Chopra, Thin film phenomena, McGraw-Hill, Inc, New York, 1969.